CR 151748

THE UNIVERSITY OF TEXAS AT AUSTIN

THE EFFECT OF THE TRANSPORT PROPERTY MODELS ON THE SHUTTLE BOUNDARY LAYER

John J. Bertin, Daniel R. Neal, and
Dennis D. Stalmach

(NASA-CR-151748) THE EFFECT OF THE TRANSPORT PROPERTY MODELS ON THE SHUTTLE BOUNDARY LAYER (Texas Univ. at Austin.) 111 p HC A06/MF A01 CSCL 22B
N78-27165
Unclas
G3/16 25174

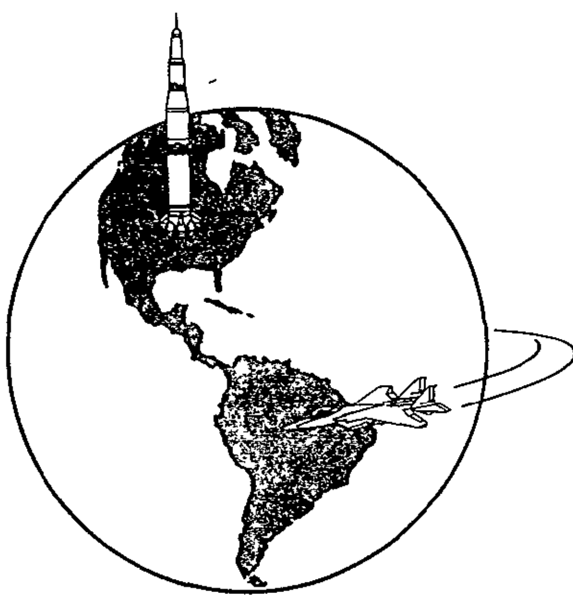

Aerospace Engineering Report 78002

This work was supported by the
Johnson Space Center
through NASA Contract NAS 9–13680

June 1978

Department of Aerospace Engineering and Engineering Mechanics

THE EFFECT OF TRANSPORT PROPERTY MODELS ON THE SHUTTLE BOUNDARY LAYER*

by

John J. Bertin, Daniel R. Neal
and
Dennis D. Stalmach

AEROSPACE ENGINEERING REPORT 78002

*This work was supported by the
Johnson Space Flight Center
through Contract NAS 9-13680

Department of Aerospace Engineering
and Engineering Mechanics

The University of Texas at Austin

June 1978

TABLE OF CONTENTS

ACKNOWLEDGEMENTS

This work was supported by the Johnson Space Center (NASA) through contract NAS9-13680. The authors acknowledge the considerable efforts of Dr. W.D. Goodrich in providing both contractual direction and direct technical contributions. The authors would also like to thank Mrs. Bettye Lofton for skillfully typing the manuscript and Mr. Pradipta Shome for preparing the technical illustrations.

INTRODUCTION

In order to predict the convective heating environment for the windward surface of the Space Shuttle entry configuration, one must develop engineering correlations which define the three-dimensional flow-field. Since the boundary layer is thin, the flow field may be divided into two regions: (1) the viscous boundary layer adjacent to the surface of the vehicle and (2) the essentially inviscid flow outside the boundary layer. The first step is to calculate the inviscid flow between the shock wave and the boundary layer. The second step is to calculate the resultant boundary layer, subject to the boundary conditions provided by the inviscid flow solution and the assumed temperature distribution of the surface. If the displacement thickness of the boundary layer is relatively large, the inviscid flow field could be recalculated using the effective surface as the boundary condition. An iterative procedure could be used to determine the intersection of the solutions provided by the inviscid-flow equations with those for the boundary-layer equations.

The solutions discussed in the present report assume that the inviscid flow field is known and is not affected by the presence of the boundary layer. Specifically, it is assumed that the distributions of the static pressure, the entropy at the edge of the boundary layer and the radius of the "equivalent" body of revolution are known. These parameters define the inviscid flow field. The values of any other properties at the edge of boundary layer which are required to obtain numerical solutions of the boundary layer are calculated using the "real-gas" thermodynamic properties of Ref. 1 and the transport-property models discussed herein.

Theoretical solutions of the nonsimilar, laminar boundary-layer were computed for four points along the shuttle entry trajectory using the code described in Ref. 2. Since the boundary layer is that region of the flow field where the effects of viscosity and of thermal conductivity are most important, numerical solutions for the boundary layer were generated using different models for the transport properties. These solutions, which are the subject of the present report, indicate that the displacement thickness and the heat-transfer rates are very sensitive to changes in the models for thermal conductivity and for specific heat. Thus, the solutions are sensitive to the assumed transport-property model.

The significance of the fact that the theoretical heat-transfer rates vary significantly is of obvious importance to the shuttle design. However, the sensitivity of the calculated displacement thickness to the assumed transport-property model is also of importance. As noted in Ref. 3, "The experimentally-determined transition locations indicate that the tile-induced flow perturbations become strongest when the height of the misaligned tiles is of the order of the displacement thickness". Although the misaligned tiles were distributed over much of the windward surface, the relative transition locations were correlated in terms of the ratio of δ^*/k evaluated at $x \approx 0.1L$.

Van Driest and Boison (Ref. 4) correlated the effects of triptype roughness elements on the relative transition Reynolds number using the ratio of the roughness height to the boundary-layer displacement thickness (k/δ^*) evaluated at the trips. Other investigators have used parameters which depend on the solution of the undisturbed boundary layer to correlate the effects of roughness on transition. For example, van Driest and Blumer (Ref. 5) have used Re_{δ^*}, where:

$$Re_{\delta^*} = \frac{\rho_e U_e \delta^*}{\mu_e} , \tag{1}$$

to correlate data showing the effect of a band of spherical roughness elements on conical models as well as on flat plates. Holloway and Morrisette (Ref. 6) have used Re_k, where:

$$Re_k = \frac{\rho_k U_k k}{\mu_k} \tag{2}$$

(the subscript k denotes that the property is evaluated at the top of the roughness element), to correlate the effect of controlled roughness on boundary-layer transition for unswept, blunted flat plates.

It should be noted that a parameter which correlates the roughness effects for one configuration may not provide an adequate correlation of the roughness effects for a different configuration (see Ref. 7). Note also that the objective of this brief literature review is not to recommend a specific transition correlation but to demonstrate that such correlations employ parameters which depend on the theoretical solution of the undisturbed, laminar boundary-layer solutions. The solutions presented in this report illustrate the effect of the assumed transport property models on the theoretical solutions for the undisturbed, laminar boundary-layer.

NOMENCLATURE

C	Chapman-Rubesin factor $\frac{\rho\mu}{\rho_e\mu_e}$
C_f	local skin friction coefficient
$\bar{C}_p$	specific heat, $\sum_i C_i C_{pi}$
F	dimensionless streamwise component of the local velocity $\frac{u}{u_e}$
h	enthalpy
k	thermal conductivity
L	length of the Space Shuttle Orbiter
M	Mach number
p	pressure
Pr	Prandtl number, $\frac{\mu\bar{C}_p}{k}$
$\dot{q}$	local convective heat-transfer rate
r	distance from surface of body to axis of symmetry, measured normal to the axis of symmetry
S	entropy
T	temperature
u	velocity in streamwise direction
v	velocity normal to the wall
x	physical streamwise wetted distance from the stagnation point
y	physical distance normal to the wall
δ	boundary-layer thickness

δ^*	displacement thickness, equation (17)
θ	non-dimensional temperature $\frac{T}{T_{te}}$
θ	momentum thickness, equation (19)
μ	viscosity
ρ	density

Subscripts

a	measured along the axis of the Shuttle Orbiter
e	edge value
te	local stagnation value at the edge of the bounary layer
t2	stagnation value downstream of the normal shock wave
w	wall value

Superscripts

k	body geometry factor, k = 0, for two-dimensional flow; and k = 1 for axisymmetric flow

THEORETICAL ANALYSIS

Theoretical solutions of the nonsimilar, laminar boundary layer were obtained using the finite difference code described in Ref. 2. The code provides solutions for the laminar boundary layer for an axisymmetric or a two-dimensional configuration with possible ablation or transpiration cooling. The body may be either axisymmetric or two-dimensional providing the radius of curvature is large in comparison to the boundary layer thickness, i.e., centrifugal forces are neglected. Approximate solutions for a three-dimensional boundary layer with small cross flow can be obtained using the axisymmetric analog (Ref. 8) in which an effective radius of curvature is used to describe the streamline divergence. For flow with no mass injection at the wall, the thermodynamic properties of the free-stream gas may be modeled with the ideal gas relations (Ref. 9) or with real gas properties using the thermodynamic subroutine, "MOLIER", which correspond to those presented in Ref. 1. For flows with mass injection, the thermodynamic properties of the mixture of injectant and stream gases are approximated with the ideal gas relations. Chemical reactions between the species are not considered. The governing equations applicable to the flow model are as follows:

continuity: $$\frac{\partial(\rho u r^k)}{\partial x} + \frac{\partial(\rho v r^k)}{\partial y} = 0 \qquad (3)$$

where $k = 1$ for axisymmetric flows and $k = 0$ for two-dimensional flow.

species: $$\rho u \frac{\partial C_i}{\partial x} + \rho v \frac{\partial C_i}{\partial y} = \frac{\partial}{\partial y}\left(\rho D_i \frac{\partial C_i}{\partial y}\right) \qquad (4)$$

x-component of momentum:

$$\rho u \frac{\partial u}{\partial x} + \rho v \frac{\partial u}{\partial y} = - \frac{\partial p_e}{\partial x} + \frac{\partial}{\partial y}\left(\mu \frac{\partial u}{\partial y}\right) \qquad (5)$$

y-component of momentum:

$$\frac{\partial p}{\partial y} \simeq 0 \qquad (6)$$

which represents the standard boundary-layer assumption regarding the pressure gradients normal to the wall.

energy:

$$\rho u \frac{\partial h}{\partial x} + \rho v \frac{\partial h}{\partial y} = u \frac{dp_e}{dx} + \frac{\partial}{\partial y}\left(k \frac{\partial T}{\partial y} + \rho D_i \sum_i h_i \frac{\partial C_i}{\partial y}\right) + \mu \left(\frac{\partial u}{\partial y}\right)^2 \qquad (7)$$

The governing equations which describe the nonsimilar, possibly compressible, flow in physical coordinates are nonlinear, partial differential equations. Therefore, a transformation is sought to simplify the solution procedures. Using the standard Lee-Dorodnitsyn coordinate transformation (Ref. 10):

$$s = \int_0^x \rho_e \mu_e u_e r^{2k} dx \tag{8}$$

$$\eta = \frac{\rho_e u_e r^k}{\sqrt{2s}} \int_0^y \frac{\rho}{\rho_e}\, dy \tag{9}$$

An additional coordinate transformation is made, as suggested in Ref. 11:

$$n = 1 - e^{-\alpha\eta} \tag{10}$$

This transformation is for numerical purposes. Numerical integrations can now be carried out over a fixed interval (zero to one) rather than the usual interval in the η-coordinate system (zero to infinity). This coordinate system eliminates the need for an iteration to define the boundary layer edge. Note that in the present approach it is assumed that the edge of the viscous boundary layer, the edge of the thermal boundary layer, and the edge of the species concentration layer, all occur at the same η.

Also, the transformation affects nodal point spacing in the physical-coordinate plane. Points which are evenly spaced with respect to the n-coordinate are not evenly spaced in physical space. Spacing of the y-coordinates of the nodal locations varies with position, such that Δy increases with distance from the wall.

This results in more nodal points in the region near the wall, where gradients are large, and fewer points in the region away from the wall, where gradients are smaller. The scale factor α is treated as a constant for any two adjacent streamwise stations. If the value of the edge shear, which is defined as:

$$\frac{F_N - F_{N-1}}{\Delta n} ,$$

is not within the range 0.0 to 0.2, α is changed by 5%. The boundary layer is recalculated until the edge shear criteria is met. Thus, the scale factor may change, e.g., for an accelerating flow past a cooled wall. The resultant governing equations in the transformed coordinate system, with $F = \frac{u}{u_e}$ and with $\theta = \frac{T}{T_{te}}$, are as follows.

Species:

$$\alpha^2(1-n)^2\left(\frac{C}{Sc}\right)_n C_{1n} + \alpha^2(1-n)\left((1-n)\,C_{1nn} - C_{1n}\right)\frac{C}{Sc} + \alpha(1-n)\,f\,C_{1n}$$

$$= 2s\left(C_{1s}F - \alpha(1-n)\,F_s\,C_{1n}\right) \qquad (11)$$

momentum:

$$fF_n\,\alpha(1-n) + \alpha^2(1-n)^2\,C_nF_n + C\alpha^2(1-n)\left((1-n)\,F_{nn} - F_n\right)$$

$$+ \beta\left(\frac{\rho_e}{\rho} - F^2\right) = 2s\left(FF_s - f_sF_n\,\alpha(1-n)\right) \qquad (12)$$

energy:

$$\frac{1}{\bar{C}_p}\alpha^2(1-n)^2\left(\frac{C\bar{C}_p}{Pr}\right)_n\theta_n + \left(\frac{C}{Pr}\right)\alpha^2(1-n)\left((1-n)\theta_{nn} - \theta_n\right) + \alpha(1-n)\,f\,\theta_n$$

$$+\frac{C_{1e}}{\bar{C}_p}\frac{C}{Sc}\left(C_{p_1} - C_{p_2}\right)\alpha^2(1-n)^2\,\theta_n C_{1n} + \frac{Cu_e^2}{\bar{C}_p T_{te}}F_n^2\,\alpha^2(1-n)^2$$

$$-\frac{u_e^2}{\bar{C}_p T_{te}}\beta\frac{\rho_e}{\rho}F = 2s\left(F\theta_s - \alpha(1-n)\,\theta_n f_s\right) \tag{13}$$

where the subscripts n and s denote differentiation with respect to n and s, respectively.

Boundary Conditions

In the previous section, the governing equations were written in terms of three dimensionless, dependent variables, F, C_1, and θ. Since the surface temperature and the inviscid flow field are known a priori, values for F and θ are immediately determined at both boundaries.

At the wall, $n = 0$:

$$F = 0$$

$$\theta = \frac{T_w}{T_{te}}$$

$$C_{1n} = \frac{(\rho v)_w\, C_{1w}\, Sc_w\sqrt{2s}}{\alpha\;\rho_w\;\mu_w\;u_e\;r^k}$$

$$f(0) = -\frac{1}{\sqrt{2s}}\int_0^x (\rho v)_w\, r^k\, dx$$

At the boundary layer edge, $\eta = 1$:

$$F = 1$$

$$\theta = \frac{T_e}{T_{te}}$$

$$C_1 = 1$$

$$C_2 = 0$$

DISCUSSION OF RESULTS

As noted in the Introduction, theoretical solutions of the non-similar, laminar boundary layer were computed for four points, i.e., times, along the Shuttle entry trajectory. The times were selected to represent a wide range of flow conditions and, therefore, varying degrees of validity of the assumed transport property models. The free-stream conditions, the angle-of-attack, and the properties which define the local, inviscid flow-field, are presented in Table 1. Specifically, the static pressure (p_e), the entropy at the edge of the boundary layer (S_e/R), and the radius of the "equivalent" body of revolution (RDS) are given as function of the wetted distance from the stagnation point in the plane of symmetry (x) for the 49 (M) streamwise stations. The surface temperature (T_w) is also assumed to be known. Except for the viscosity, any other properties of the inviscid flow at the edge of the boundary layer, which are required to obtain numerical solutions, are evaluated using the "real-gas" thermodynamic properties of Ref. 1. The viscosity is calculated using one of the transport-property models described herein.

Since there is no mass injection at the surface, all of the gas is the stream gas, i.e., air, and $C_1 = 1.0$ at all points in the boundary layer. Thus, each of the terms in equation (11) is zero.

For incompressible flows, the momentum and the energy equations must be solved simultaneously for the unknowns, F and θ. Simultaneous treatment of the equations must be done, since the cofactors of the velocity function (F) in the momentum equation include temperature-dependent parameters, i.e., the Chapman-Rubesin factor ($C = \rho\mu/\rho_e\mu_e$) and the density ratio (ρ/ρ_e). In addition to F and θ, both of which appear explicitly in the energy equation, numerous temperature-dependent parameters appear in the cofactors of the energy equation. These parameters include the Chapman-Rubesin factor, the density ratio, the specific heat ($\bar{C}_p$), and the Prandtl number (Pr). Since the Prandtl number is:

$$Pr = \frac{\mu \bar{C}_p}{k} \tag{14}$$

the thermal conductivity (k) also appears in the cofactors of the energy equation.

The MOLIER subroutine was used to calculate the densities in the boundary layer for all cases. Note that the pressure was constant across the boundary layer and the inviscid pressure distribution for a given flight condition was independent of the assumed transport-property model. Thus, at a given x-location, the density would be a function of the temperature only. However, the temperature profiles differed for the different transport-property models. As a result, the density profiles depended on the transport-property model.

Boundary-layer solutions were obtained using six "different" models to represent the pressure/temperature-correlation of the transport properties. For the purposes of this report, they are designated:

(1) perfect-gas model

(2) linear interpolation of values of Ref. 12

(3) Real-gas model, p = 1.0 atm

(4) Real-gas model, p = 0.1 atm

(5) Real-gas model, p = 0.01 atm, and

(6) Real-gas model, averaged properties

The perfect-gas model. - It was assumed that the specific heat and the Prandtl number are constant for perfect air. Specifically (see Table 2a),

$$C_p = 0.2404 \frac{\text{Btu}}{\text{lbm}°\text{R}} = 7.7346 \frac{\text{Btu ft}}{\text{lbf sec}^2 °\text{R}}$$

$$Pr = 0.70$$

Furthermore, it was assumed that the viscosity of perfect air is given by Sutherland's formula (Ref. 13):

$$\mu = 2.27 \frac{T^{1.5}}{T \times 198.6} \times 10^{-8} \frac{\text{lbf sec}}{\text{ft}^2} \tag{15}$$

Since the Prandtl number and the specific heat are constant, the thermal conductivity can be calculated directly using equations (14) and (15).

Thus, the viscosity and the thermal conductivity are a function of temperature only, i.e., are independent of pressure, for perfect air. When using the code, the value of a transport property at some temperature is calculated using a cubic-polynomial fit of the tabulated values.

The linear interpolation model. - The transport-property values calculated using this model were obtained using a double linear-interpolation of tabulated real-gas values. In this technique, a given transport property is specified as a function of $\log_{10}p$ and T. The tabulated values, which are presented in Tables 2b, 2c, 2d, and 2f, are "essentially" those of Hansen (Ref. 12). The following comments are made to explain the use of the word "essentially",

(1) In order to improve the accuracy of the interpolated values, additional values at temperatures below 800°R were added to those presented in Ref. 12. The additional values were calculated using the perfect-gas relations.

(2) The viscosity (μ), the thermal conductivity (k), and the Prandtl number (Pr) were taken directly from the tables of Ref. 12. Then, in order to have consistent interrelations between the values for the different properties, the specific heat ($\bar{C}_p$) was calculated using equation (14).

<u>The real-gas models at a specified pressure, i.e., 1.0 atm, 0.1 atm, or 0.01 atm.</u> - For these three "models", the transport properties were assumed to be a function of temperature only. The temperature-dependence of the transport-property values for a specific pressure is assumed to be defined by the values of Hansen (Ref. 12). See Tables 2b, 2c, and 2d. Thus, when using the code, the value of a transport property at some temperature is calculated using a cubic-polynomial fit of the tabulated values.

Even though the properties are assumed to be a function of temperature only, these models are termed real-gas models, since the values for the transport properties, i.e., the thermal conductivity, the viscosity, etc., reflect the real-gas effects at the specified pressure. However, because the values of the transport properties for a real-gas are a function of temperature and of pressure, these models are only approximate. These models were included in the present study, since correlations of the transport properties in terms of a single variable (temperature) are relatively easy to code and, therefore, represent an attractively simple model for the transport properties. The degree to which the failure to include the pressure-dependence affects the validity of the approximation depends not only on the static pressure and the changes in the static pressure over the body but also on the temperature. The static pressures and the amount the stagnation pressure varies is shown in the tabulated values of Table 1.

The real-gas model using the averaged properties. - Since the stagnation pressure for the four flight conditions varied from 0.02 atm to 0.10 atm, a sixth model for the transport properties was assumed. For this model, the values were the arithmetic average of the values from Ref. 12 for p = 0.1 atm and for p = 0.01 atm. The resultant values are presented in Table 2e. This too is only an approximate real-gas model, since the property values change rapidly with temperature at the higher temperatures.

Transport Properties

For the flight conditions of the present study, the temperature in the shock layer varies from approximately 1400°R (which corresponds to the temperature of the air adjacent to the surface for the coldest wall condition) to 11,000°R (which corresponds to the highest stagnation temperature over the range of flight conditions). Over this temperature range, the molecules of air not only vibrate but dissociate into atoms. As a result, the thermodynamic and the transport properties of real air are significantly different than those of perfect air. Furthermore, they are functions both of temperature and of pressure. The viscosity, the Prandtl number, the thermal conductivity, and the specific heat are presented in Figs. 1-3.

Viscosity. - The viscosity is presented in Fig. 1. For temperatures of less than 8000°R, the viscosity is independent of pressure and the perfect-gas correlation provides accurate values for the actual viscosity. Thus, the viscosity coefficient is not significantly influenced by the oxygen dissociation. At temperatures in excess of 8000°R, the actual values of the viscosity are greater than those given by the perfect-gas correlation, being greatest for the lowest pressure (over this range of temperature). Thus, the dissociation of nitrogen affects the value of the viscosity.

Thermal conductivity and specific heat. - Energy is transferred either (1) by molecular collisions or (2) by diffusion of molecular species and the reactions which occur as the gas tends to maintain itself in chemical equilibrium at each point. The first mechanism is the one responsible for the thermal conductivity of nonreacting gases. The second mode of energy transfer, which takes place whenever the gas undergoes a chemical reaction, is due to the diffusion of the chemical species. These particles then react with one another, giving off or absorbing the heat of reaction and causing the heat transfer which may be considerably larger than the ordinary heat transfer due to molecular collisions.

Note that the specific heat and the thermal conductivity go through distinct maxima where the chemical components change most rapidly with temperature (see Fig. 3). The first maximum is due to the oxygen dissociation reaction; the second is due to the nitrogen dissociation reaction. When the pressure decreases, these maxima increase in sharpness and in magnitude, as they shift to lower temperatures.

Prandtl number. - At relatively low temperatures, the air is like a pure diatomic gas with a constant specific heat, equal to approximately 7R/2. As the temperature increases, vibrational energy is excited. At these temperatures, the specific heat ($\bar{C}_p$) increases more than the thermal conductivity (k) and the Prandtl number increases (see Fig. 2). At still higher temperatures, the oxygen dissociates and both $\bar{C}_p$ and k go through pronounced maxima (as shown in Fig. 3), while the viscosity coefficient is essentially unaffected. Since the maximum for k occurs at slightly lower temperatures than the maximum for $\bar{C}_p$, the Prandtl number decreases. As a result, the Prandtl number is an "s-shaped" function of temperature. As the nitrogen dissociation proceeds, the Prandtl number exhibits a second "s-shaped" correlation with temperature for the same reasons discussed for the oxygen dissociation. Fully dissociated air is like a pure monatomic gas so that the Prandtl number approaches 2/3. Thus, as long as the temperature is below the level at which ionization begins, the Prandtl number is in the range from 0.6 to 1.0.

A Detailed Discussion of the Results for One Flight Condition

The theoretical boundary-layer solutions for one flight condition will now be discussed in detail. The flight condition chosen is that for a free-stream Mach number of 22.04, an altitude of 226,000 ft., and an angle of attack of 40.2°. This flight condition was chosen as representative of the results obtained in the present study. The temperature of the air is sufficiently high that the effects of dissociation are appreciable. This will be evident in the results presented herein.

In this section, various parameters are presented as a function of y at two streamwise stations in the windward plane of symmetry. The locations of the two stations are illustrated in Fig. 4. It should be noted that the photograph is from a wind tunnel test of a scale model and is presented only to provide the reader with (approximate) relative locations. The first station is 2.596 ft from the stagnation point. The inviscid-flow Mach number at this location for this flight condition is 1.498. At the second station, which is 56.375 ft from the stagnation point, the inviscid-flow Mach number is 3.238.

<u>Profiles of the basic unknowns, F and θ</u>. - Distributions of the streamwise velocity component and of the static temperature across the boundary layer are presented in Figs. 5 and 6, respectively.

The velocity, which is presented as the dimensionless ratio u/u_e, is only a weak function of the assumed transport model. Even at x = 56.375 ft, where the boundary-layer thickness (δ) calculated using the perfect-gas transport properties is 3.5 times that calculated using the more appropriate linear interpolation model, the velocities at a given y-coordinate are within 4% of each other. Because the velocity profiles are relatively insensitive to the transport-property models and because the viscosity at the wall is equal to the perfect gas value for the entire range of pressure considered at these surface temperatures, the shear at the wall is virtually independent of the transport-property model.

The corresponding temperature distributions are presented in Fig. 6. Because it is important that the magnitude of the temperature is known, so that the chemistry of the situation can be identified, the temperatures have not been nondimensionalized. Further, the corresponding distributions of the thermal conductivity, which affects the temperature distributions, are presented in Fig. 7.

Consider just the temperature distributions calculated using the linear-interpolation model, which represents both the temperature- and the pressure-dependence of the transport properties. Since the static pressure is 0.035 atm at the first station and 0.019 atm at the second station, a "local" peak in the thermal conductivity occurs at about 5400°R due to the dissociation of oxygen and a second, stronger, "local" peak occurs at about 9900°R due to the dissociation of nitrogen (see Fig. 2). Thus, very near the wall, the temperature increases rapidly with y. The thermal conductivity is relatively high in this region due to the dissociation of oxygen allowing the energy associated with the high temperatures in the outer portion of the boundary layer to be transmitted toward the wall. There is a slight inflection point in the T(y) distribution when the temperature is near 6000°R. The inflection point corresponds to the relatively low values for the thermal conductivity of air in this temperature range. There is a rapid increase in the value of the thermal conductivity as the temperature increases above 7000°R due to the dissociation of nitrogen. These locally high values of the thermal conductivity result in a rapid increase in temperature to the values at the outer edge of the boundary layer. Because the dissociated nitrogen accommodates the transmission of energy inward, only ten per cent of the temperature change from the wall value to the edge value occurs in the outer two-thirds of the boundary layer.

Now consider the temperature distributions calculated using the transport properties of Ref. 12 for $p = 1.0$ atm (see Table 2b). Recall that the thermal conductivity and the specific heat go through three distinct maxima where the chemical components change most rapidly with temperature. When the pressure increases, these maxima decrease in sharpness and in magnitude as they shift to higher temperatures. Note that in the solutions obtained using the 1.0 atm values of the transport properties, the temperature changes much more slowly with y when the temperature is above 6000°R. This occurs because the thermal conductivity in this temperature range (i.e., 6000°R to 10,000°R) is much less when $p = 1.0$ atm than when $p \sim 0.03$ atm. As a result, the temperature is essentially a linear function of y over a significant fraction of the outer boundary layer.

Finally, consider the temperature distributions calculated using the perfect-gas transport properties. The perfect-gas thermal conductivity, which is given by:

$$k = 2.50 \times 10^{-7}\, T \left(1 + \frac{198.6}{T}\right)^{-1} \left[\frac{\text{Btu}}{\text{ft sec}^\circ\text{R}}\right] \tag{16}$$

does not exhibit any of the chemistry-related peaks of the real-gas models and is more than 20 times less than the real-gas values at certain (p,T). Because of the relatively low thermal conductivity, the calculated temperature at a given y is lowest when the perfect-gas transport properties are used. Note that, at the downstream station, i.e., x = 56.375 ft, the temperature reaches a local maximum near the wall. These locally high temperatures are often seen in the perfect-gas solutions of a supersonic, laminar boundary-layer and are attributed to the effects of viscous dissipation. The thickness of the boundary-layer calculated using the perfect-gas transport properties is much greater than that for either of the two real-gas solutions. A possible explanation is that this occurs, because the lower thermal conductivities require that the change in temperature from the wall value to the edge value be spread over a greater distance.

The reader is cautioned against over simplifying the mechanisms of energy conversion and transport in the boundary layer. Note that the changes in the chemical composition of the air cause the specific heat to vary in a manner similar to that of the thermal conductivity. However, these calculations show that realistic modeling of the transport properties is required if valid design predictions are to be expected.

<u>The density ratio, the viscosity ratio, and the Chapman-Rubesin factor</u>. - The distributions of density, of viscosity, and of the Chapman-Rubesin factor across the boundary layer are presented in Figs. 8-10, respectively. Furthermore, regardless of what transport properties were used, the density was calculated using the MOLIER subroutine, which uses the real-gas thermodynamic relations. The static pressure in the boundary layer at a particular station is independent of the assumed transport-property models. Thus, at a particular x-location, the dimensionless density (ρ/ρ_e) is a function of the temperature only. The y-gradient of the temperature was greatest when the linear interpolation model was used. Therefore, the temperature rapidly approaches the edge value. Only very near the wall is the density ratio significantly greater than unity for this transport-property model. However, the temperatures changed relatively slowly with y for the solutions obtained using the perfect-gas transport properties. Since the surface temperature is significantly less than the edge temperature, the local density is 1.25 times the edge value over much of the boundary layer. These relatively high densities in the boundary layer apparently do not significantly affect the velocity profile. In fact, the boundary layer thickness (δ) was greatest for the solution where the density is largest, i.e., that for the perfect-gas transport properties at x = 56.375 ft. As discussed previously, the large δ for this solution is attributed to the fact that, since the temperature gradient is relatively small, a larger distance is required to achieve the edge conditions.

As evident in Fig. 1, the viscosity is not significantly affected by the dissociation of oxygen. The perfect-gas model accurately describes the coefficient of viscosity until the temperature reaches 6300°R. Pressure-dependent changes are of the order of a few percent over the entire temperature range for the boundary layer solutions for the $M_\infty = 22.04$ flow. The viscosity profiles are presented in Fig. 9.

The Chapman-Rubesin factor is presented in Fig. 10 as a function of y at the two streamwise stations for the $M_\infty = 22.04$ flow field. With the exception of the solution at the downstream station which was obtained using the perfect-gas transport properties, the Chapman-Rubesin factor decreases rapidly from the wall value. For the solution using the linear interpolation model, the value is between 1.0 and 1.2 except for $y < 0.2\delta$. The local maximum which occurs in the theoretical temperature distribution calculated using the perfect-gas transport properties causes the Chapman-Rubesin factor for that solution to be markedly different in character than the other profiles.

<u>The displacement thickness</u>. - As noted in the Introduction, the displacement thickness is often used as a parameter in correlations of the effect of surface roughness on the transition location. The displacement thickness for a compressible boundary layer is given by (Ref. 14):

$$\delta^* = \int_0^\delta \left(1 - \frac{\rho u}{\rho_e u_e}\right) dy = \frac{\sqrt{2s}}{\rho_e u_e r^k} \int_0^{1.0} \left(\frac{\rho_e}{\rho} - \frac{u}{u_e}\right) \frac{d\eta}{\alpha(1-\eta)} \qquad (17)$$

Because the wall is relatively cool, the density of the air next to the surface is 5.0 ρ_e. In many instances, the velocity parameter

(u/u_e) increases faster than the density parameter (ρ/ρ_e) decreases. Thus, as illustrated by the calculations presented in Fig. 11, the integrand $(1 - \rho u/\rho_e u_e)$ is negative at many points in the boundary layer. At the upstream station (x = 2.596 ft), the integrand is negative for a considerable fraction of the boundary layer for two of the solutions. As a result, the theoretical value of the displacement thickness at x = 2.596 ft is negative when the transport properties are calculated using either the perfect-gas model or the real-gas model with p = 1.0 atm. The theoretical value of the displacement thickness is positive, when the linear interpolation model is used. The streamwise distributions for the displacement thickness are presented in Fig. 12. At the downstream station (x = 53.375 ft), the integrand exceeds - 1.0 at one point in the boundary-layer which was calculated using perfect-gas transport properties. Because the integrand assumes large negative values over most of the boundary layer, the displacement thickness is negative and very large (- 0.19475 ft). In the solution generated using the real-gas model, p = 1.0 atm, the integrand assumes both negative and positive values. As a result, δ^* is positive but is relatively small (+0.01031 ft.) The linear interpolation model yields a solution for which $\delta^* = + 0.023803$ ft.

The large negative values of δ^* result because the density in the boundary layer is so large. Furthermore, because the assumed transport-property model affects the temperature distribution, it also affects the local values of the density. As will be shown in the subsequent figures, the magnitude of the displacement thickness at a station for a given flow field is very sensitive to the assumed transport-property model.

Therefore, calculations were made using the definition of the displacement thickness for an incompressible flow. For an incompressible flow,

$$\delta_i = \int_0^\delta \left(1 - \frac{u}{u_e}\right) dy \tag{18}$$

Since the velocity ratio is less than one throughout the boundary layer, δ_i^* will always be positive. Furthermore, because the velocity profile is relatively insensitive to the assumed transport-property model, δ_i^* should be too. Streamwise distributions of δ_i^* are presented in Fig. 12 for the solutions generated using the perfect-gas model and the linear interpolation model. Note that the values of δ_i^* (the incompressible definition) are approximately 1.5 to 2.0 times the values of δ^* (the compressible definition).

Momentum thickness. - The momentum thickness is another parameter which can be used in correlating the effect of a step height on the local flow field. The momentum thickness for a compressible boundary layer is given by (Ref. 14):

$$\theta = \int_0^\delta \frac{\rho u}{\rho_e u_e} \left(1 - \frac{u}{u_e}\right) dy = \frac{\sqrt{2s}}{\rho_e u_e r^k} \int_0^\delta \frac{F(1 - F)d\eta}{\alpha(1 - \eta)} \tag{19}$$

The integrand $\frac{\rho u}{\rho_e u_e}(1 - \frac{u}{u_e})$ is presented as a function of y in Fig. 13. For the downstream station, the value of the integrand for the solution obtained using the perfect-gas model is significantly greater than the corresponding values for the two "real-gas" solutions.

As a result, the momentum thickness calculated using the perfect-gas model is significantly greater than the "real-gas" values. As shown in Fig. 14, the values of the momentum thickness calculated using the real-gas properties at $p = 1.0$ atm and those calculated using the linear interpolation model are in good agreement. As will be evident in the subsequent figures, the magnitude of the momentum thickness at a given station for a given flow field is essentially the same for all of the real-gas models.

Skin-friction coefficient. - The skin-friction coefficient is given by:

$$C_f = \mu_w \left(\frac{\partial u}{\partial y}\right)_w \Big/ 0.5\, \rho_e u_e^2 \tag{20}$$

Recall that the wall temperature is a specified input boundary condition for a given flow condition (see Table 1). For the wall temperature range of the present study, the viscosity coefficient is independent of the transport-property model. Furthermore, as has already been discussed, the transport-property model had only a minor effect on the computed values of the velocity component u near the wall. Thus, the skin-friction coefficient, as calculated using equation (20) is essentially independent of the transport-property model. This conclusion is verified by the theoretical coefficients which are presented in Fig. 15 as a function of x, the streamwise coordinate.

Heat transfer. - The heat transfer from the air in the boundary layer to the surface is given by:

$$\dot{q} = k_w \left(\frac{\partial T}{\partial y}\right)_w \tag{21}$$

The local heating rates were divided by the heat-transfer rate to the stagnation point of a sphere whose radius is 1.0 foot ($\dot{q}_{t,ref}$). The reference heating rate was calculated using the relation of Detra, Kemp, and Riddell (Ref. 15):

$$\dot{q}_{t,ref} = 17{,}600 \left(\frac{U_\infty}{25{,}600}\right)^{3.15} \left(\frac{\rho_\infty}{0.002377}\right)^{0.5} \tag{22}$$

For this equation the units of $\dot{q}_{t,ref}$ are Btu/ft^2 sec; U_∞, ft/sec; and ρ_∞, slugs/ft^3. Equation (22) provides an approximate correlation of a series of calculations based on the relations developed in Ref. 16. Therefore, the reference heating rate incorporates a "real-gas" transport-property model. Note that the reference heating rate is a function of the velocity and of the altitude only. Therefore, there is a specific value of $\dot{q}_{t,ref}$ for each flow condition.

For the surface temperature range of the present study, the thermal conductivity of the air adjacent to the wall is essentially independent of the transport-property model. However, the variation of temperature across the boundary layer is very sensitive to the transport properties. As noted when discussing Fig. 6, the relatively high values of thermal conductivity of the dissociated air allowed the high temperatures at the edge of the boundary layer to be transmitted inward. Thus, the temperature gradient at the wall is greatest for the real-gas, linear interpolation model. As a result, the heat-transfer rates vary significantly, as evident in the theoretical distributions presented in Fig. 16.

A Review of the Results for the Four Flight Conditions

The theoretical, laminar boundary-layer solutions for the four flight conditions will be reviewed now. Distributions of the displacement thickness, the momentum thickness, the skin-friction coefficient, and the heat-transfer rate are presented in this section. The values of the parameters as calculated for the six transport-property models considered in the present study are compared in one set of figures, i.e., Figs. 17, 19, 22, and 24. The values of these parameters as calculated by three different groups for the flight environment are presented in the second set of figures. The three groups are:

(a). The University of Texas at Austin (whose calculations are designated by "values calculated using NSBLLI code"),

(b). The Lockheed Electronics Company/the Johnson Space Center (whose calculations are designated by "values calculated using BLIMP code") and

(c). Rockwell International.

The NSBLLI code used by the University has been described briefly in this report and is described in detail in Ref. 2. The calculations presented in this section use the transport-properties obtained with a double-linear interpolation of tabulated real-gas values. The BLIMP code used by the Lockheed Electronics Company/the Johnson Space Center is described in Ref. 17. A detailed comparison of solutions obtained using these two codes has been reported in Ref. 2. The theoretical solutions for flow condition (a) and for flow condition (d) were compared. Not only was there good agreement for parameters such as δ^*,

θ, C_f, and $\dot{q}/\dot{q}_{t,ref}$, but the velocity profiles and the temperature profiles were in good agreement. The values calculated by Rockwell International were provided by Dr. W.D. Goodrich of the Johnson Space Center. These tabulated values included those required to define the inviscid flow field (which are reproduced in Table 1 and which were used as input for the NSBLLI code and for the BLIMP code) and those values of δ^*, θ, and C_f (which are presented in Figs. 18, 21, 23, and 25). Note that neither detailed boundary-layer profiles nor heat-transfer-rate distributions from Rockwell International were available for comparison.

The effect of the transport-property models on the aerothermodynamic parameters has been discussed in the previous section for flow condition (c). The values of the displacement thickness and of the local heating rate were seen to be sensitive to the transport-property model. These trends are also evident in the solutions for the other flow conditions. This is true even at the lowest free-stream Mach number, i.e., 9.49, or flow condition (a), where the stagnation temperature is 5508°R. Oxygen, but not nitrogen, will dissociate at these temperatures. At the other flight conditions, the nomentum thickness is essentially the same for the various "real-gas" transport-property models but is significantly greater for the perfect-gas model. The skin-friction coefficient is essentially the same for all transport-property models.

The real-gas effects not only affect the local values of the displacement thickness as calculated using the different transport-property models but they also affect its distribution. This is indicated in the theoretical distributions of the displacement thickness for flow condition (b), which is presented in Fig. 19a. There is a sudden, sharp increase in δ^* for $x > 0.13L$. Near the nose, where the displacement thickness is relatively small, the temperature of the inviscid flow at the edge of the boundary layer is sufficiently large that considerable dissociation of nitrogen occurs. The high static temperatures near the nose are evident in the temperature profiles presented in Fig. 20. The temperature at the edge of the boundary layer decreases in the streamwise direction so that, for $x \sim 0.13L$, $T_e \approx 6900°R$. The temperature at points within the boundary layer is less than this. Therefore, there is no appreciable dissociation of nitrogen for stations downstream of $x = 0.13L$. Note that the effect of the local composition of air also influences the thermodynamic properties, such as the density. Thus, the reader is cautioned against oversimplification by attributing these "anomalies" to a single parameter. The δ^* distribution calculated using the BLIMP code (see Fig. 21a) exhibited a similar behavior in this region. Therefore, the result is not dependent on the numerical algorithms used to solve the governing equations. However, based on the previous comments about the correlation between the BLIMP solutions and the NSBLLI solutions, this agreement should not be surprising.

CONCLUDING REMARKS

Theoretical solutions of a nonsimilar, laminar boundary layer have been obtained for four points along the entry trajectory for the Shuttle Orbiter entry configuration. The times were selected to represent a wide range of flow conditions. Boundary-layer solutions were obtained using six "different" models to represent the pressure/temperature-correlation of the transport properties. The following conclusions are made based on these calculations.

(1). The displacement thickness and the heat transfer rates were very sensitive to the assumed transport-property model.

(2). The skin-firction coefficient was independent of the transport-property model.

(3). The momentum thickness was essentially the same for the various "real-gas" transport-property models but is significantly greater for the perfect-gas model.

REFERENCES

1. W.E. Moeckel and K.C. Weston, "Composition and Thermodynamic Properties of Air in Chemical Equilibrium", TN4265, April 1958, NACA.

2. D.D. Stalmach and J.J. Bertin, "The Analysis of a Nonsimilar Laminar Boundary Layer", Aerospace Engineering Report 78001, Feb. 1978, The University of Texas at Austin.

3. J.J. Bertin, E.S. Idar, III, and W.D. Goodrich, "Effect of Surface Cooling and Roughness on Transition for the Shuttle Orbiter", AIAA Paper No. 77-704, AIAA 10th Fluid and Plasma Dynamics Conference, Albuquerque, N.M., June 1977.

4. E.R. van Driest and J.C. Boison, "Experiments on Boundary Layer Transition at Supersonic Speeds," Journal of the Aeronautical Sciences, Dec. 1957, Vol. 24, No. 12, pp. 885-899.

5. E.R. van Driest and C.B. Blumer, "Boundary-Layer Transition at Supersonic Speeds: Roughness Effects with Heat Transfer, AIAA Journal, April 1968, Vol. 6, No. 4, pp. 603-607.

6. P.F. Holloway and E.L. Morrisette, "Roughness Effects on Boundary-Layer Transition for Blunt-Leading-Edge Plates at Mach 6", TND-3517, Aug. 1966, NASA.

7. P.S. Klebanoff, G.B. Schubauer, and K.D. Tidstrom, "Measurements of the Effect of Two-Dimensional and Three-Dimensional Roughness Elements on Boundary-Layer Transition", Journal of the Aeronautical Sciences, Nov. 1955, Vol. 22, No. 11, pp. 803-804.

8. J.C. Cooke, "An Axially Symmetric Analogue for General Three-Dimensional Boundary Layers," British Aeronautical Research Council, R&M 3200, 1961.

9. G.J. van Wylen, Thermodynamics, John Wiley and Sons, Inc., New York, 1959.

10. W.H. Dorrance, Viscous Hypersonic Flow, McGraw-Hill Book Company, New York, 1962.

11. J.A. Sills, "Transformations for Infinite Regions and Their Applications to Flow Problems," AIAA Journal, Jan. 1969, Vol. 7, No. 1, pp 117-123.

12. C.F. Hansen, "Approximations for the Temperature and Transport Properties of High-Temperature Air", TR R-50, Nov. 1957, NACA.

13. ———, "Equations, Tables, and Charts for Compressible Flow", Report 1135, 1953, NACA.

14. H. Schlichting, Boundary Layer Theory, McGraw-Hill Book Company, New York, 1968.

15. R.W. Detra; N.H. Kemp; and F.R. Riddell, "Addendum to Heat Transfer to Satellite Vehicles Reentering the Atmosphere", Jet Propulsion, December 1957, Vol. 27, No. 12, pp. 1256-1257.

16. J.A. Fay and F.R. Riddell, "Theory of Stagnation Point Heat Transfer in Dissociated Air", Journal of the Aeronautical Sciences, Feb. 1958, Vol. 25, No. 2, pp. 73-85, 121.

17. H. Tong, A.C. Buckingham, and H.L. Morse," Nonequilibrium Chemistry Boundary Layer Integral Matrix Procedure", Aerotherm Final Report No. 73-67, July 1973, the Acurex Corporation.

Table 1. - The input boundary conditions for Space Shuttle Orbiter Flight Design Trajectory.

(a) M_∞ = 9.49; altitude = 162,000 ft; angle of attack = 30.83°; P_{t2} = 215.8 lbf/ft^2; T_{t2} = 5,508°R.

M	x(ft)	p_e/p_{t2}	T_w(°R)	S_e/R	RDS(ft)
1	0.8325	0.9164	2265.	37.24	0.8225
2	1.0113	0.8900	2251.	37.23	0.9900
3	1.1900	0.8595	2238.	37.22	1.1500
4	1.5188	0.8120	2211.	37.19	1.4600
5	1.8475	0.7687	2182.	37.15	1.7500
6	2.1450	0.7310	2154.	37.10	2.0100
7	2.4425	0.6992	2124.	37.07	2.2500
8	2.7088	0.6710	2097.	37.06	2.5000
9	2.9750	0.6475	2071.	37.05	2.7100
10	3.2875	0.6190	2041.	37.04	2.9600
11	3.6000	0.5930	2012.	37.03	3.1800
12	4.1625	0.5540	1964.	36.99	3.6100
13	4.7250	0.5227	1923.	36.95	4.0230
14	5.2875	0.4990	1887.	36.91	4.4250
15	5.8500	0.4780	1859.	36.88	4.8000
16	6.3875	0.4600	1834.	36.85	5.1800
17	6.9250	0.4454	1815.	36.82	5.5480
18	7.4750	0.4310	1799.	36.79	5.9000
19	8.0250	0.4182	1784.	36.77	6.2600
20	8.6000	0.4060	1770.	36.74	6.6300
21	9.1000	0.3968	1760.	36.72	6.9450
22	9.6500	0.3870	1750.	36.69	7.2800
23	10.2000	0.3770	1740.	36.68	7.6200
24	10.7380	0.3690	1733.	36.65	7.9450
25	11.275	0.3610	1727.	36.63	8.2700

Table 1. - (a) Continued.

M	x(ft)	p_e/p_{t2}	T_w(°R)	S_e/R	RDS(ft)
26	11.813	0.3540	1723.	36.60	8.5890
27	12.350	0.3477	1720.	36.58	8.9075
28	12.888	0.3415	1717.	36.56	9.2160
29	13.425	0.3360	1715.	36.53	9.5250
30	13.963	0.3300	1712.	36.51	9.8340
31	14.500	0.3255	1710.	36.49	10.143
32	15.575	0.3170	1706.	36.44	10.738
33	16.650	0.3086	1701.	36.40	11.333
34	17.713	0.3020	1691.	36.36	11.925
35	18.775	0.2955	1675.	36.31	12.518
36	20.388	0.2880	1612.	36.25	13.363
37	22.000	0.2819	1557.	36.19	14.208
38	24.680	0.2770	1537.	36.07	15.599
39	27.360	0.2751	1530.	36.96	16.990
40	30.030	2.2760	1526.	35.85	18.399
41	32.700	0.2772	1522.	35.76	19.808
42	35.385	0.2780	1518.	35.68	21.174
43	38.070	0.2795	1515.	35.62	22.540
44	40.735	0.2800	1512.	35.56	23.920
45	43.400	0.2810	1510.	35.50	25.300
46	46.085	0.2820	1507.	35.44	26.695
47	48.770	0.2835	1494.	35.39	28.090
48	51.435	0.2843	1502.	35.34	29.480
49	54.100	0.2850	1500.	35.29	30.870
50	56.785	0.2860	1493.	35.24	32.250

Table 1. - Continued.

(b) M_∞ = 16.05; altitude = 199,000 ft; angle of attack = 31.8; p_{t2} = 148.84 psf, T_{t2} = 9,385°R

M	x(ft)	p_e/p_{te}	T_w(°R)	S_e/R	RDS(ft)
1	1.1500	0.8975	2920.	44.62	1.1200
2	1.5667	0.8440	2840.	44.54	1.5200
3	1.9833	0.7960	2750.	44.43	1.8900
4	2.4000	0.7510	2670.	44.31	2.2600
5	2.7867	0.7160	2605.	44.21	2.5900
6	3.1733	0.6810	2550.	44.12	2.9100
7	3.5600	0.6512	2510.	44.04	3.2300
8	4.1300	0.6150	2470.	43.93	3.7000
9	4.7000	0.5853	2440.	43.83	4.1400
10	5.2500	0.5590	2410.	43.74	4.5700
11	5.8000	0.5365	2380.	43.65	4.9800
12	6.3500	0.5165	2365.	43.57	5.4000
13	6.9000	0.5008	2350.	43.47	5.7900
14	7.4400	0.4860	2344.	43.39	6.2000
15	7.9800	0.4717	2340.	43.30	6.5700
16	8.5300	0.4590	2323.	43.23	6.9400
17	9.0800	0.4473	2290.	43.15	7.3100
18	9.6400	0.4370	2262.	43.06	7.6900
19	1.0200	0.4282	2240.	42.97	8.0500
20	1.0750	0.4200	2222.	42.87	8.4000
21	1.1300	0.4121	2203.	42.78	8.7600
22	1.1850	0.4050	2186.	42.65	9.1200
23	1.2400	0.3976	2169.	42.51	9.4800
24	1.2900	0.3920	2155.	42.37	9.8500
25	1.3400	0.3856	2142.	42.26	1.0200
26	1.3950	0.3800	2130.	42.22	1.0610
27	1.4500	0.3747	2120.	42.20	1.1000
28	1.5550	0.3650	2100.	42.17	1.1650

Table 1. - (b) Continued.

M	x(ft)	p_e/p_{te}	$T_w(^{\circ}R)$	S_e/R	RDS(ft)
29	1.6600	0.3566	2080.	42.12	1.2200
30	1.7700	0.3470	2060.	42.03	1.2900
31	1.8800	0.3400	2040.	41.91	1.3500
32	2.0400	0.3310	2020.	41.77	1.4400
33	2.2000	0.3234	2000.	41.69	1.5400
34	2.4700	0.3210	1970.	41.55	1.7000
35	2.7400	0.3203	1950.	41.40	1.8500
36	3.0050	0.3203	1930.	41.29	1.9900
37	3.2700	0.3203	1910.	41.18	2.1600
38	3.5400	0.3203	1890.	41.05	2.3200
39	3.8100	0.3203	1880.	40.94	2.4800
40	4.0750	0.3203	1860.	40.84	2.6300
41	4.3400	0.3203	1850.	40.73	2.7900
42	4.6100	0.3203	1835.	40.61	2.9400
43	4.8800	0.3203	1820.	40.51	3.1000
44	5.1450	0.3203	1810.	40.41	3.2500
45	5.4100	0.3203	1800.	40.81	3.4000
46	5.6800	0.3203	1790.	40.22	3.5600
47	5.9500	0.3203	1780.	40.14	3.7300
48	6.2150	0.3203	1770.	40.04	3.8800
49	6.4800	0.3203	1760.	39.95	4.0400

Table 1. - Continued.

(c) M_∞ = 22.04; altitude = 226,000 ft; angle of attack = 40.2°; P_{t2} = 89.020 lbf/ft^2; T_{t2} = 10,357°R.

M	x (ft)	p_e/p_{te}	T_w(°R)	S_e/R	RDS(ft)
1	1.3910	0.9170	3130.	49.62	1.3700
2	1.7040	0.8940	3080.	49.59	1.6600
3	2.0175	0.8704	3030.	49.51	1.9550
4	2.3070	0.8510	2990.	49.41	2.2100
5	2.5960	0.8330	2955.	49.30	2.4800
6	2.8860	0.8150	2922.	49.19	2.7400
7	3.1750	0.7989	2890.	49.06	3.0000
8	3.4620	0.7830	2865.	48.92	3.2400
9	3.7500	0.7680	2840.	48.79	3.4900
10	4.0370	0.7530	2814.	48.68	3.7200
11	4.3250	0.7402	2790.	48.58	3.9500
12	4.6920	0.7240	2760.	48.43	4.2600
13	5.0580	0.7070	2734.	48.31	4.5600
14	5.4250	0.6923	2712.	48.20	4.8500
15	5.9740	0.6720	2683.	48.07	5.2900
16	6.5250	0.6553	2655.	47.96	5.7250
17	7.0620	0.6390	2630.	47.87	6.1600
18	7.6000	0.6244	2610.	47.77	6.5750
19	8.1500	0.6110	2586.	47.70	6.9700
20	8.7000	0.5981	2565.	47.64	7.4000
21	9.2380	0.5880	2548.	47.58	7.8000
22	9.7750	0.5770	2530.	47.52	8.2000
23	10.313	0.5670	2510.	47.47	8.6000
24	10.850	0.5587	2490.	47.43	9.0000
25	11.388	0.5510	2477.	47.39	9.3800

Table 1. - (c) Continued.

M	x(ft)	p_e/p_{t2}	T_w(°R)	S_e/R	RDS(ft)
26	11.925	0.5436	2462.	47.36	9.7750
27	12.463	0.5380	2450.	47.32	10.160
28	13.000	0.5297	2435.	47.30	10.550
29	13.538	0.5250	2422.	47.27	10.920
30	14.075	0.5183	2410.	47.25	11.300
31	15.150	0.5070	2390.	47.20	12.060
32	16.225	0.4967	2375.	47.16	12.800
33	18.375	0.4787	2330.	47.05	14.250
34	19.975	0.4690	2308.	46.95	15.300
35	21.575	0.4590	2288.	46.84	16.400
36	24.250	0.4553	2260.	46.65	18.100
37	26.925	0.4553	2235.	46.48	19.925
38	29.600	0.4553	2215.	46.30	21.700
39	32.275	0.4553	2195.	46.14	23.475
40	34.963	0.4553	2180.	45.99	25.200
41	37.650	0.4553	2166.	45.85	27.000
42	40.325	0.4553	2149.	45.72	28.700
43	43.000	0.4553	2130.	45.59	30.525
44	45.675	0.4553	2118.	45.48	32.300
45	48.350	0.4553	2103.	45.37	34.050
46	51.025	0.4553	2090.	45.25	35.900
47	53.700	0.4553	2076.	45.15	37.575
48	56.375	0.4553	2065.	45.05	39.400
49	59.050	0.4553	2053.	44.95	41.111

Table 1. - Continued.

(d) M_∞ = 29.86; altitude = 246,000 ft; angle of attack = 41.4°; p_{t2} = 46.26 lbf/ft^2; T_{t2} = 10,798°R.

M	x(ft)	p_e/p_{t2}	T_w(°R)	S_e/R	RDS(ft)
1	1.9500	0.8950	3095.	54.13	1.8900
2	2.0470	0.8890	3076.	54.09	1.9800
3	2.1430	0.8840	3061.	54.03	2.0600
4	212400	0.8780	3048.	53.97	2.1500
5	2.3370	0.8740	3037.	53.92	2.2300
6	2.5300	0.8640	3016.	53.81	2.4100
7	2.7230	0.8540	2996.	53.70	2.5900
8	2.9200	0.8440	2977.	53.60	2.7700
9	3.1100	0.8355	2960.	53.50	2.9300
10	3.3000	0.8260	2942.	53.39	3.1000
11	3.4900	0.8170	2927.	53.29	3.2700
12	3.6800	0.8090	2912.	53.20	3.4300
13	3.8700	0.8000	2897.	53.10	3.6000
14	4.0600	0.7920	2883.	53.01	3.7500
15	4.2500	0.7837	2869.	52.92	3.9100
16	4.6170	0.7680	2839.	52.76	4.2300
17	4.9830	0.7530	2812.	52.61	4.5300
18	5.3500	0.7390	2784.	52.48	4.8400
19	5.7170	0.7250	2758.	52.36	5.1500
20	6.0830	0.7125	2732.	52.26	5.4300
21	6.4500	0.7006	2707.	52.19	5.7300
22	6.8100	0.6900	2684.	52.11	6.0200
23	7.1700	0.6790	2660.	52.05	6.3200
24	7.5300	0.6677	2637.	51.99	6.5900
25	7.8970	0.6590	2614.	51.93	6.8800

Table 1. - (d) Conclusion.

M	x(ft)	p_e/p_{t2}	T_w(°R)	S_e/R	RDS(ft)
26	8.2630	0.6500	2595.	51.87	7.1700
27	8.6300	0.6411	2577.	51.82	7.4300
28	9.1700	0.6290	2552.	51.75	7.8300
29	9.7100	0.6175	2535.	51.68	8.2500
30	10.255	0.6080	2522.	51.61	8.6500
31	10.800	0.5990	2511.	51.54	9.0300
32	11.350	0.5900	2499.	51.46	9.4600
33	11.900	0.5815	2488.	51.37	9.8400
34	12.400	0.5740	2479.	51.30	10.230
35	12.900	0.5667	2470.	51.24	10.600
36	13.450	0.5603	2460.	51.18	11.100
37	14.000	0.5540	2450.	51.13	11.600
38	15.050	0.5425	2433.	51.05	12.250
39	16.100	0.5313	2419.	51.02	12.900
40	17.200	0.5210	2403.	50.95	13.610
41	18.300	0.5128	2388.	50.88	14.400
42	19.900	0.4990	2365.	50.77	15.600
43	21.500	0.4912	2345.	50.68	16.700
44	24.200	0.4880	2311.	50.55	18.400
45	26.900	0.4874	2281.	50.45	20.300
46	29.550	0.4874	2259.	50.36	22.100
47	32.200	0.4874	2237.	50.25	23.900
48	34.900	0.4874	2218.	50.10	25.700
49	37.600	0.4874	2200.	49.95	27.500
50	40.250	0.4874	2182.	49.80	29.300
51	42.900	0.4874	2166.	49.65	31.200
52	45.600	0.4874	2151.	49.52	32.900
53	48.300	0.4874	2137.	49.39	34.800
54	50.950	0.4874	2122.	49.25	36.600

Table 2. - Transport Properties

(a) Perfect-gas model

T (°R)	$\mu \times 10^6$ $\left(\frac{\text{lbf sec}}{\text{ft}^2}\right)$	$k \times 10^6$ $\left(\frac{\text{Btu}}{\text{ft sec °R}}\right)$	C_p $\left(\frac{\text{Btu ft}}{\text{lbf sec}^2\text{ °R}}\right)$	Pr (-)
200	0.1611	1.7801	7.7346	0.7
300	0.2366	2.6143		
400	0.3034	3.3574		
500	0.3633	4.0143		
600	0.4178	4.6165		
700	0.4678	5.1689		
800	0.5144	5.6838		
900	0.5579	6.164		
1300	0.7100	7.845		
1700	0.8380	9.259		
2100	0.9504	10.50		
2500	1.051	11.61		
2900	1.144	12.64		
3300	1.230	13.59		
3700	1.310	14.47		
4100	1.386	15.31		
4500	1.458	16.11		
4900	1.527	16.87		
5300	1.593	17.60		
5700	1.656	18.30		
6100	1.717	18.97		
7000	1.847	20.41		
7900	1.968	21.75		
8800	2.082	23.01		
9700	2.191	24.21		
10600	2.294	25.35		
11500	2.393	26.44	7.7346	0.7

Table 2. - Continued.

(b) Real-gas model, properties for
p = 1.0 atm. (data from Ref. 12)

T (°R)	$\mu \times 10^6$ $\left(\frac{lbf\ sec}{ft^2}\right)$	$k \times 10^6$ $\left(\frac{Btu}{ft\ sec\ °R}\right)$	C_p $\left(\frac{Btu\ ft}{lbf\ sec^2\ °R}\right)$	Pr (-)
200	0.1611	1.7801	7.7346	0.7
300	0.2366	2.6143		
400	0.3034	3.3574		
500	0.3633	4.0143		
600	0.4178	4.6165		
700	0.4678	5.1689		
800	0.5144	5.6838	7.7346	0.7
900	0.558	5.963	7.887	0.738
1800	0.808	10.01	9.366	0.756
2700	1.100	13.26	9.246	0.767
3600	1.293	15.95	9.535	0.773
4500	1.461	24.79	11.81	0.696
5400	1.612	54.08	21.03	0.627
6300	1.756	86.61	32.55	0.660
7200	1.909	58.87	23.50	0.762
8100	2.057	35.99	13.16	0.752
9000	2.201	72.71	20.18	0.611
9900	2.353	139.6	34.59	0.583
10800	2.529	247.6	58.94	0.602
11700	2.756	368.3	89.94	0.673
12600	3.044	414.2	108.31	0.796
13500	3.349	334.2	92.51	0.927
14400	3.688	220.0	58.64	0.983

Table 2. - Continued.

(c) Real-gas model, properties for
$p = 0.1$ atm. (data from Ref. 12)

T (°R)	$\mu \times 10^6$ $\left(\frac{\text{lbf sec}}{\text{ft}^2}\right)$	$k \times 10^6$ $\left(\frac{\text{Btu}}{\text{ft sec °R}}\right)$	C_p $\left(\frac{\text{Btu ft}}{\text{lbf sec}^2\text{ °R}}\right)$	P_r (-)
200	0.1611	1.7801	7.7346	0.7
300	0.2366	2.6143		
400	0.3034	3.3574		
500	0.3633	4.0143		
600	0.4178	4.6165		
700	0.4678	5.1689		
800	0.5144	5.6838	7.7346	0.7
900	0.558	5.963	7.887	0.738
1800	0.868	10.01	8.718	0.756
2700	1.100	13.26	9.246	0.767
3600	1.293	16.95	10.04	0.766
4500	1.461	38.28	16.90	0.645
5400	1.612	92.61	36.54	0.636
6300	1.762	72.67	30.69	0.744
7200	1.917	31.50	12.47	0.759
8100	2.065	69.72	20.60	0.610
9000	2.218	158.7	41.57	0.581
9900	2.411	319.4	81.74	0.617
10800	2.663	455.5	125.9	0.736
11700	2.974	390.9	119.1	0.906
12600	3.261	219.6	66.4	0.986
13500	3.477	161.6	45.0	0.969
14400	3.688	96.44	16.9	0.648

Table 2. - Continued.

(d) Real-gas model, properties for $p = 0.01$ atm. (data from Ref. 12)

T (°R)	$\mu \times 10^6$ $\left(\frac{\text{lbf sec}}{\text{ft}^2}\right)$	$k \times 10^6$ $\left(\frac{\text{Btu}}{\text{ft sec °R}}\right)$	C_p $\left(\frac{\text{Btu ft}}{\text{lbf sec}^2\text{ °R}}\right)$	Pr (-)
200	0.1611	1.7801	7.7346	0.7
300	0.2366	2.6143	|	|
400	0.3034	3.3574	|	|
500	0.3633	4.0143	|	|
600	0.4178	4.6165	|	|
700	0.4678	5.1689	|	|
800	0.5144	5.6838	7.7346	0.7
900	0.558	5.963	7.887	0.738
1800	0.868	10.01	8.718	0.756
2700	1.100	13.26	9.246	0.767
3600	1.293	19.78	11.08	0.724
4500	1.461	70.89	29.65	0.611
5400	1.612	84.84	38.95	0.740
6300	1.769	31.54	13.14	0.737
7200	1.920	57.30	18.47	0.619
8100	2.075	154.1	42.93	0.578
9000	2.266	367.5	101.2	0.624
9900	2.544	517.3	159.6	0.785
10800	2.849	318.1	108.2	0.969
11700	3.088	139.4	43.11	0.955
12600	3.319	86.59	21.65	0.830
13500	3.490	235.3	28.59	0.424
14400	3.623	394.5	42.14	0.387

Table 2. - Continued.

(e) Real-gas model, properties averaged for those p = 0.01 atm. and 0.1 atm. (data from Ref. 12)

T (°R)	$\mu \times 10^6$ $\left(\frac{\text{lbf sec}}{\text{ft}^2}\right)$	$k \times 10^6$ $\left(\frac{\text{Btu}}{\text{ft sec °R}}\right)$	C_p $\left(\frac{\text{Btu ft}}{\text{lbf sec}^2\ \text{°R}}\right)$	Pr (-)
200	0.1611	1.7801	7.7346	0.7
300	0.2366	2.6143		
400	0.3034	3.3574		
500	0.3633	4.0143		
600	0.4178	4.6165		
700	0.4678	5.1689		
800	0.5144	5.6838	7.7346	0.7
900	0.558	5.963	7.887	0.738
1800	0.868	10.01	8.718	0.756
2700	1.100	13.26	9.246	0.767
3600	1.293	18.37	10.58	0.745
4500	1.461	54.59	23.47	0.628
5400	1.612	88.73	37.87	0.688
6300	1.766	52.11	21.86	0.741
7200	1.919	44.40	15.94	0.689
8100	2.070	111.9	32.11	0.594
9000	2.242	263.1	70.76	0.603
9900	2.478	418.4	118.4	0.701
10800	2.756	386.8	119.7	0.853
11700	3.031	265.2	81.46	0.931
12600	3.290	153.1	42.25	0.908
13500	3.484	198.5	39.71	0.697
14400	3.656	245.5	34.78	0.518

Table 2. - Concluded.

(f) Real-gas model, properties for $p = 0.001$ atm. (data from Ref. 12)

T (°R)	$\mu \times 10^6$ $\left(\frac{lbf\ sec}{ft^2}\right)$	$k \times 10^6$ $\left(\frac{Btu}{ft\ sec\ °R}\right)$	C_p $\left(\frac{Btu\ ft}{lbf\ sec^2\ °R}\right)$	Pr (-)
200	0.1611	1.7801	7.7346	0.7
300	0.2366	2.6143		
400	0.3034	3.3574		
500	0.3633	4.0143		
600	0.4178	4.6165		
700	0.4678	5.1689		
800	0.5144	5.6838		
900	0.558	6.1656		
1800	0.8674	9.5843	7.7346	0.7
2700	1.100	13.2595	9.2455	0.767
3600	1.293	28.3195	14.6533	0.668
4500	1.461	117.4277	52.6733	0.654
5400	1.612	37.011	17.1368	0.745
6300	1.7642	38.7185	14.441	0.658
7200	1.920	118.9276	35.937	0.58
8100	2.10378	370.65	107.6477	0.611
9000	2.3767	570.18	191.6834	0.799
9900	2.67697	265.62	98.1327	0.989
10800	2.91178	26.228	29.4456	0.891
11700	3.10492	150.368	22.471	0.464
12600	3.26861	289.08	35.7303	0.404
13500	3.3972	545.181	59.5372	0.371
14400	3.439287	978.54	99.8659	0.351

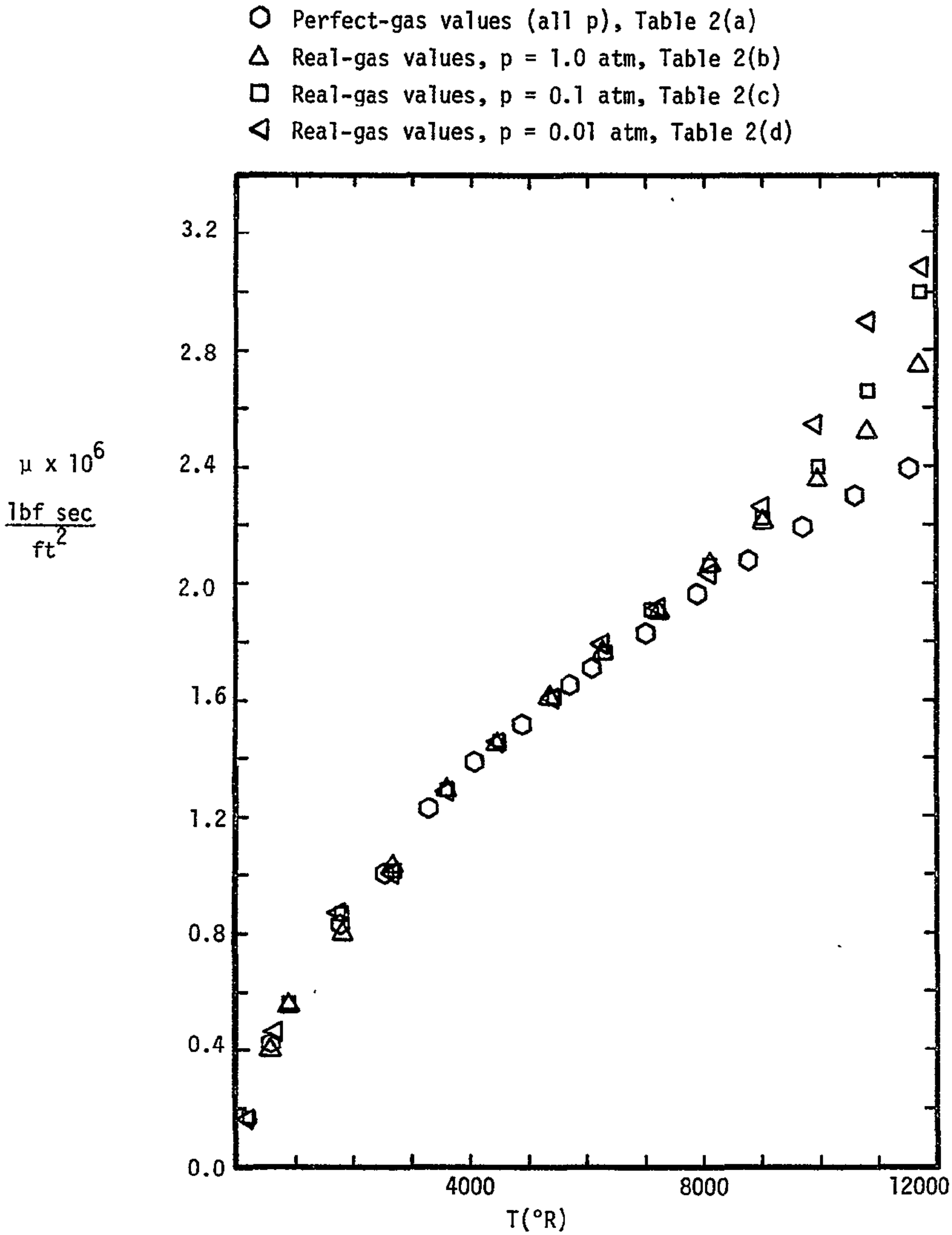

Figure 1. - Viscosity.

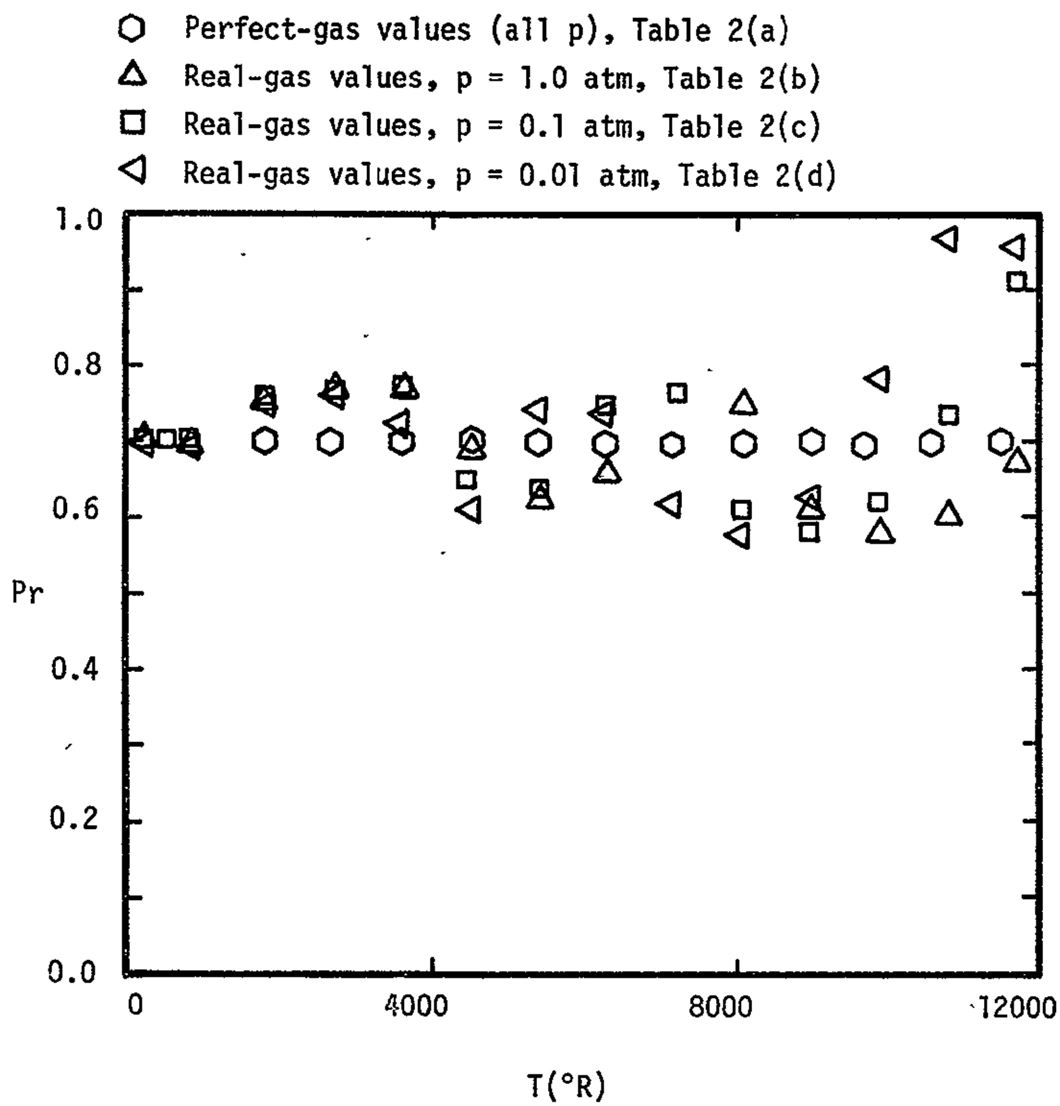

Figure 2. - Prandtl Number

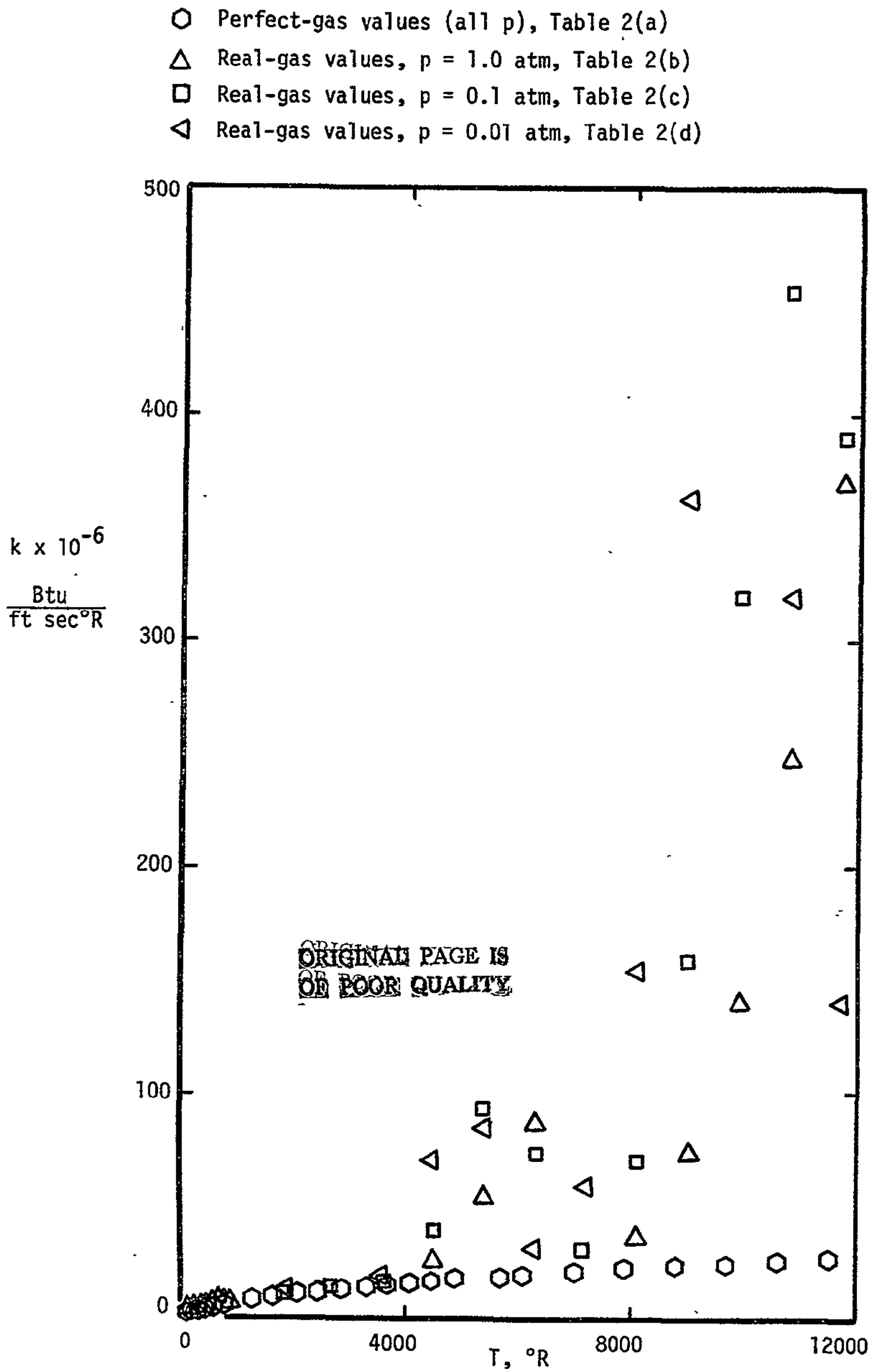

(a) Thermal conductivity

Figure 3. - Third basic transport property and the derived transport property

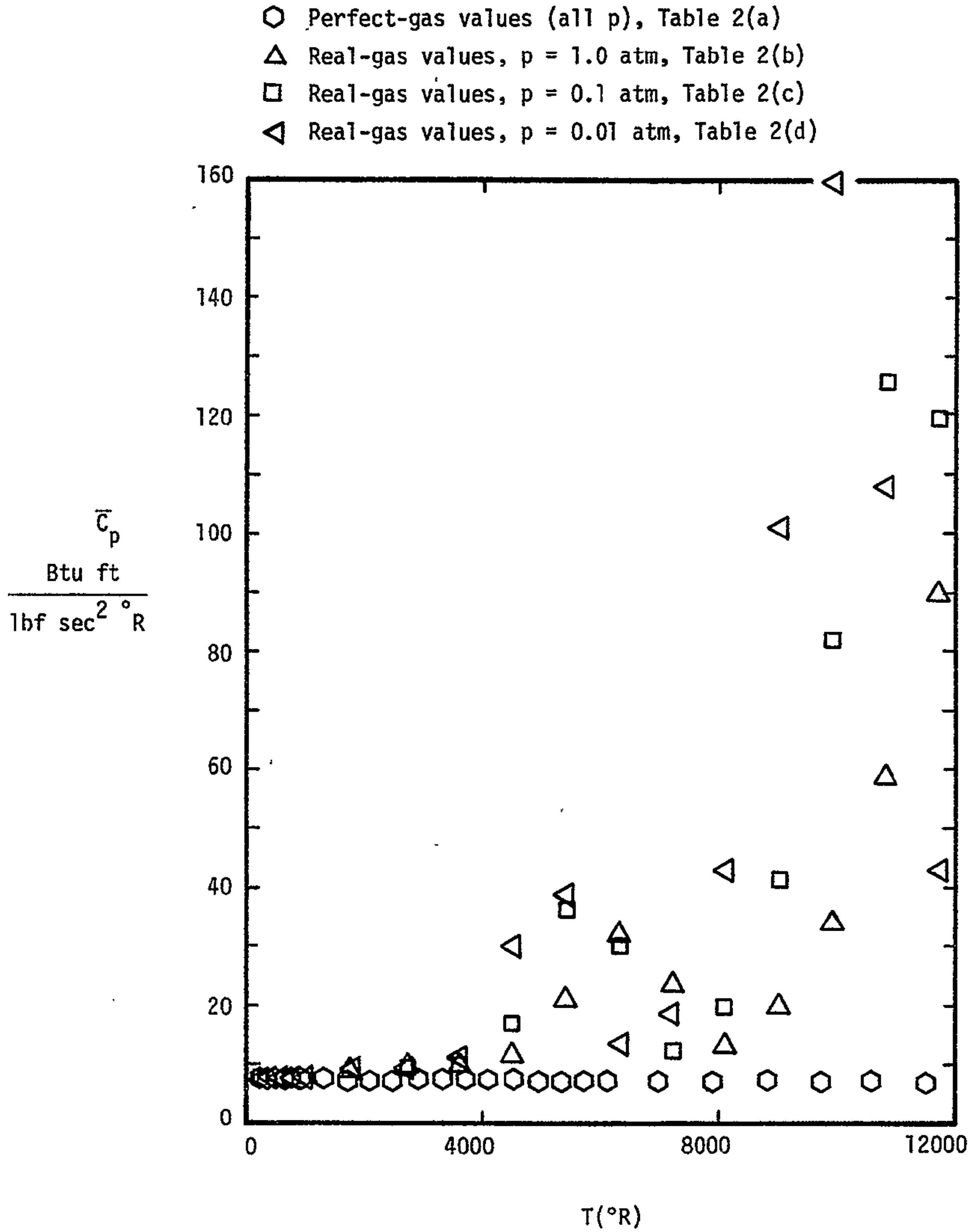

(b) Specific heat

Figure 3. - Concluded.

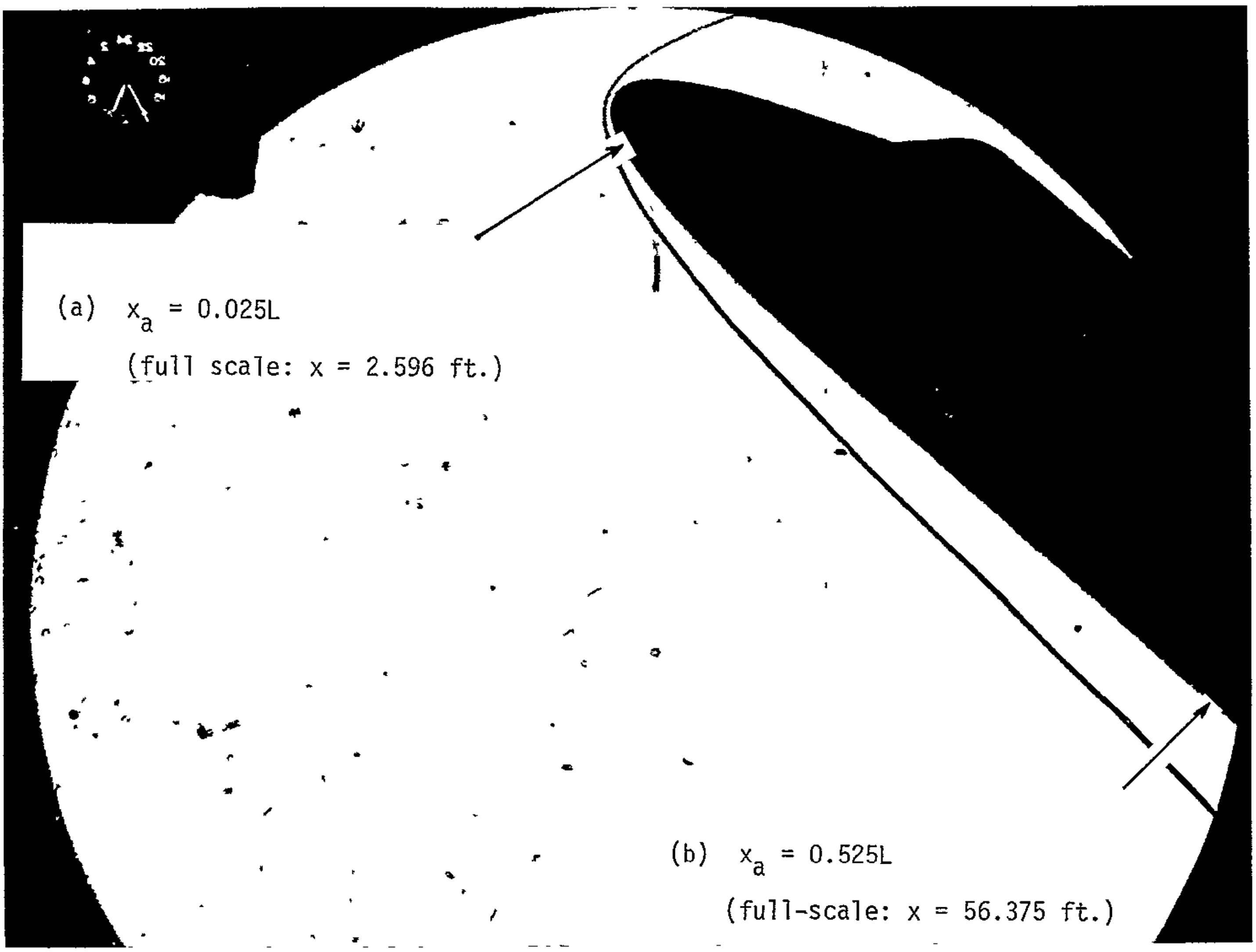

Figure 4. The locations of the two streamline stations for which detailed boundary-layer profiles are presented. Photograph is for α = 40°

Transport Model

◇ Linear interpolation of values of Ref. 12

○ Perfect-gas model, Table 2(a)

△ Real-gas model, p = 1.0 atm., Table 2(b)

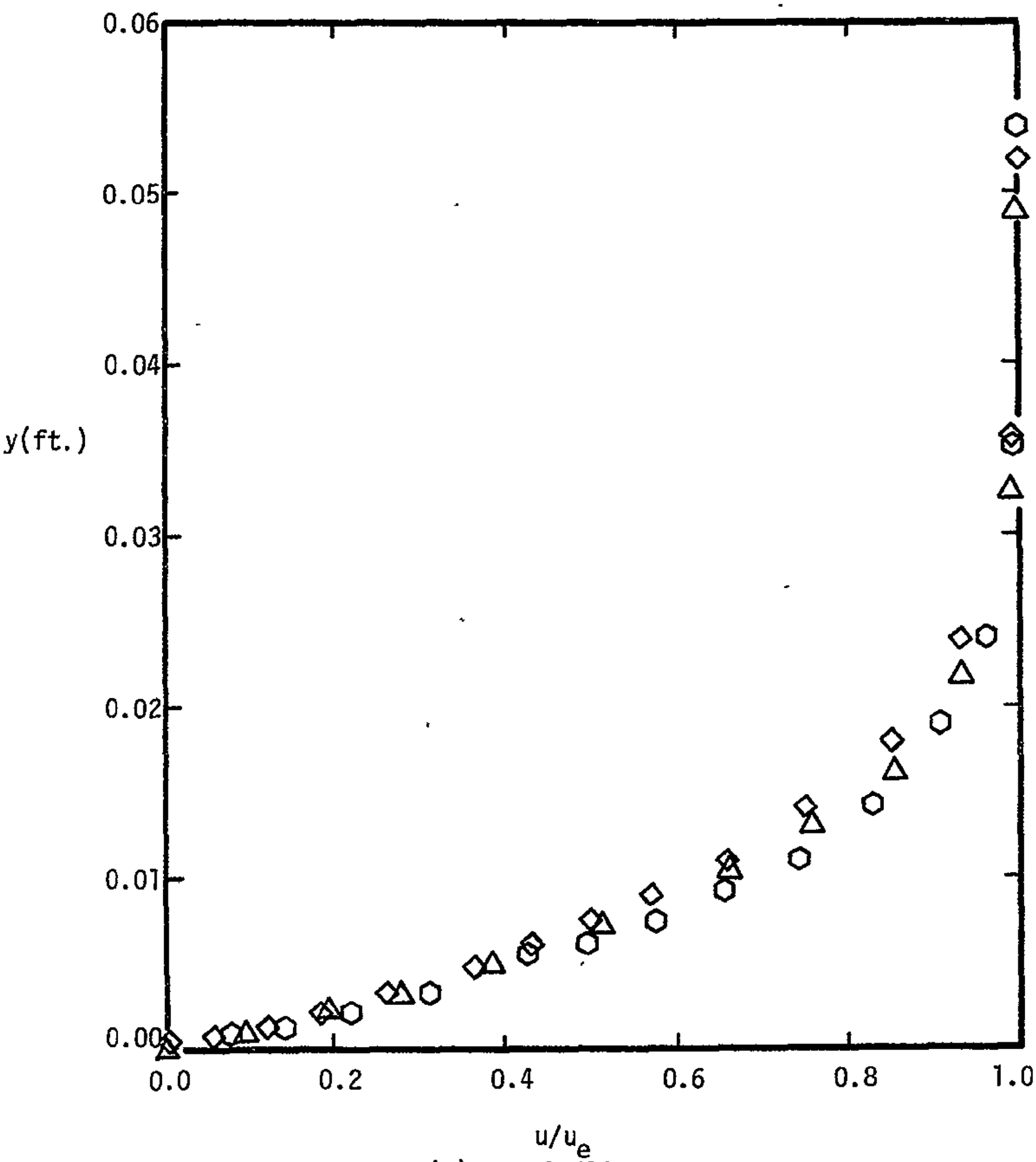

(a) x = 2.596 ft.

Figure 5. - The effect of transport property model on the velocity profile, $M_\infty = 22.04$.

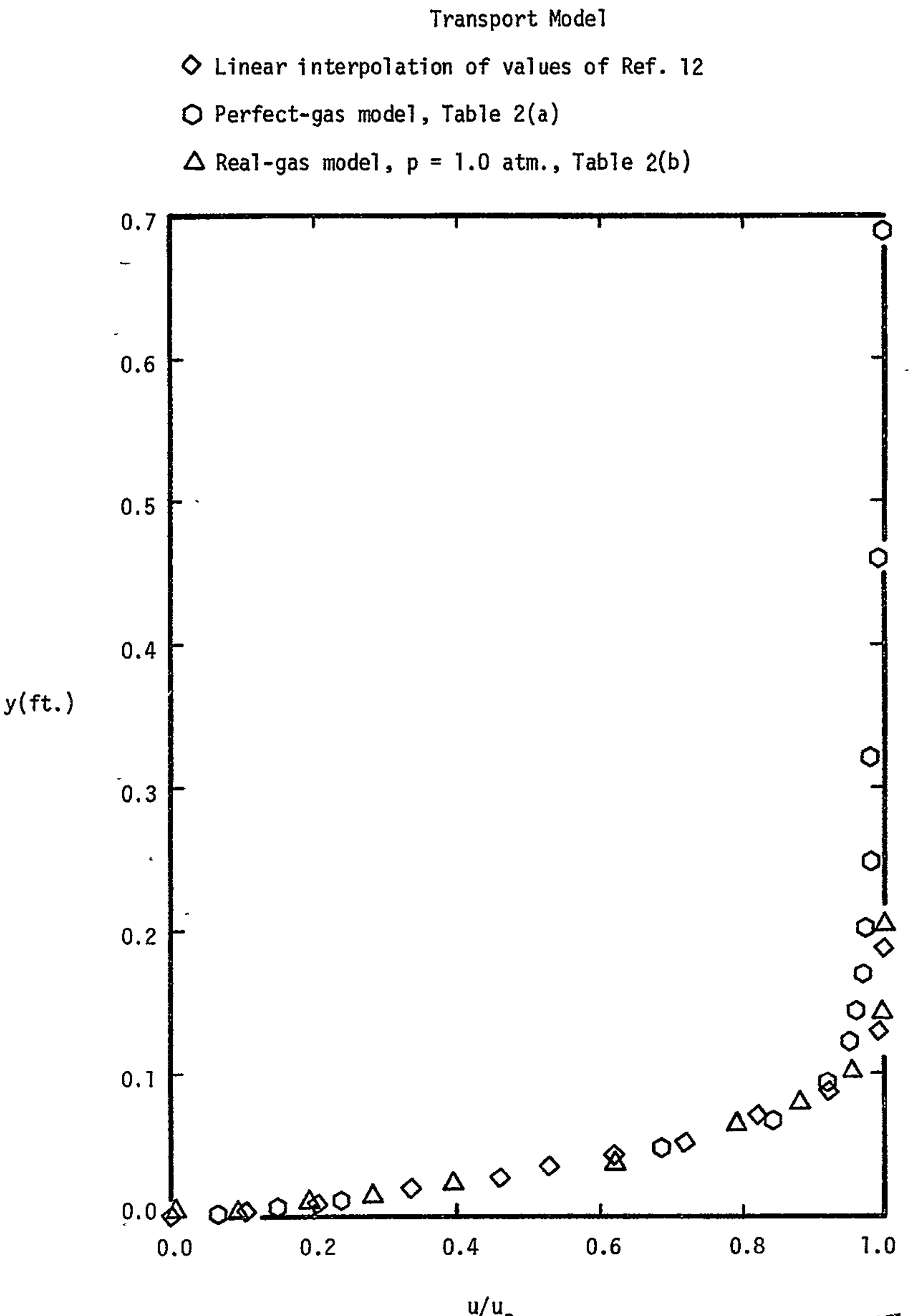

(b) x = 56.375 ft.
Figure 5. - Concluded.

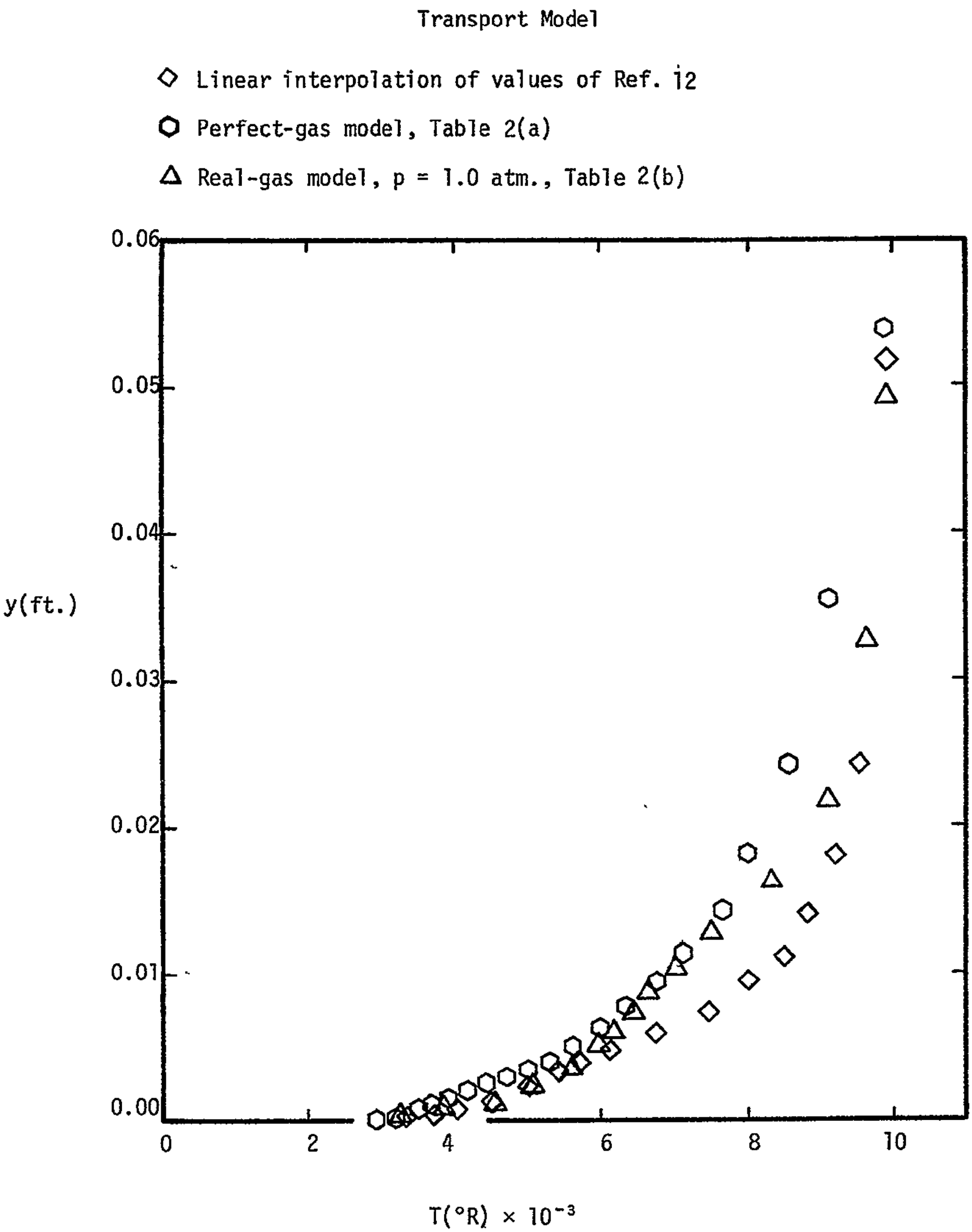

(a) x = 2.596 ft.

Figure 6. - The effect of the transport property model on the temperature profile, $M_\infty = 22.04$.

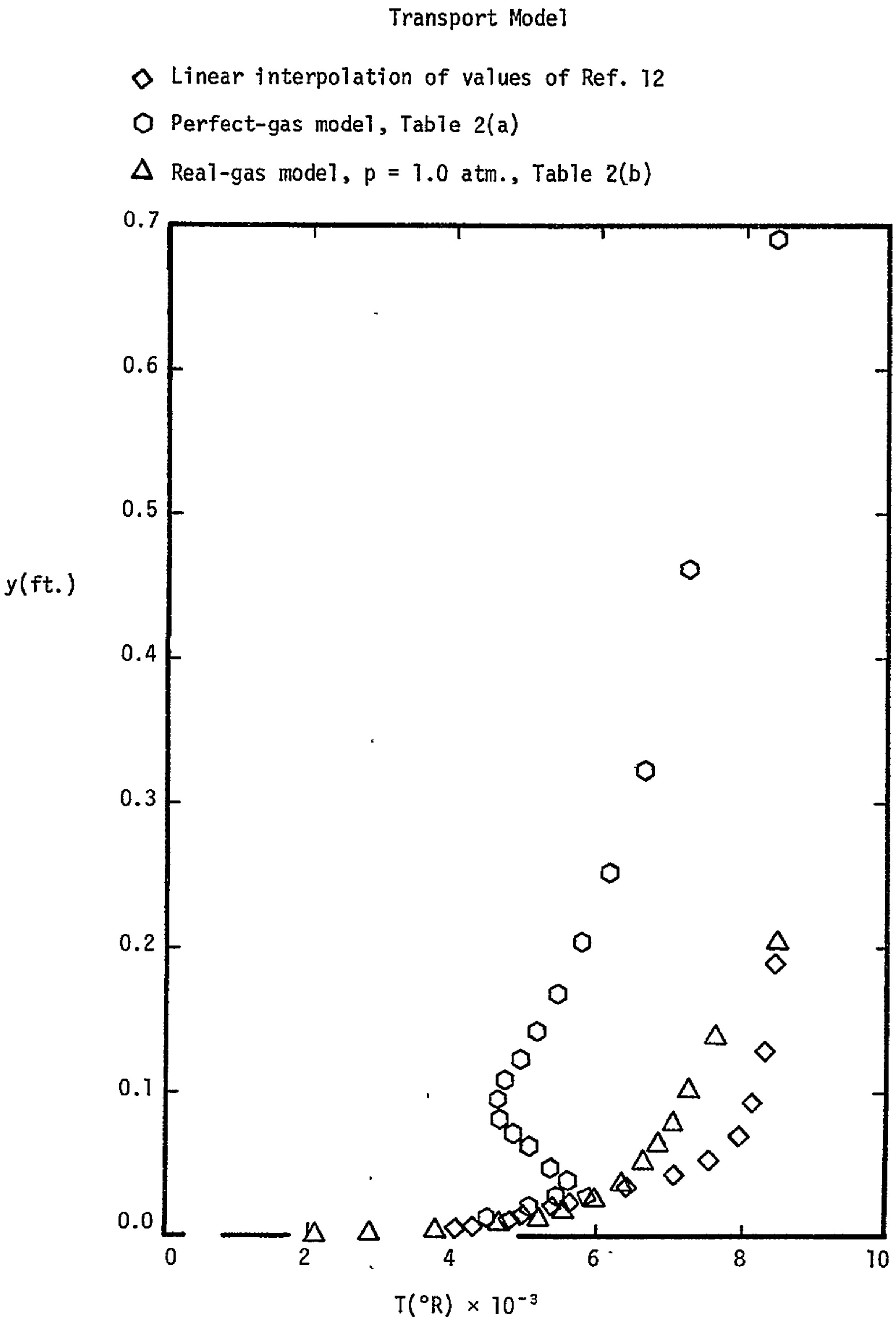

(b) $\bar{x}$ = 56.375 ft.

Figure 6. - Concluded.

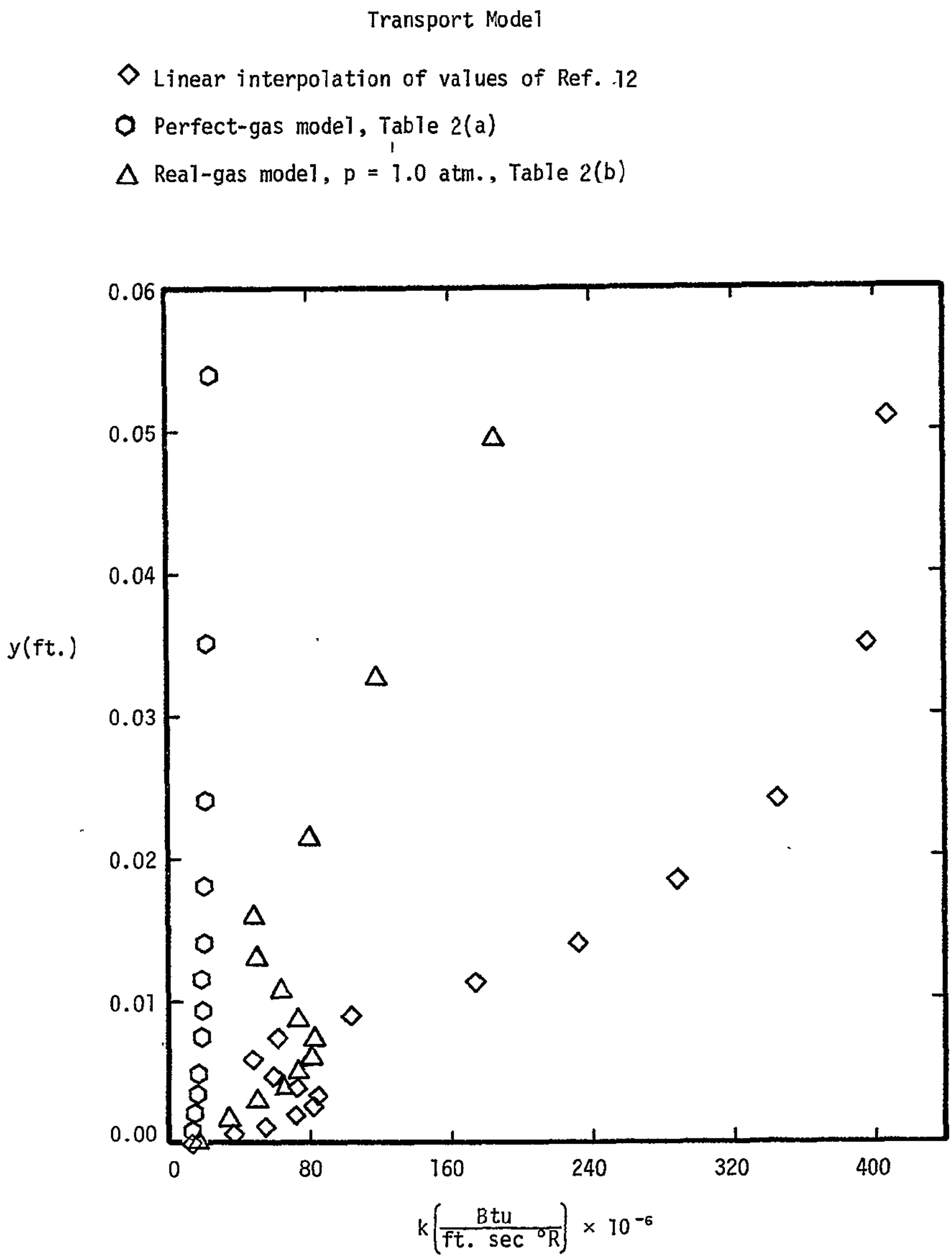

(a) $x = 2.596$ ft.

Figure 7. - The variation of the thermal conductivity for the various transport models, $M_\infty = 22.04$.

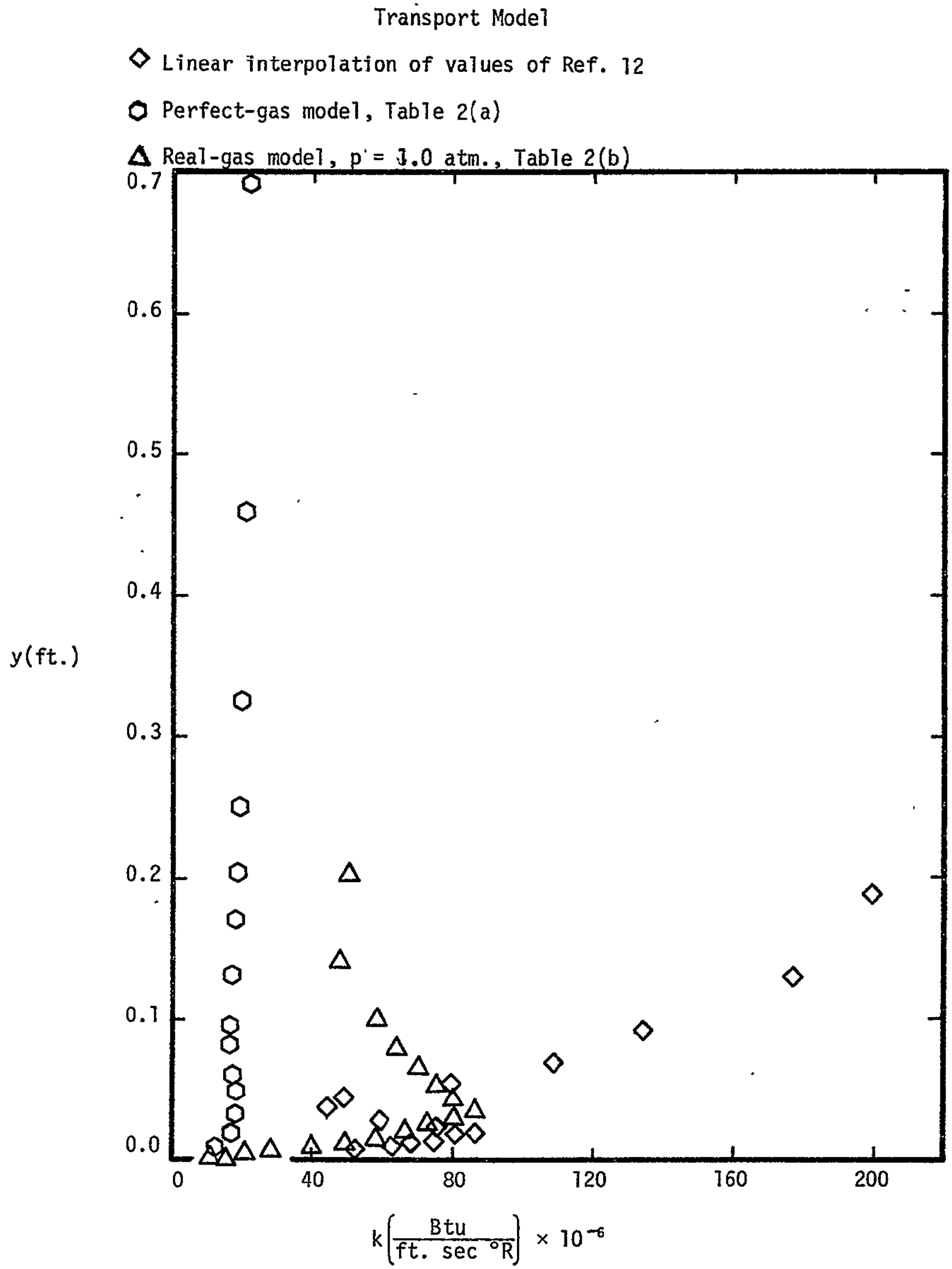

(b) x = 56.375 ft.

Figure 7. - Concluded.

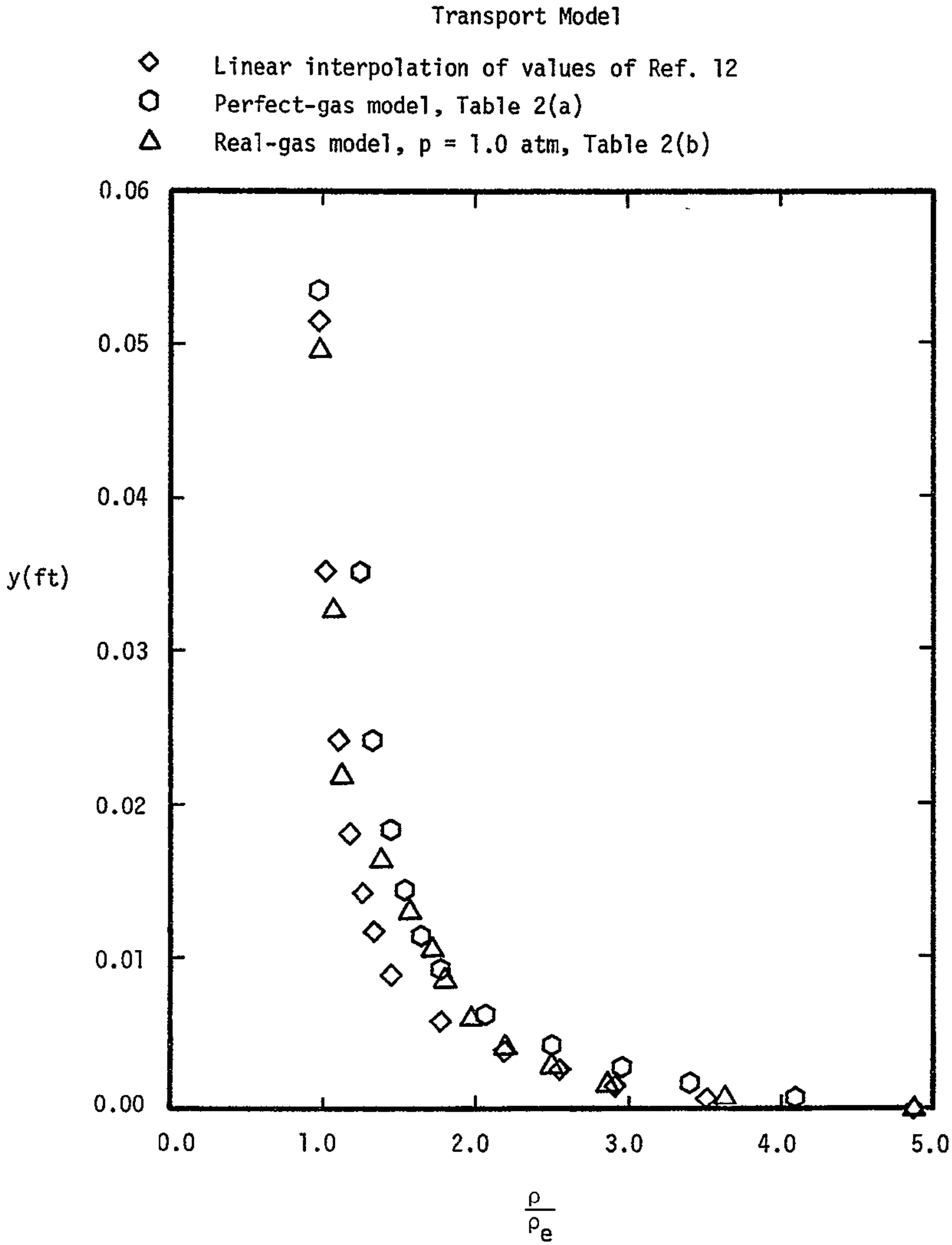

(a) x = 2.596 ft

Figure 8. - The effect of the transport property model on the density profile, $M_\infty = 22.04$.

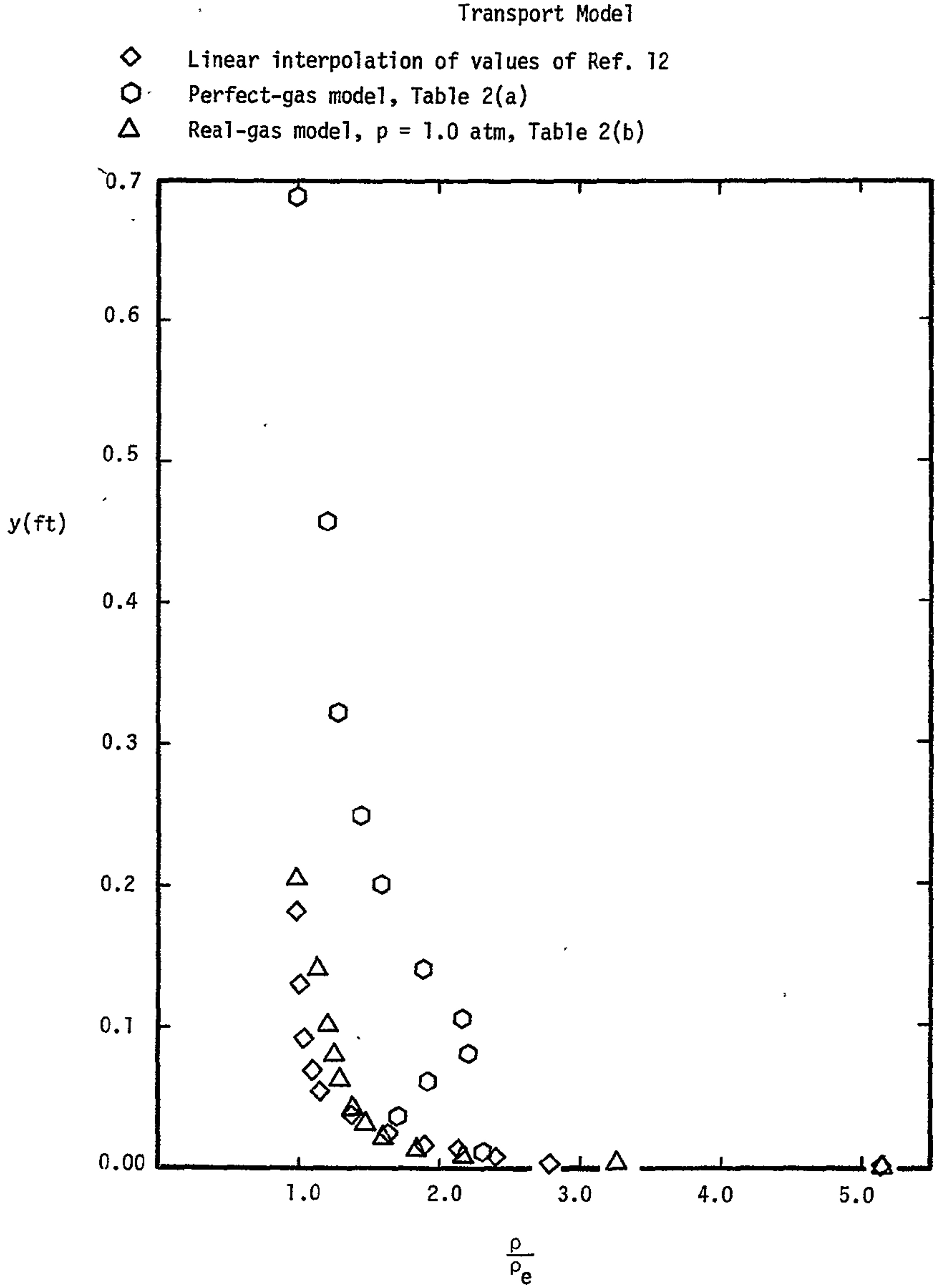

(b) x = 56.375 ft

Figure 8. - Concluded.

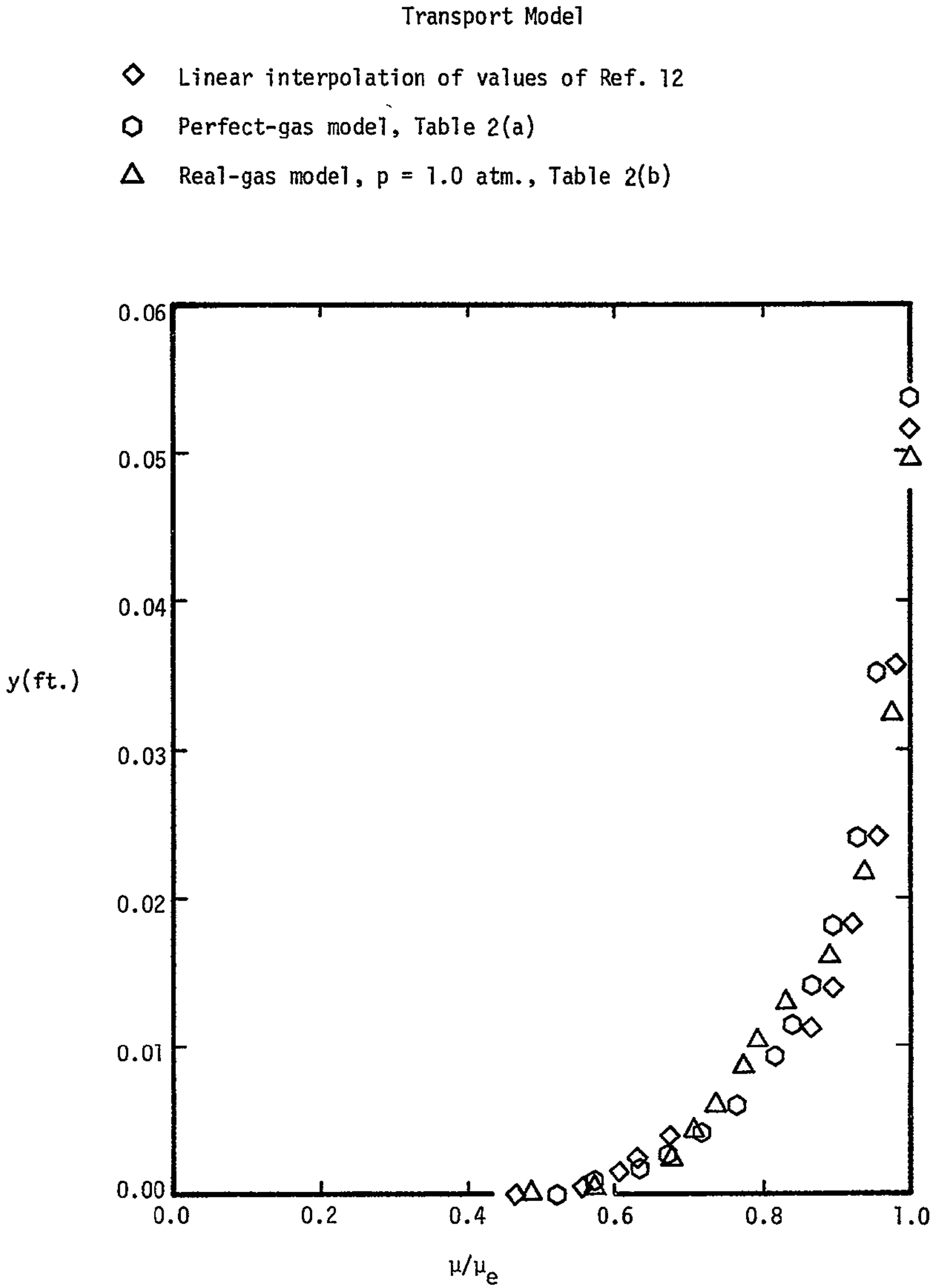

(a) x = 2.596 ft.

Figure 9. - The effect of the transport property model on the viscosity profile, $M_\infty = 22.04$

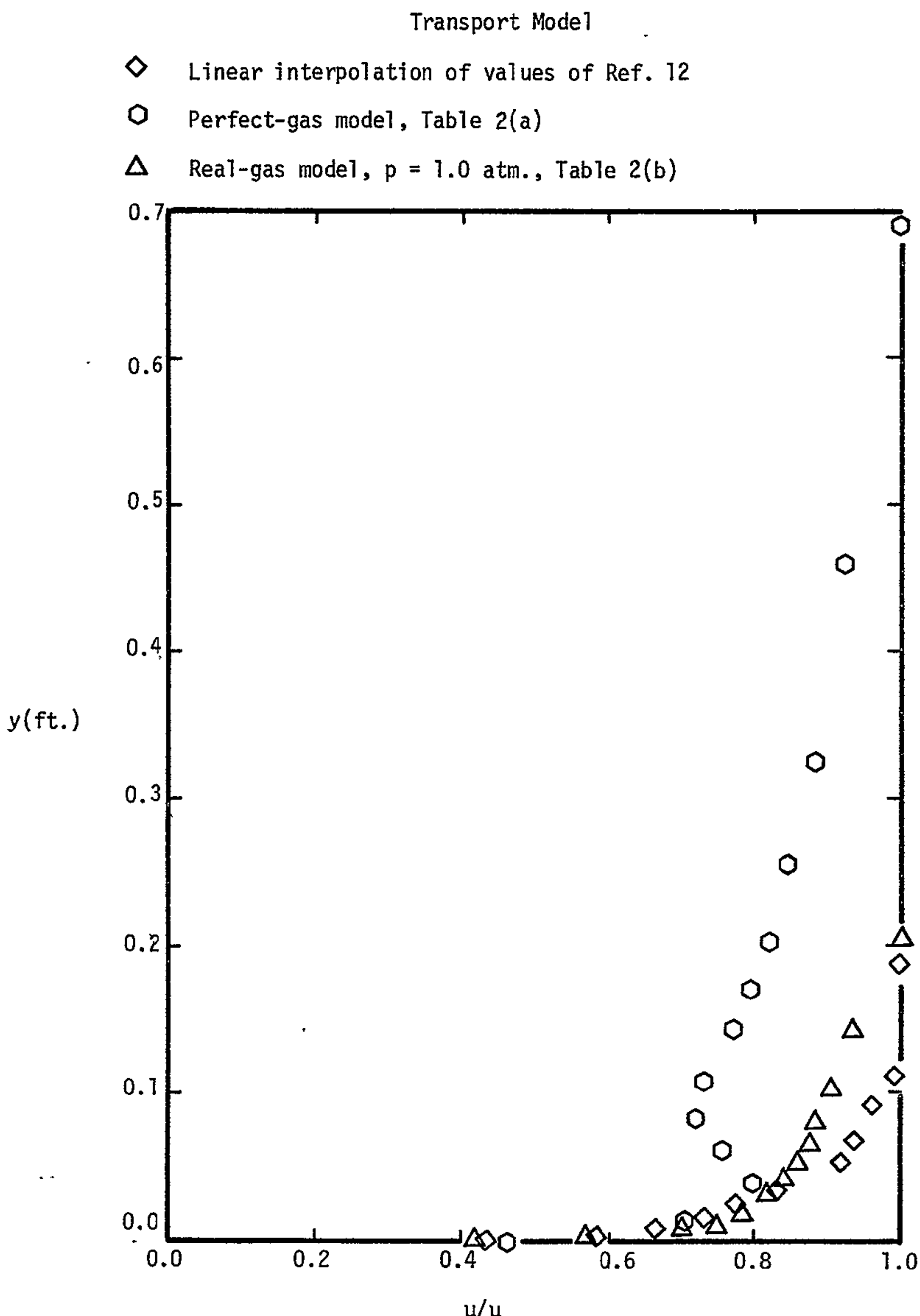

(b) x = 56.375 ft

Figure 9. - Concluded.

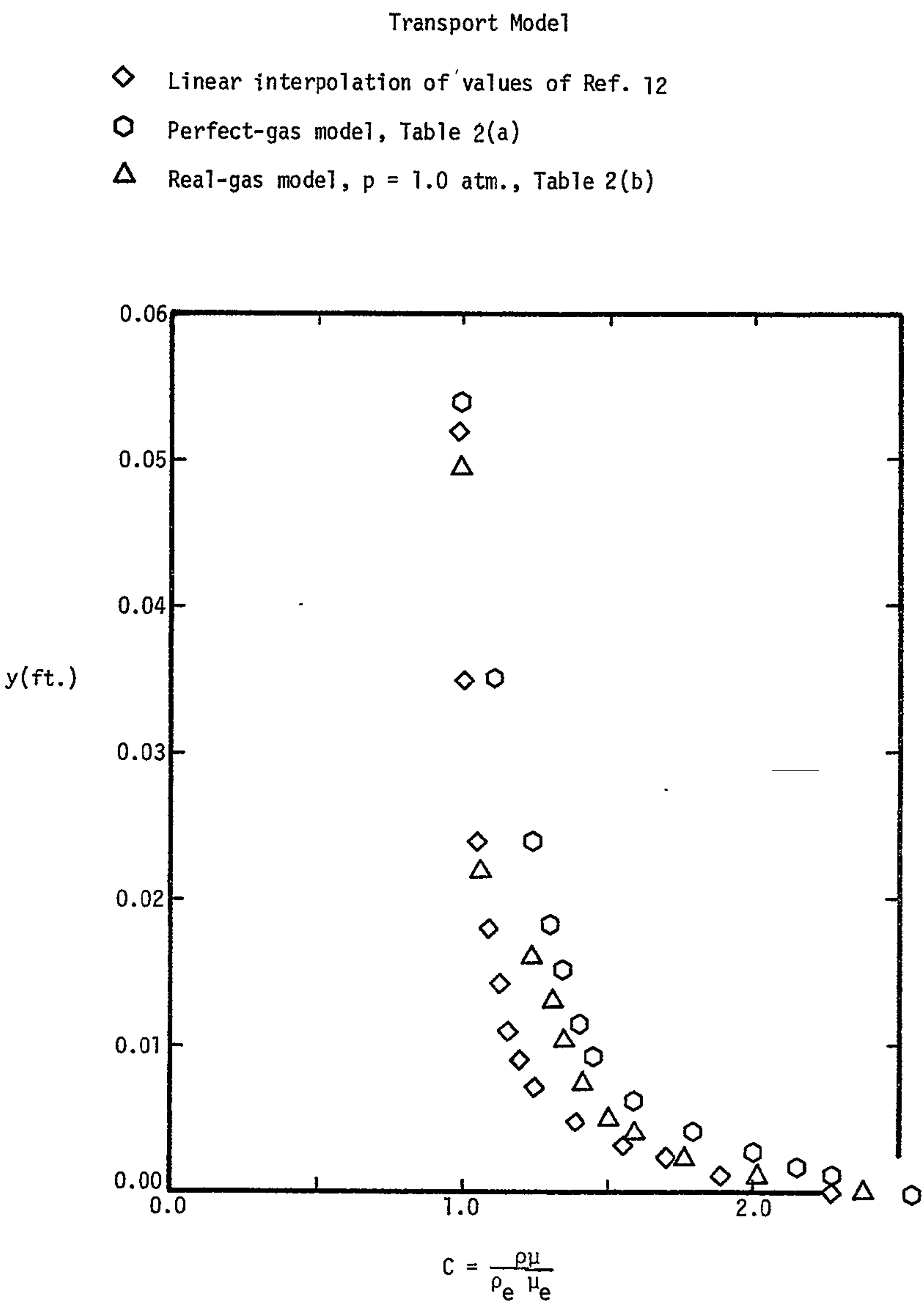

(a) x = 2.596 ft

Figure 10. - The effect of the transport property model on the Chapman-Rubesin factor profile, $M_\infty = 22.04$

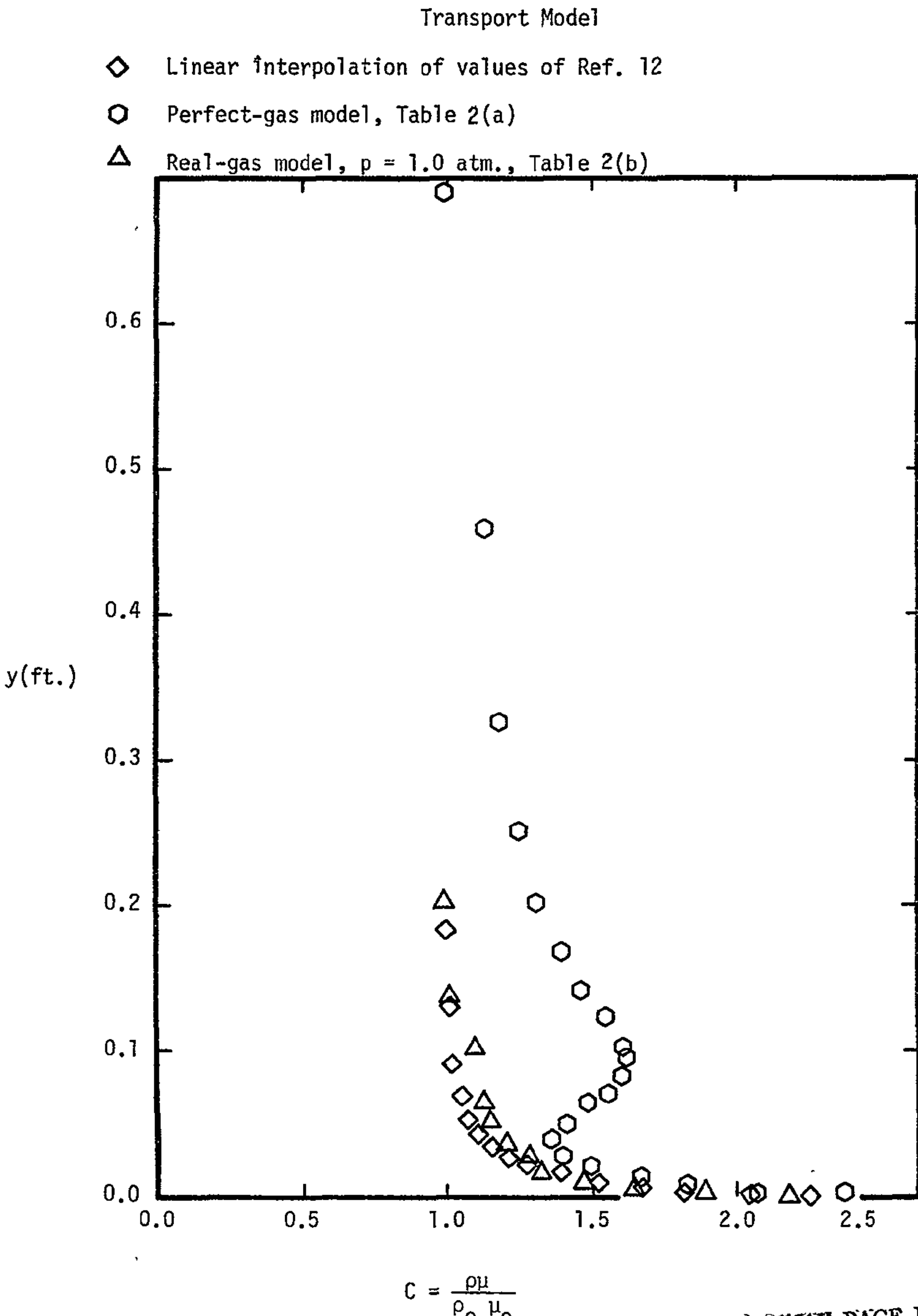

(b) x = 56.375

Figure 10. - Concluded.

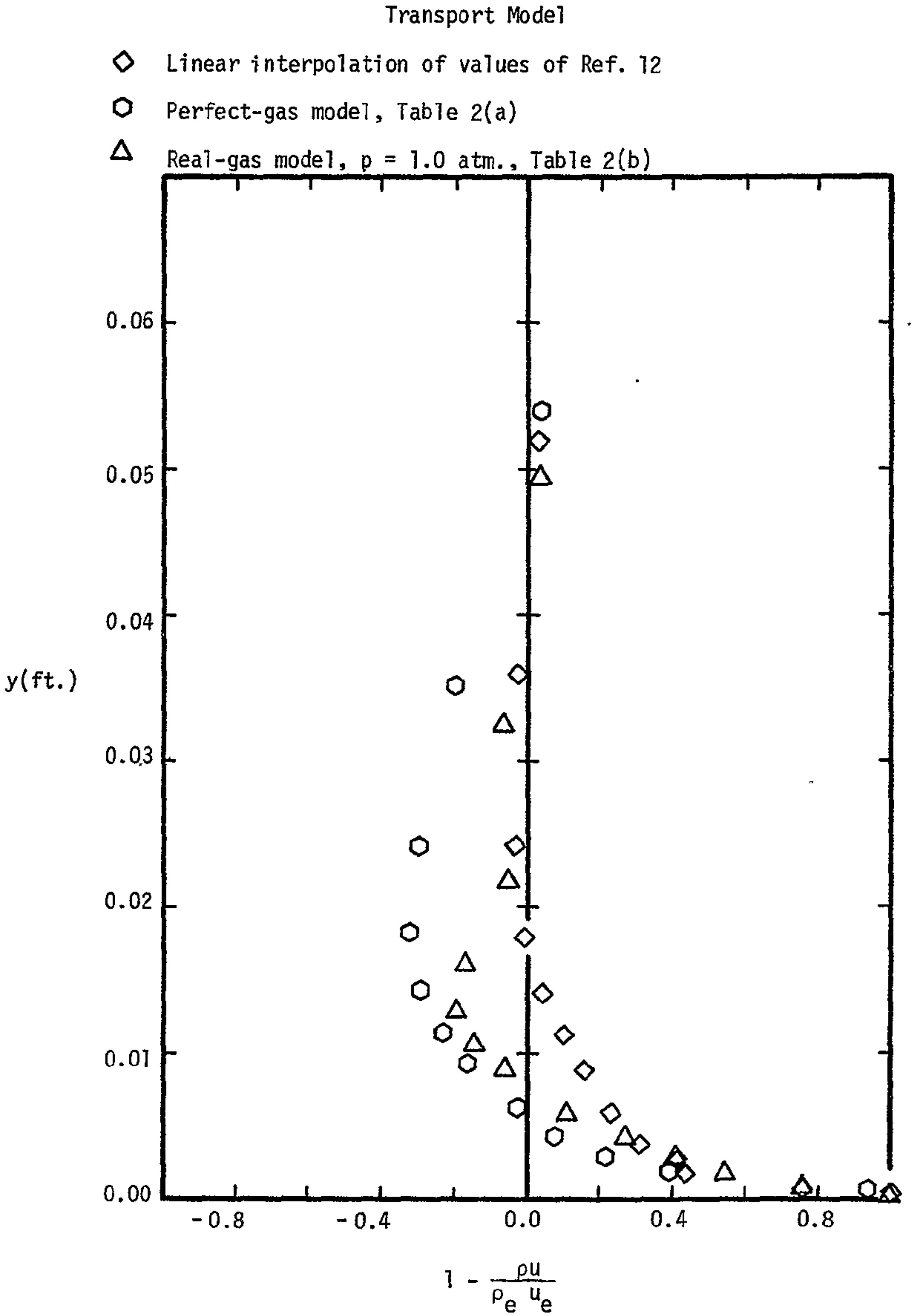

(a) x = 2.596 ft.

Figure 11. - The effect of the transport-property model on the profile of $(1 - \rho u/\rho_e u_e)$, $M_\infty = 22.04$.

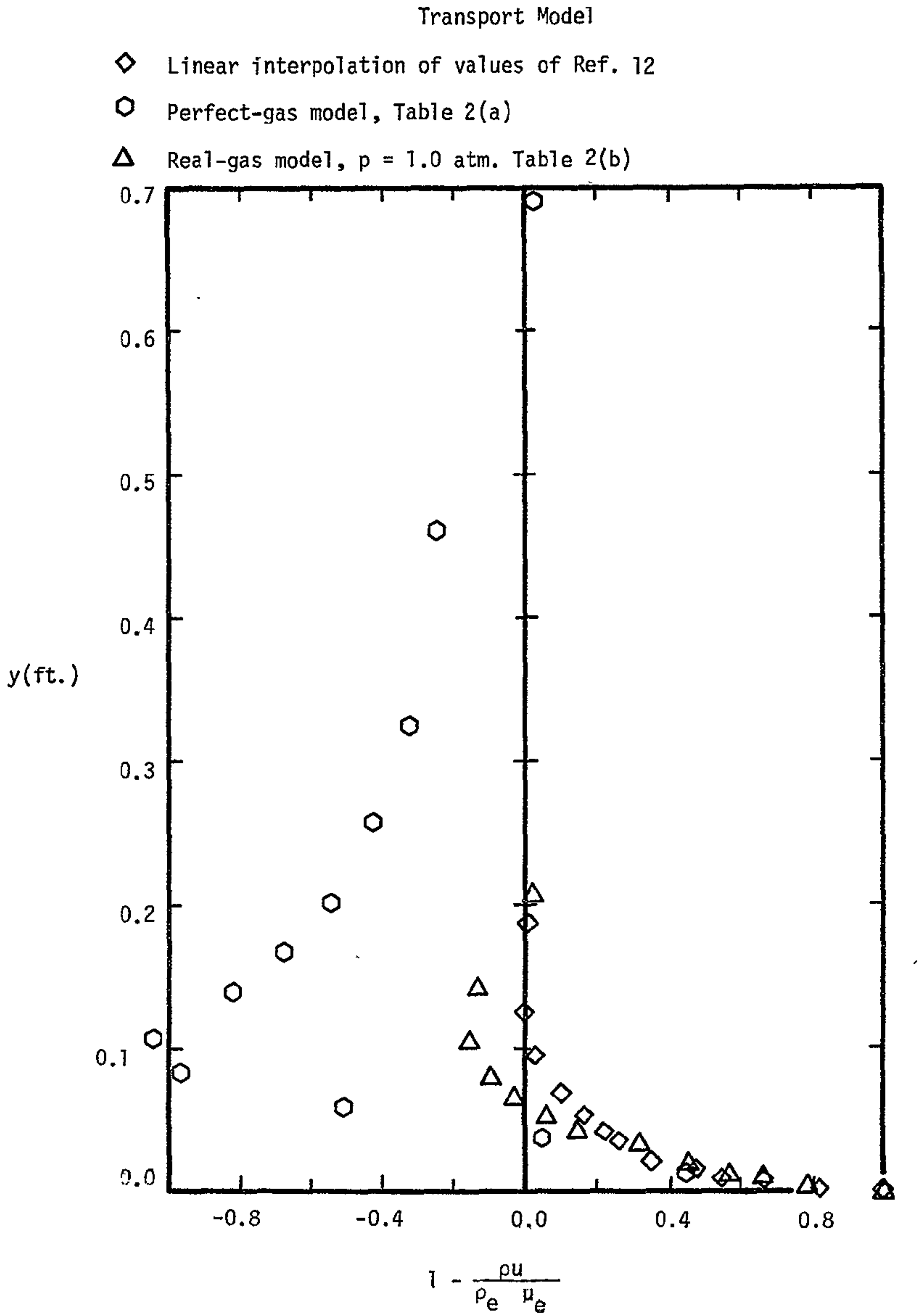

(b) x = 56.375 ft.

Figure 11. - Concluded.

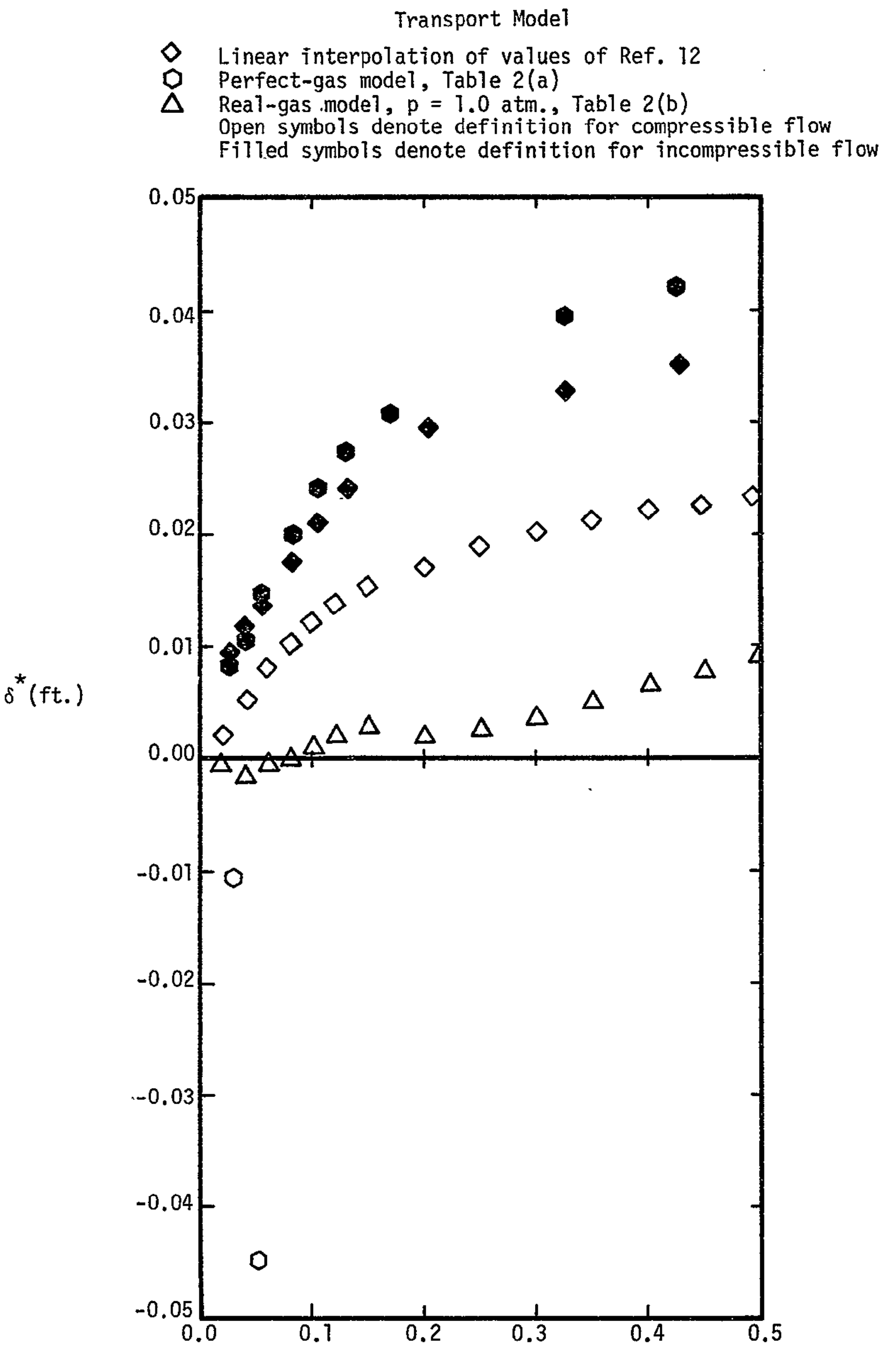

Figure 12. - The effect of the transport-property model on the streamwise distribution of the displacement thickness $M_\infty = 22.04$.

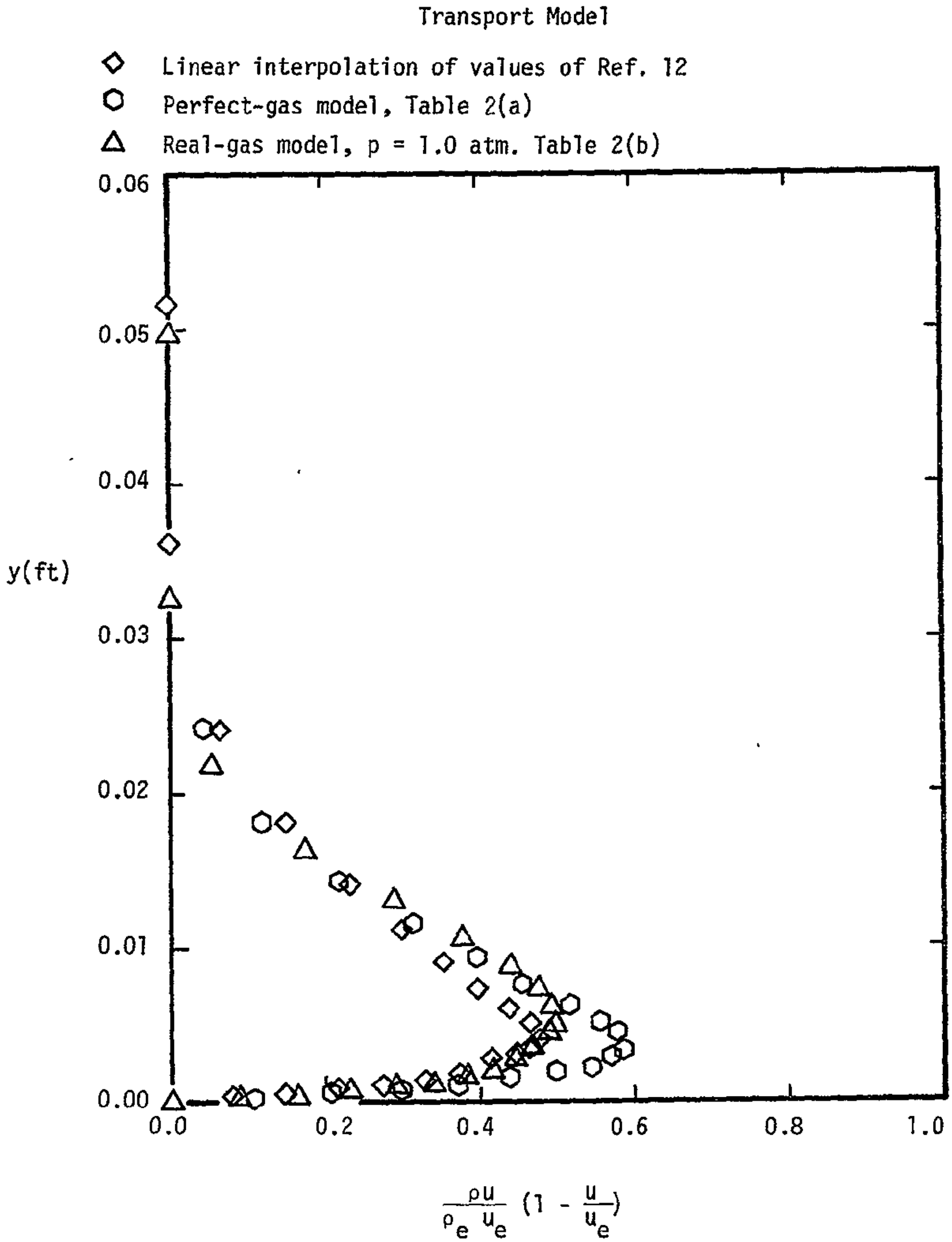

(a) x = 2.596 ft.

Figure 13. - The effect of the transport property model on the profile of $\frac{\rho u}{\rho_e u_e}(1 - \frac{u}{u_e})$, M_∞ = 22.04.

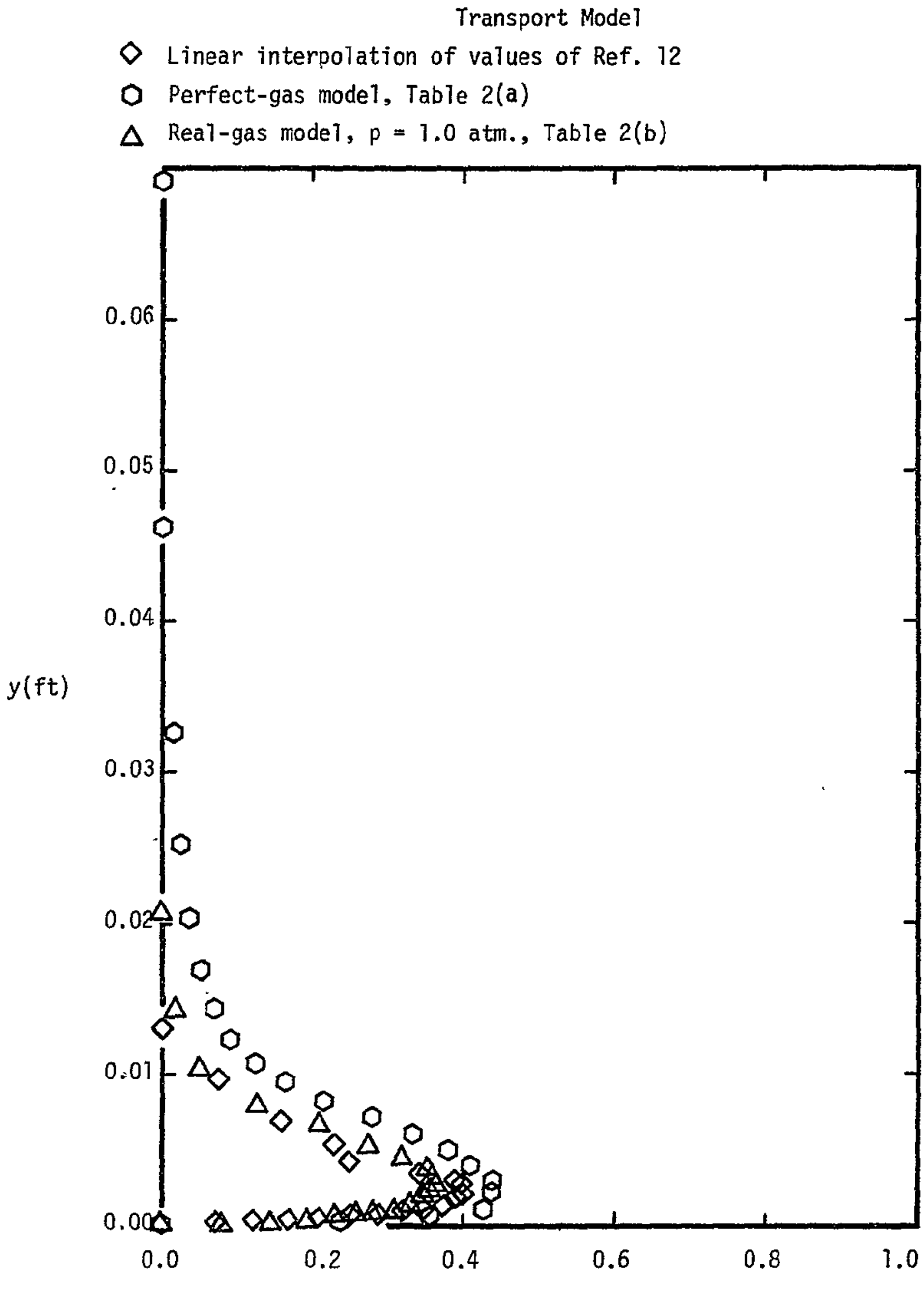

$$\frac{\rho}{\rho_e}\frac{u}{u_e}\left(1 - \frac{u}{u_e}\right)$$

(b) x = 56.375 ft.

Figure 13. - Concluded.

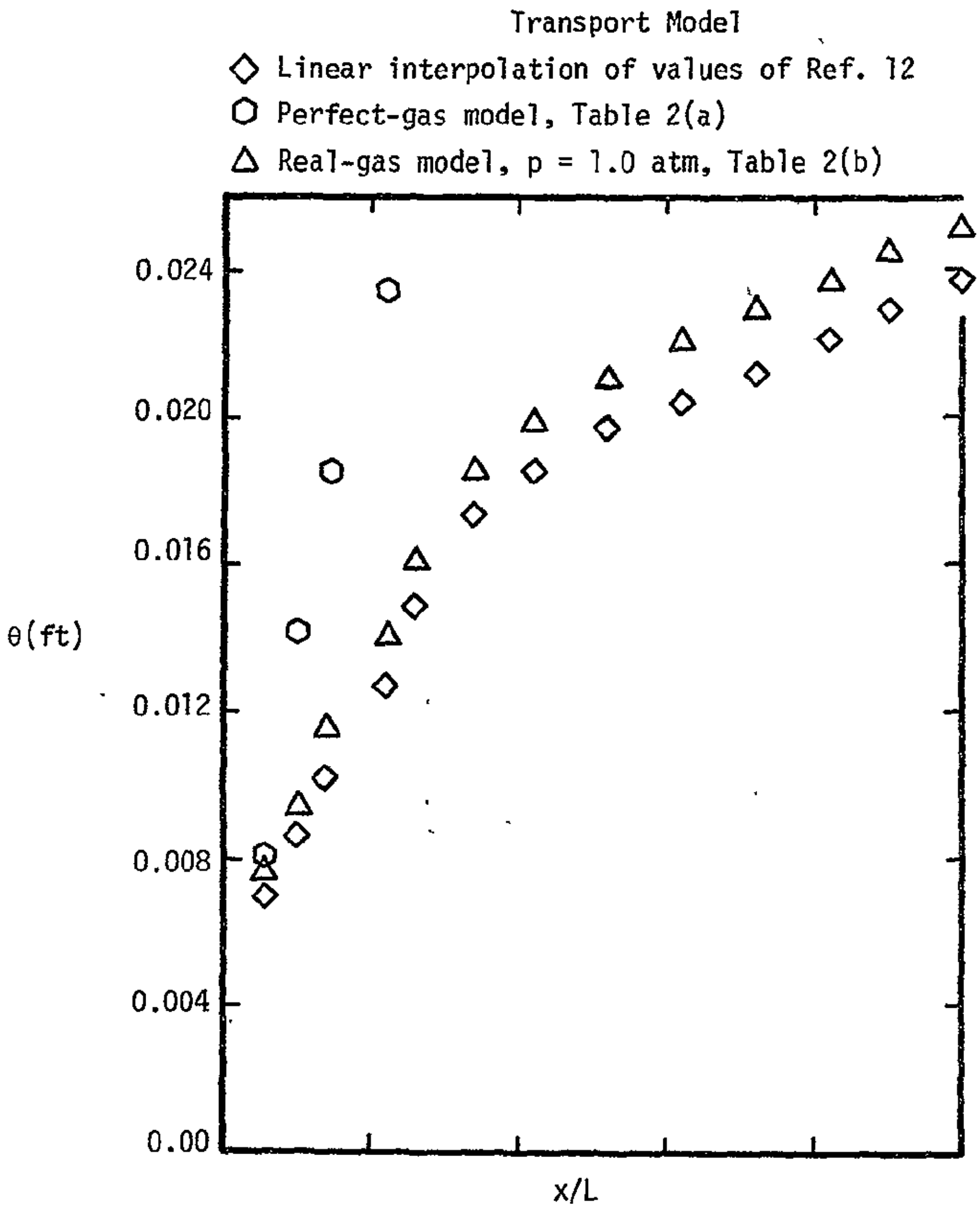

Figure 14. - The effect of the transport property model on the streamwise distribution of the momentum thickness, $M_\infty = 22.04$.

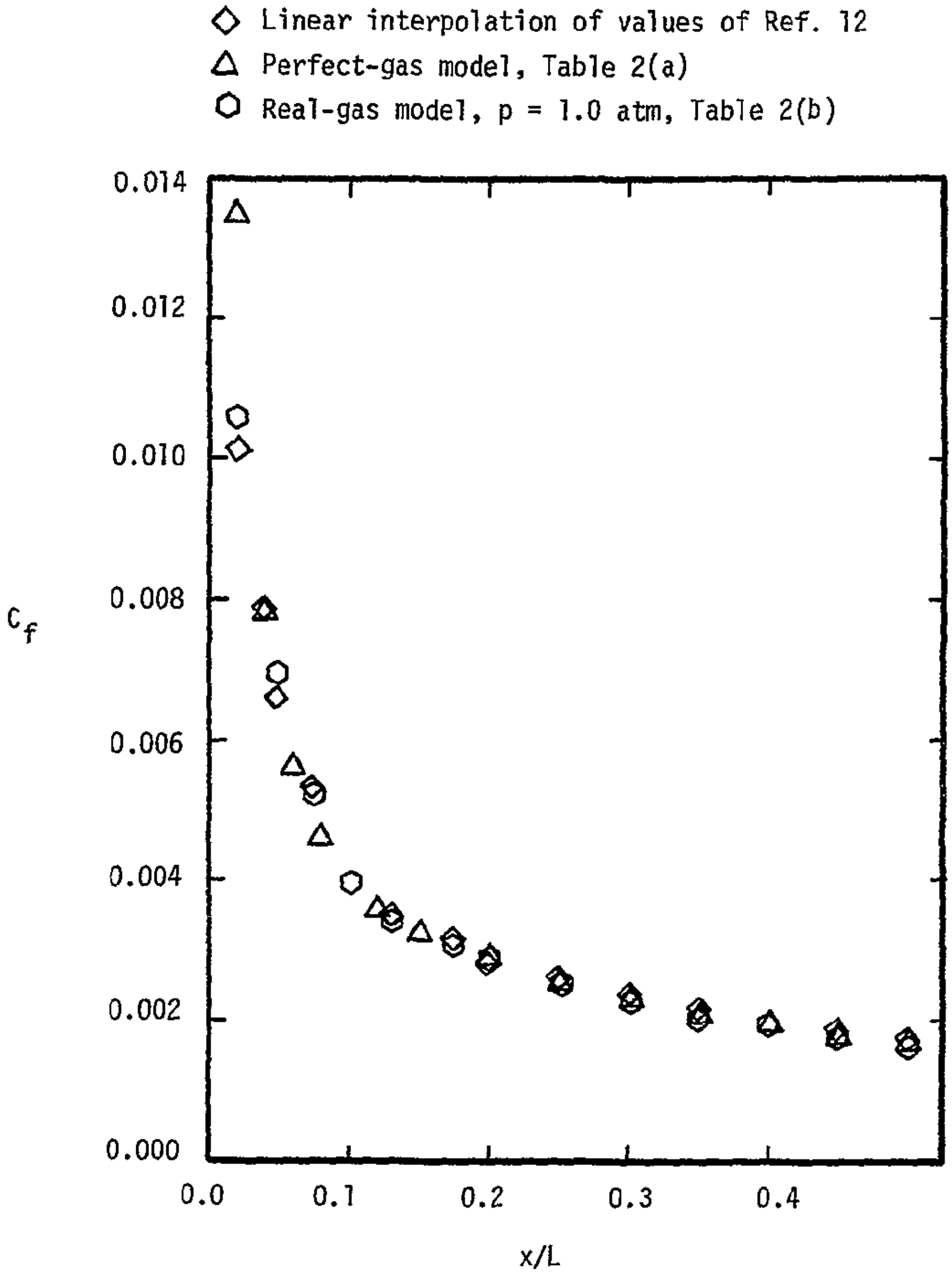

Figure 15. - The effect of transport property model on the skin friction coefficient distribution, $M_\infty = 22.04$

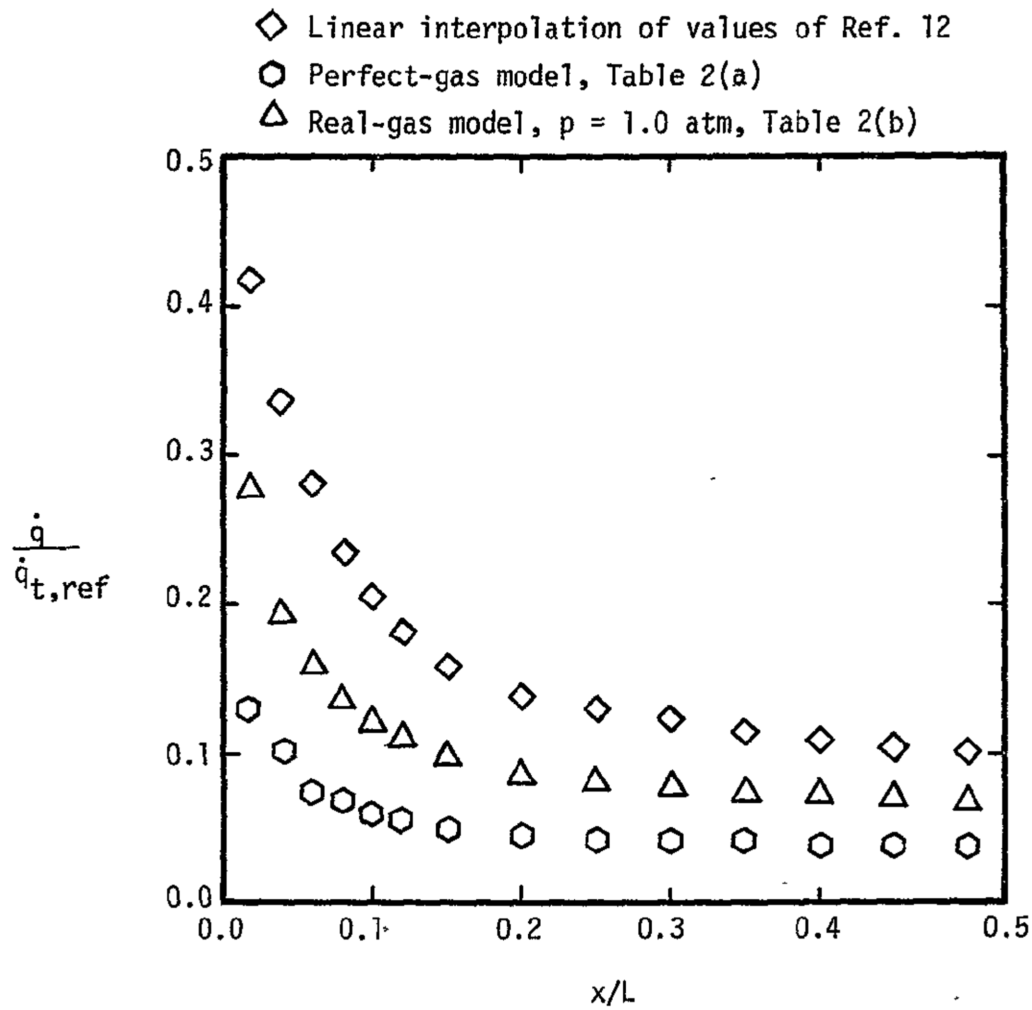

Figure 16. - The effect of transport property model on the convective heat transfer rate distribution, $M_\infty = 22.04$.

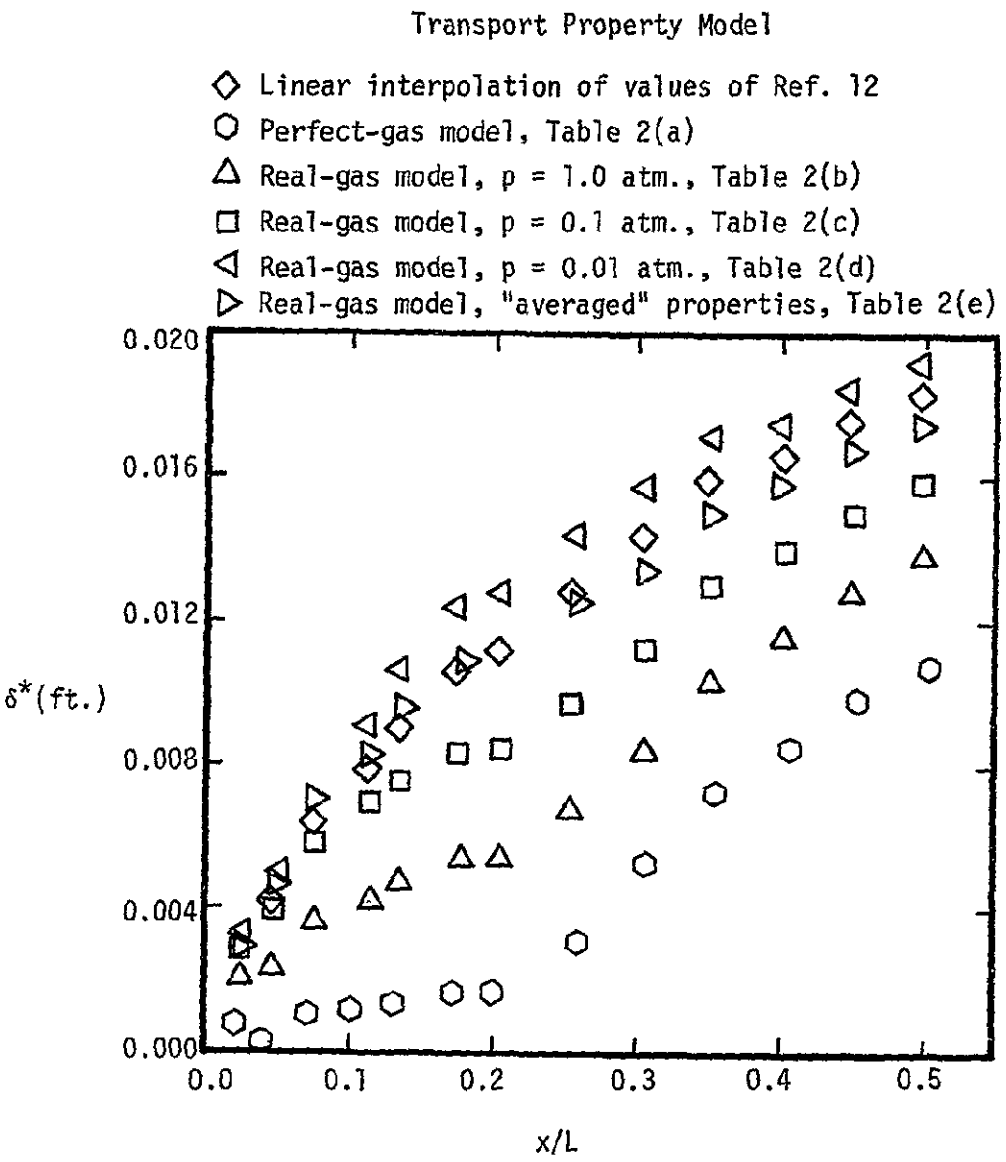

(a) The displacement thickness, δ^*

Figure 17.- The aerothermo distributions as calculated for the six transport property models for flow condition (a), $M_\infty = 9.49$

Transport Property Model

◇ Linear Interpolation of values of Ref. 12

⬡ Perfect-gas model, Table 2(a)

△ Real-gas model, p = 1.0 atm., Table 2(b)

□ Real-gas model, p = 0.1 atm., Table 2(c)

◁ Real-gas model, p = 0.01 atm., Table 2(d)

▷ Real-gas model, "averaged" properties, Table 2(e)

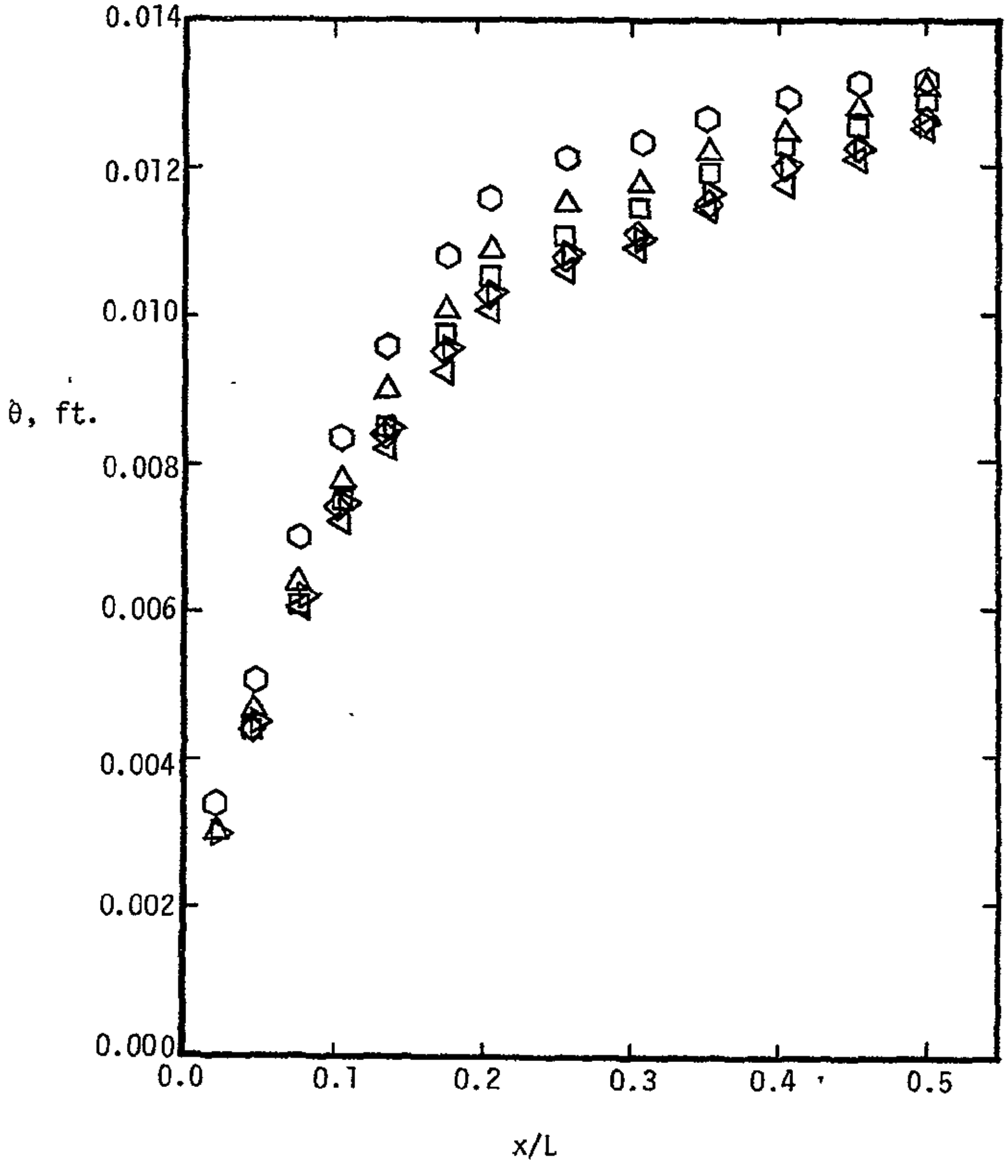

(b) The momentum thickness, θ

Figure 17. - Continued

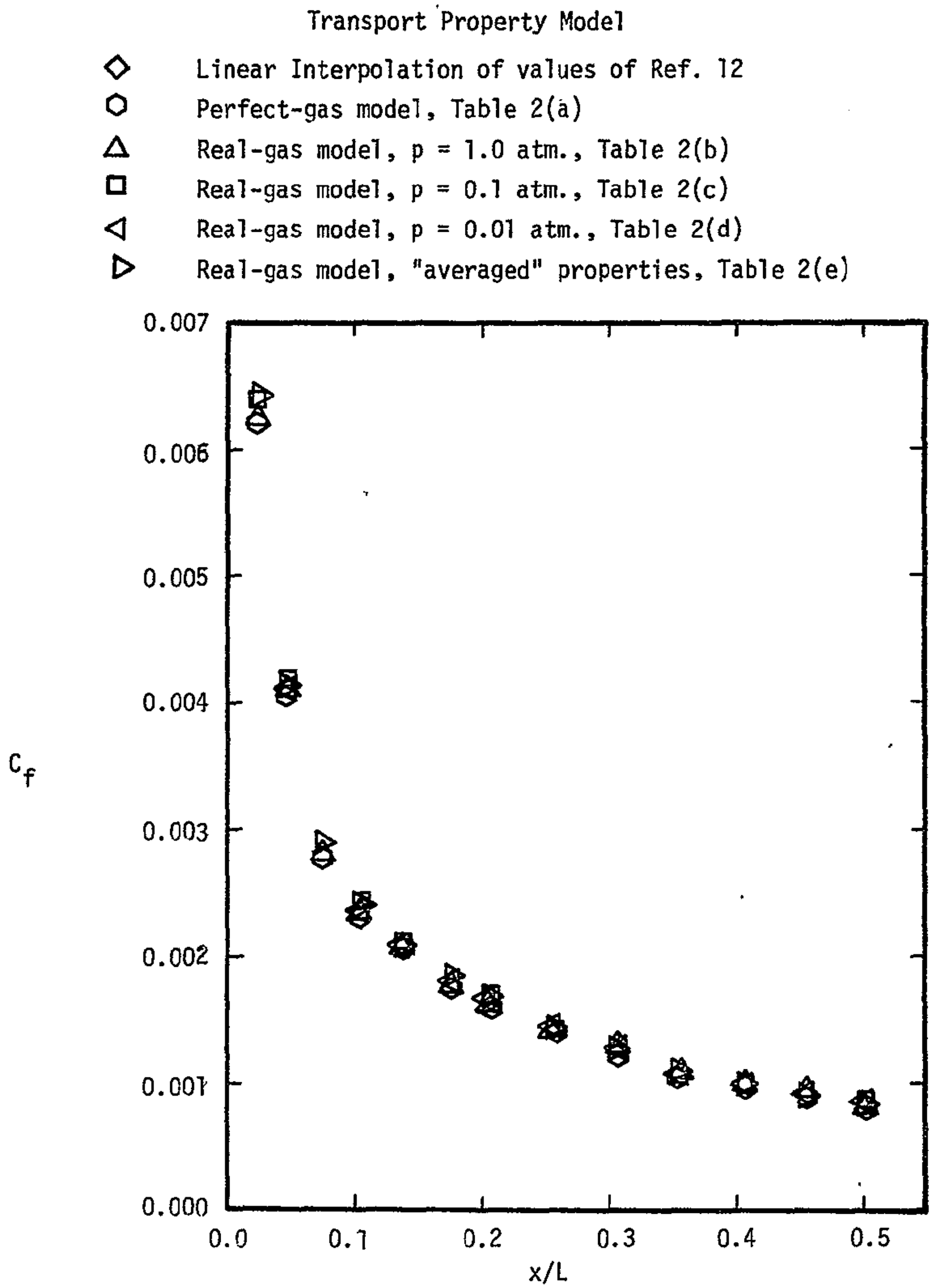

(c) The skin-friction coefficient

Figure 17. - Continued

Transport Property Model

◇ Linear Interpolation of values of Ref. 12
○ Perfect-gas model, Table 2(a)
△ Real-gas model, p = 1.0 atm., Table 2(b)
□ Real-gas model, p = 0.1 atm., Table 2(c)
◁ Real-gas model, p = 0.01 atm., Table 2(d)
▷ Real-gas model, "averaged" properties, Table 2(e)

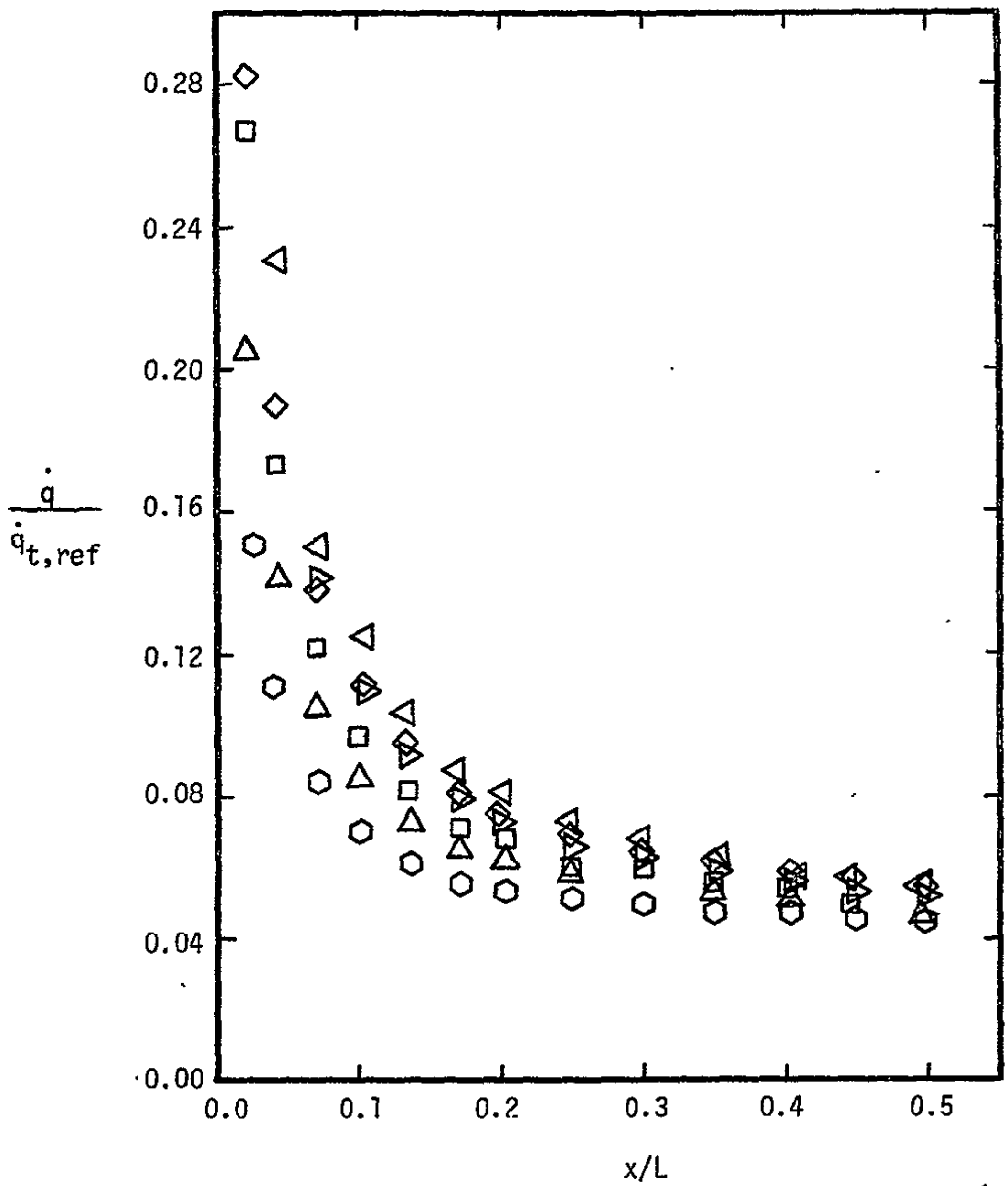

(d) The heat-transfer rate

Figure 17. - Concluded

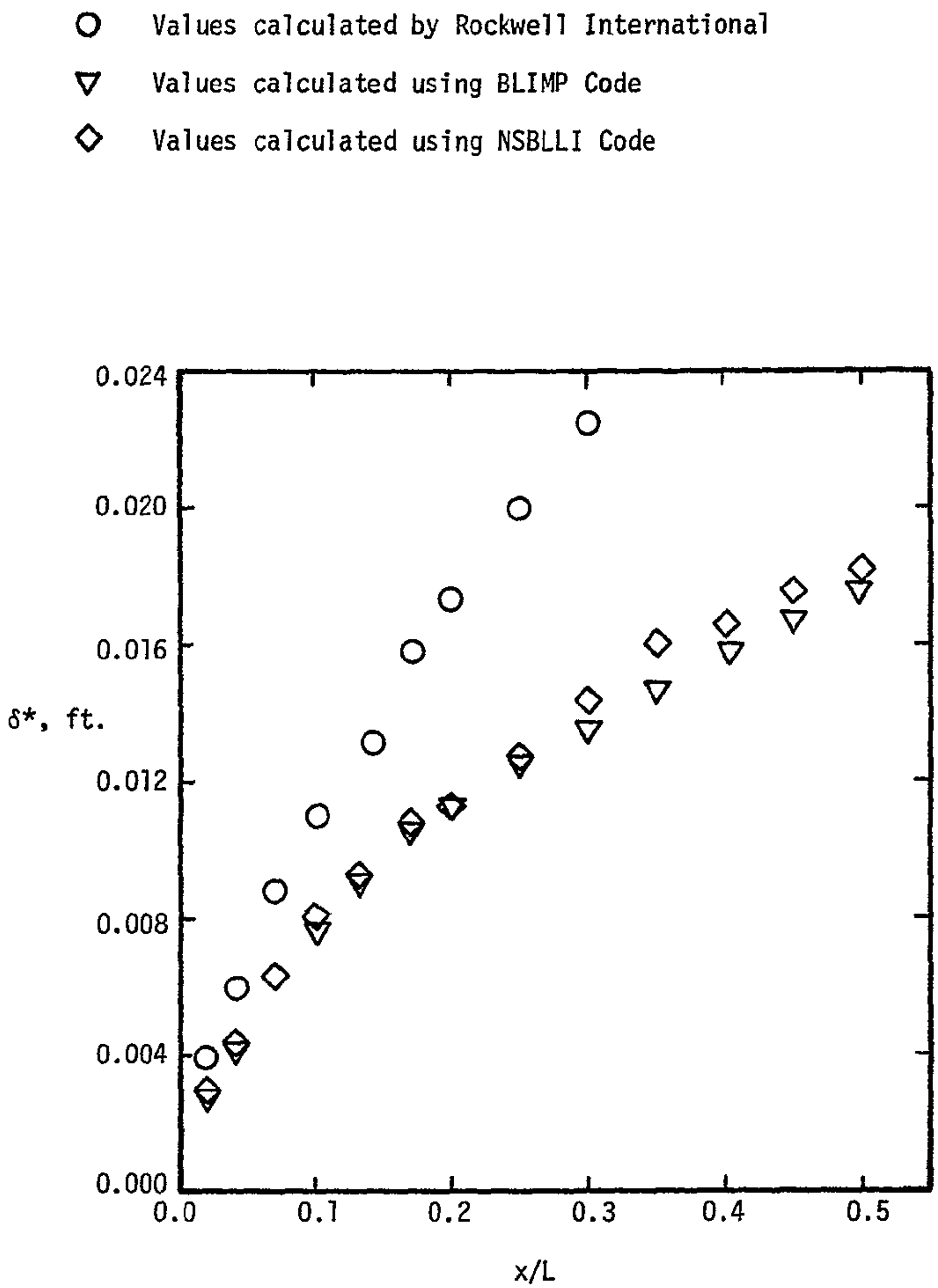

(a) The displacement thickness, δ*

Figure 18. - The "real-gas" aerothermo distributions as calculated by three groups for flow condition (a), $M_\infty = 9.49$

○ Values calculated by Rockwell International

▽ Values calculated using BLIMP Code

◇ Values calculated using NSBLLI Code

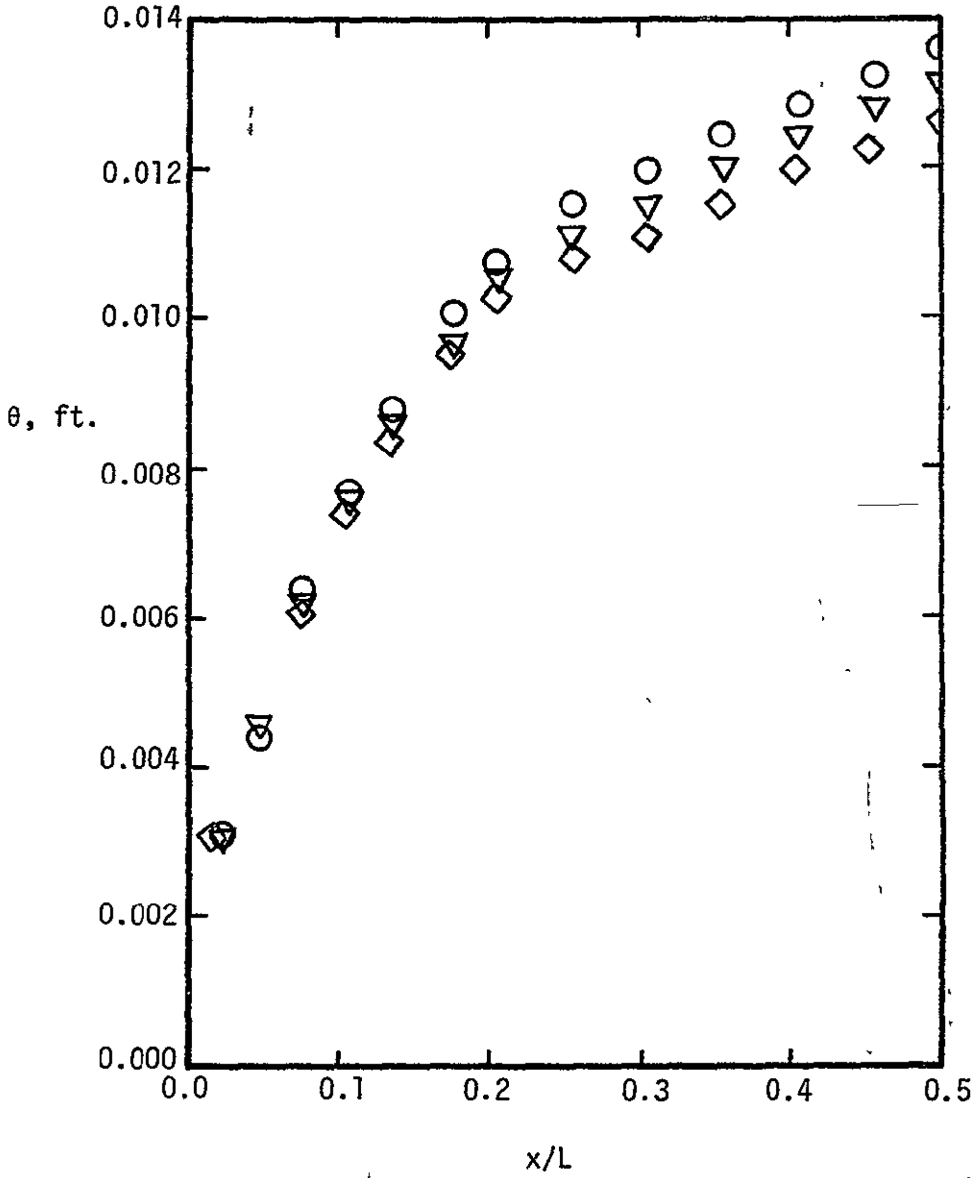

(b) The momentum thickness, θ

Figure 18. - Continued

○ Values calculated by Rockwell International

▽ Values calculated using BLIMP Code

◇ Values calculated using NSBLLI Code

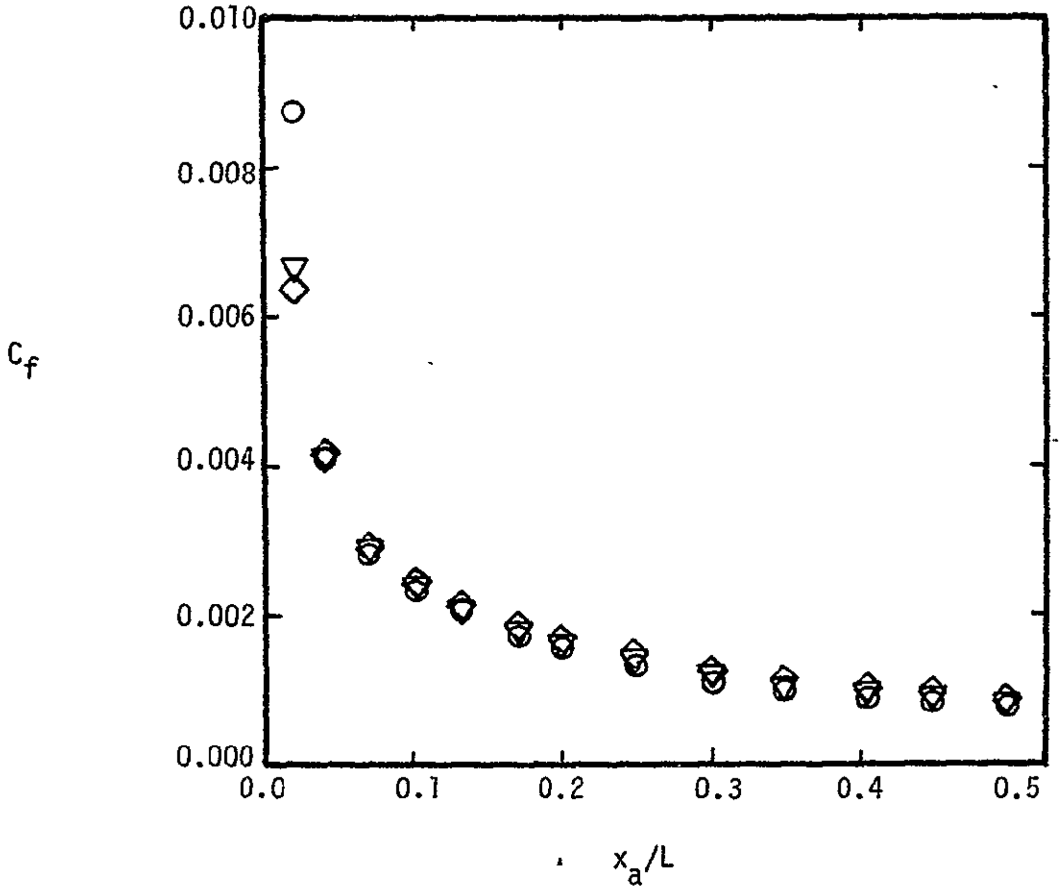

(c) The skin-friction coefficient

Figure 18. - Continued

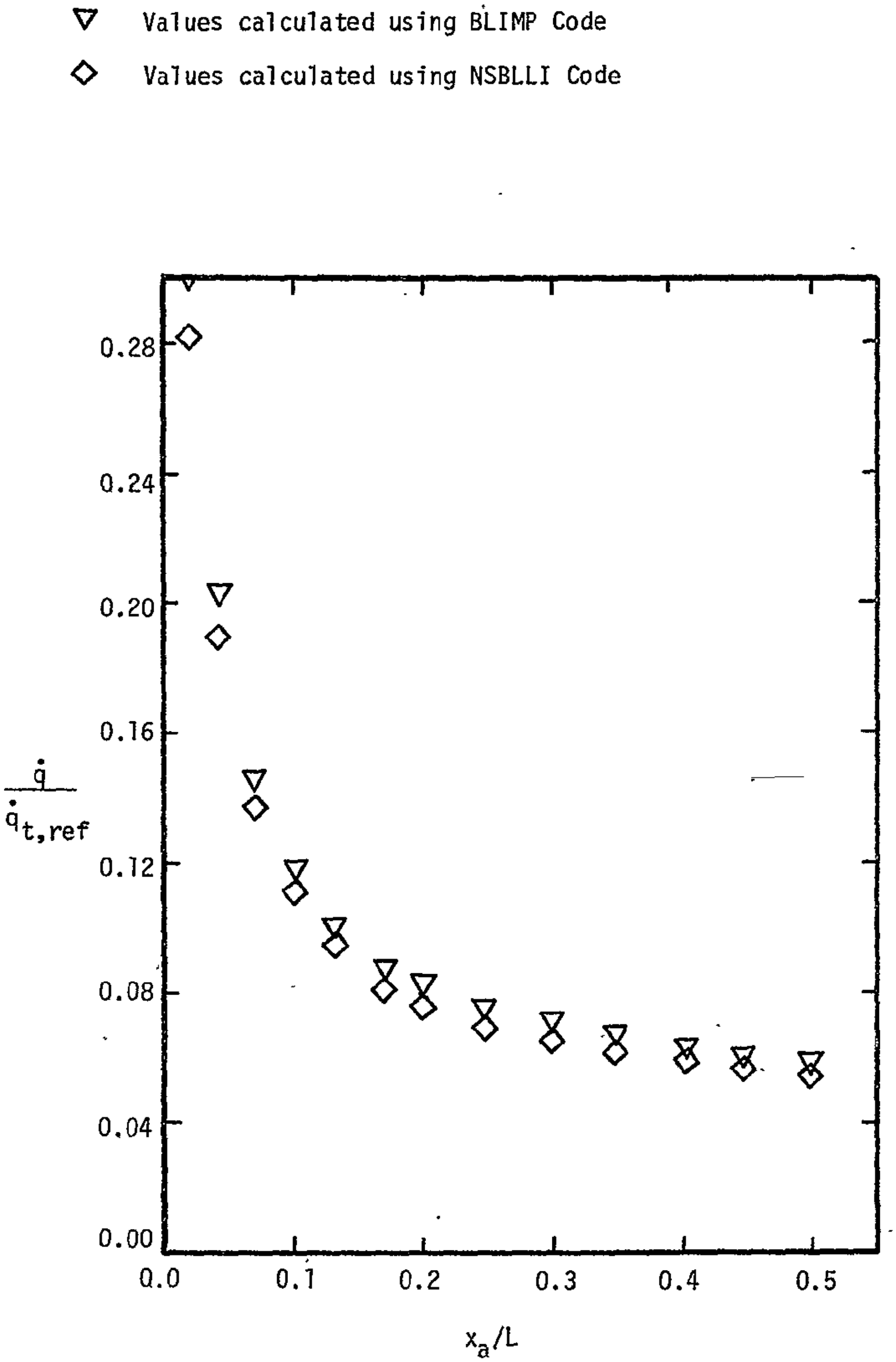

(d) The heat-transfer rates

Figure 18. - Concluded.

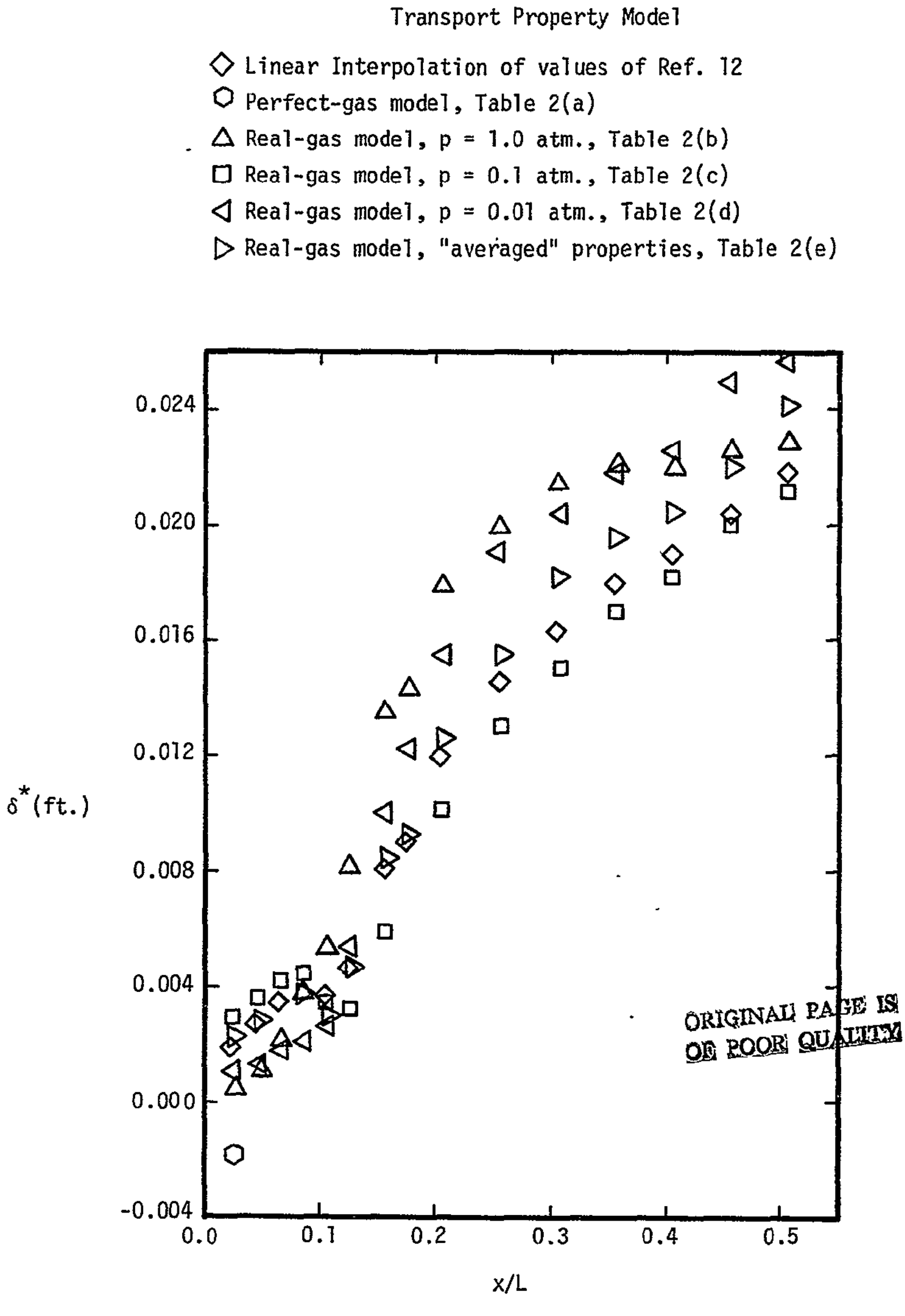

(a) The displacement thickness, δ^*

Figure 19. - The aerothermo distributions as calculated for the six transport property models for the flow condition (b), $M_\infty = 16.05$

Transport Property Módel

◇ Linear Interpolation of values of Ref. 12

○ Perfect-gas model, Table 2(a)

△ Real-gas model, p = 1.0 atm., Table 2(b)

□ Real-gas model, p = 0.1 atm., Table 2(c)

◁ Real-gas model, p = 0.01 atm., Table 2(d)

▷ Real-gas model, "averaged" properties, Table 2(e)

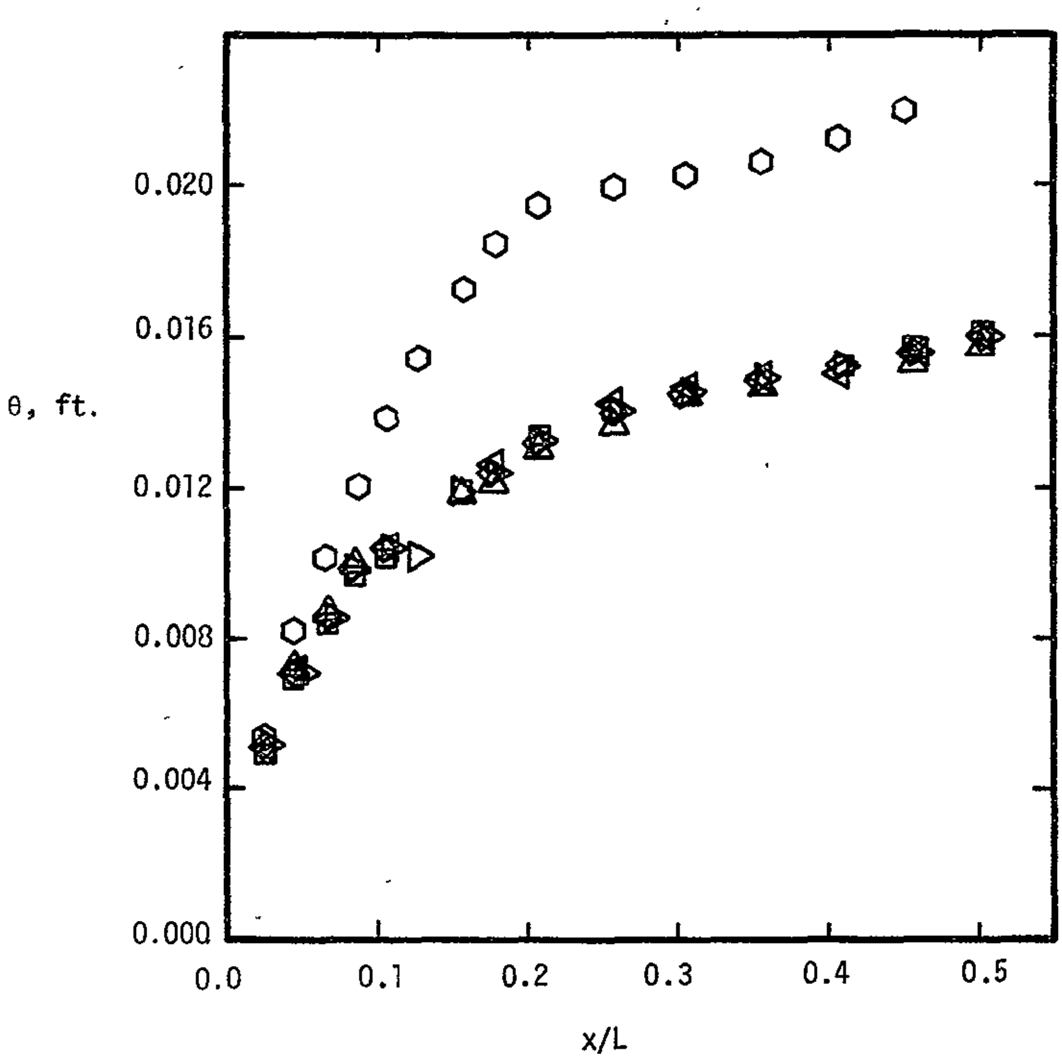

(b) The momentum thickness, θ.

Figure 19. - Continued

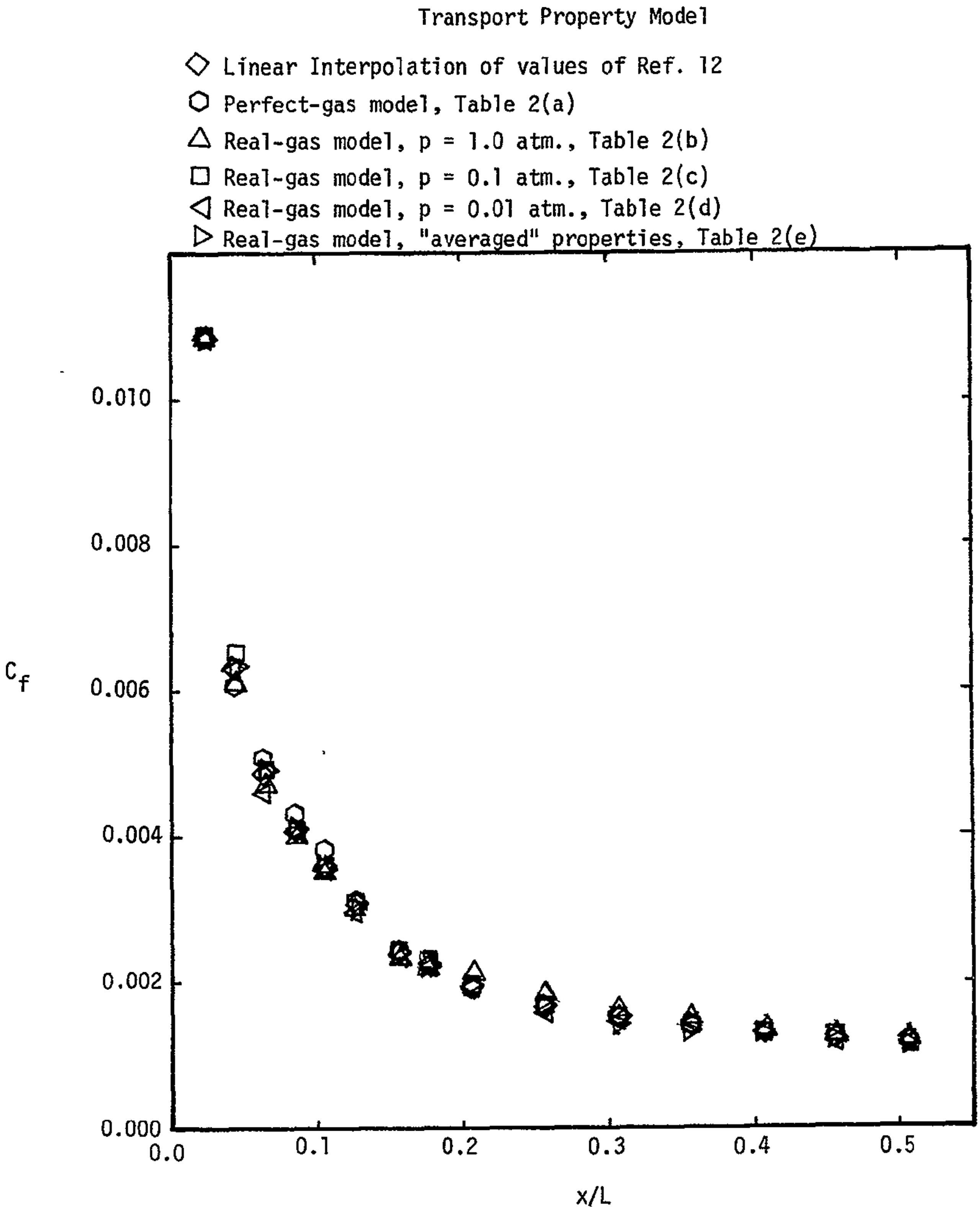

(c) The skin-friction coefficient

Figure 19. - Continued

Transport Property Model

◇ Linear interpolation of values of Ref. 12
⬡ Perfect-gas model, Table 2(a)
△ Real-gas model, p = 1.0 atm., Table 2(b)
□ Real-gas model, p = 0.1 atm., Table 2(c)
◁ Real-gas model, p = 0.01 atm., Table 2(d)
▷ Real-gas model, "averaged" properties, Table 2(e)

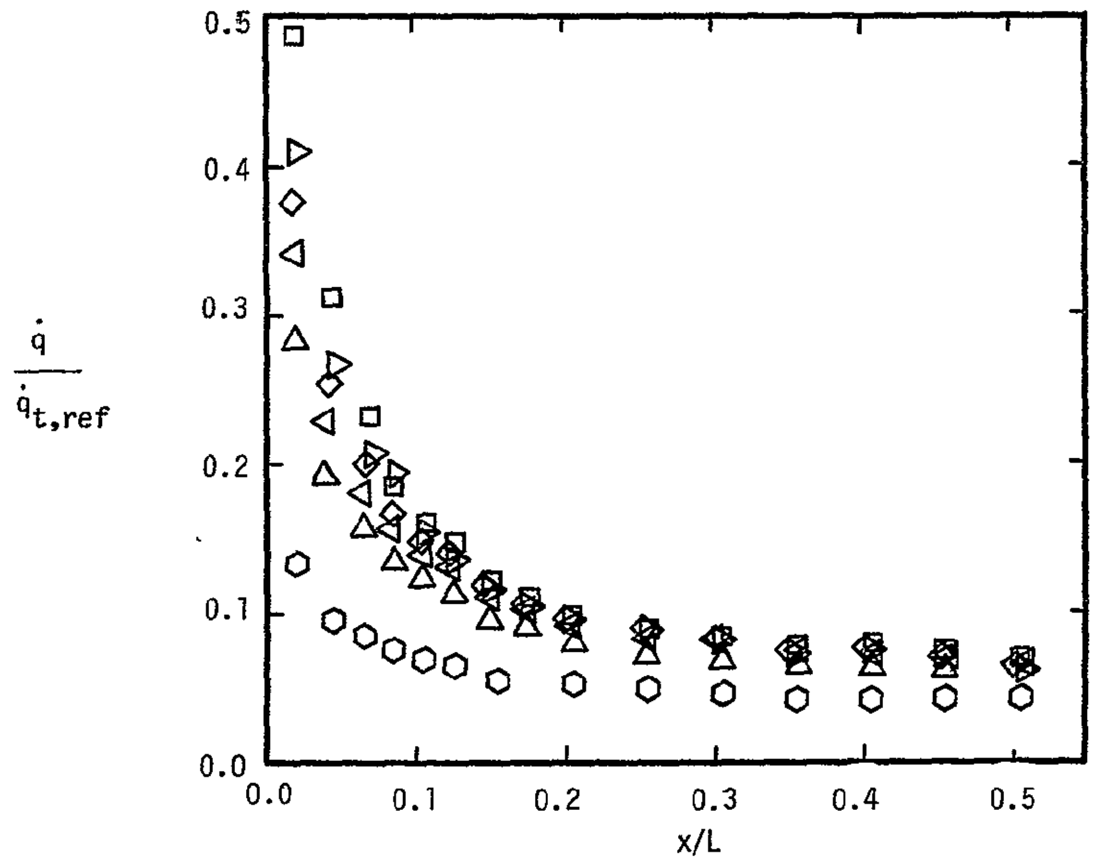

(d) The heat-transfer rate, $\dot{q}/\dot{q}_{t,ref}$

Figure 19. - Concluded

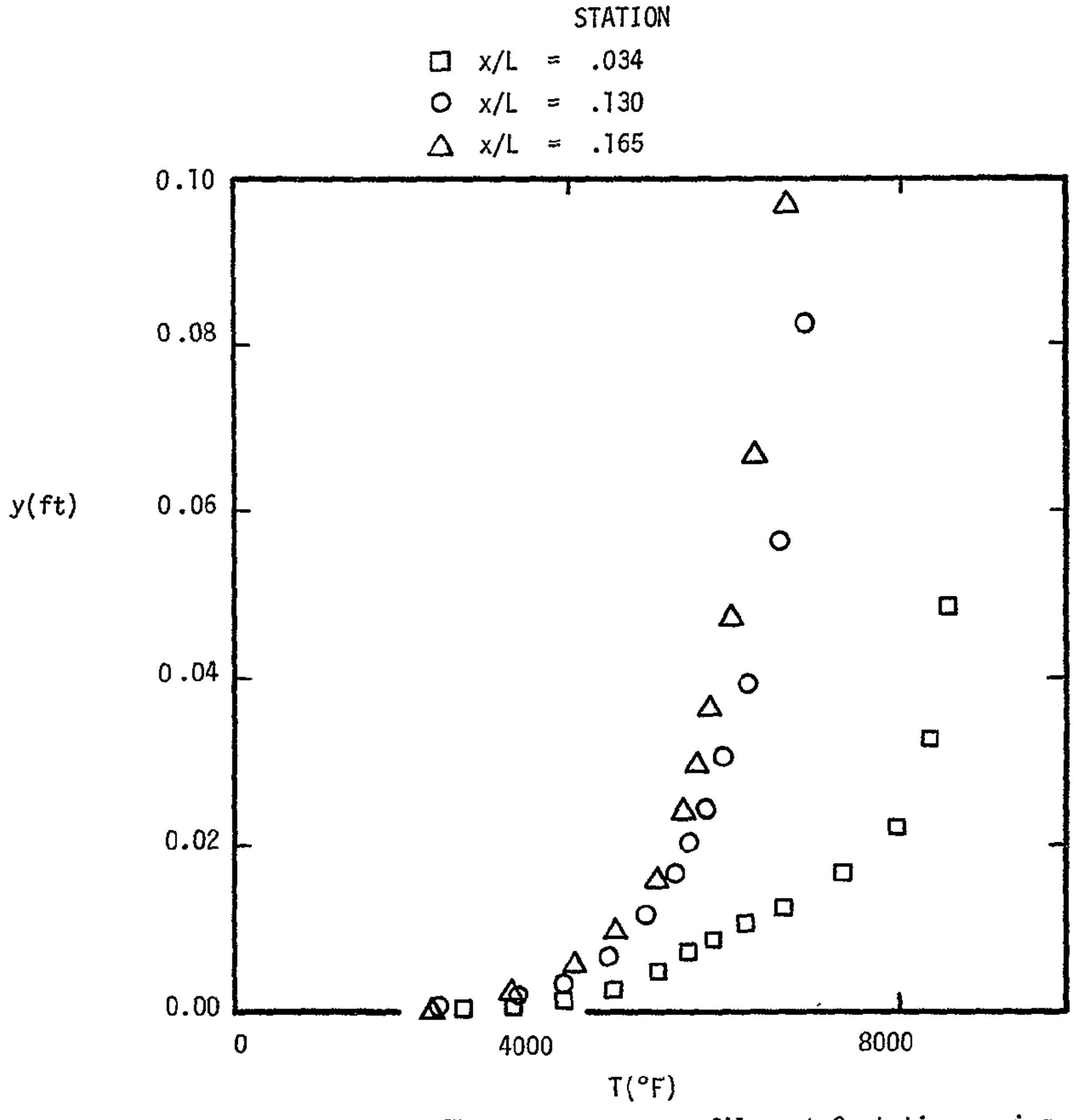

Figure 20. - The temperature profiles at 3 stations using the linear interpolation model for the flow condition (b), $M_\infty = 16.05$.

○ Values calculated by Rockwell International

▽ Values calculated using BLIMP Code

◇ Values calculated using NSBLLI Code

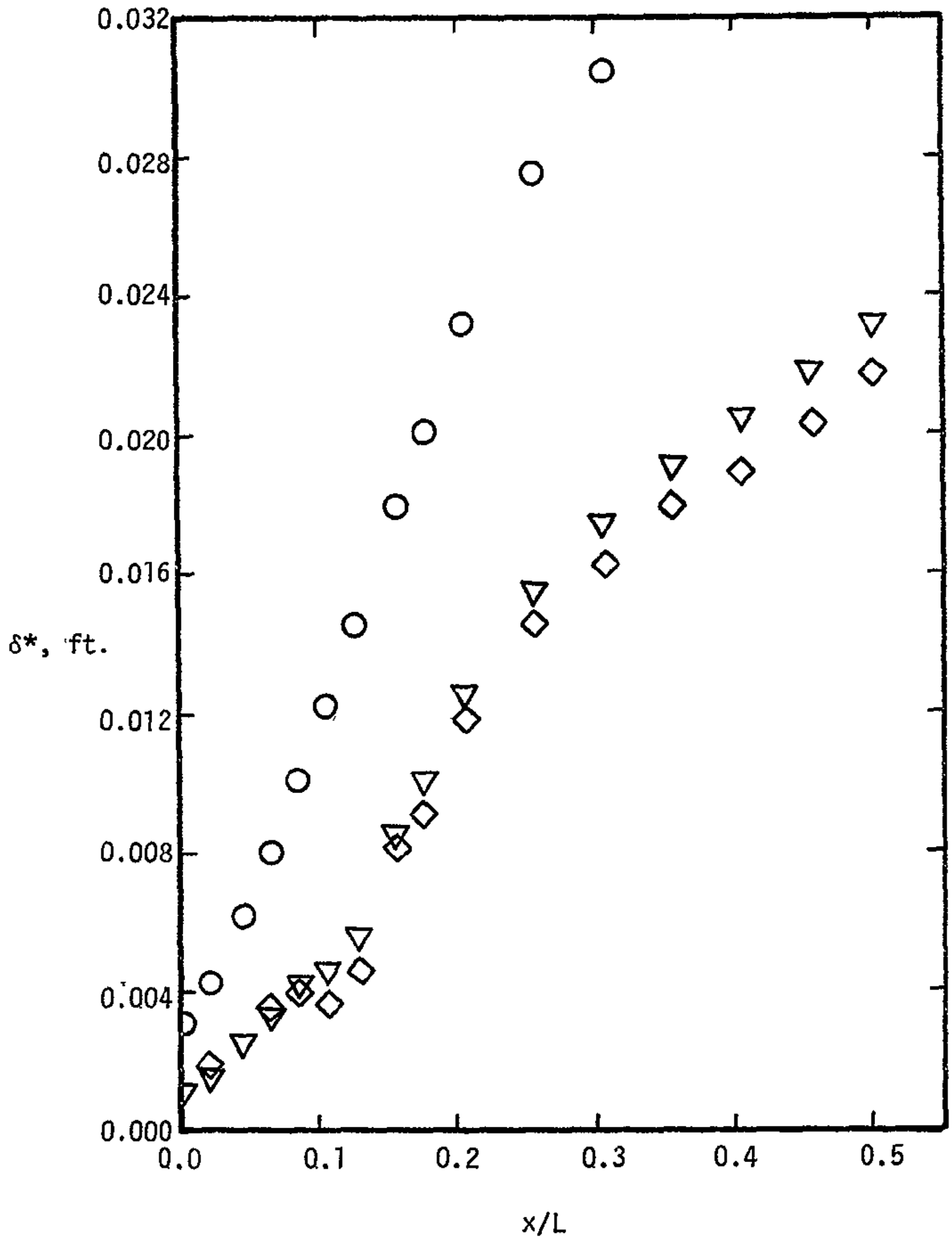

(a) The displacement thickness, δ^*

Figure 21. The "real-gas" aerothermo distributions as calculated by three groups for flow condition (b), $M_\infty = 16.05$.

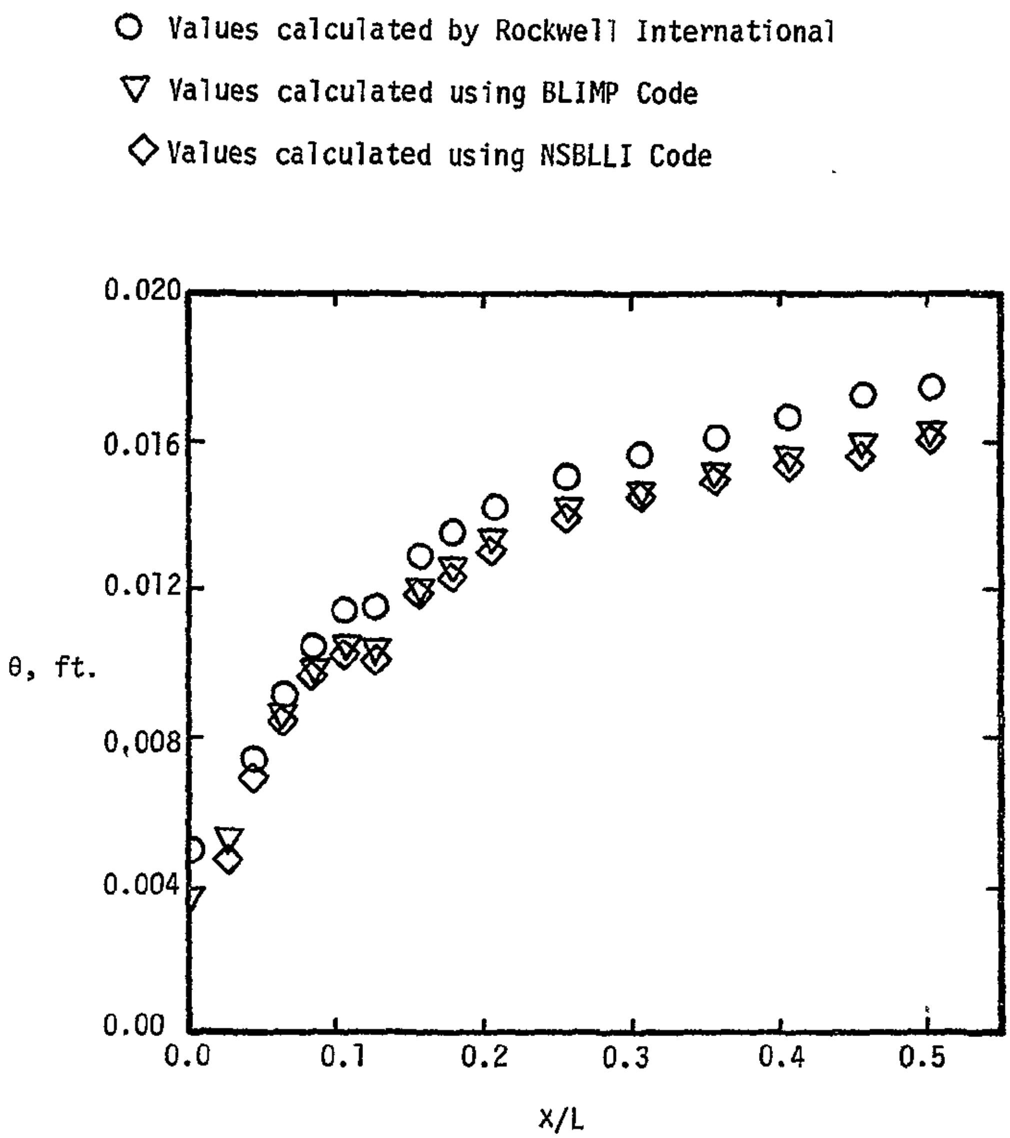

(b) The momentum thickness, θ

Figure 21. - Continued

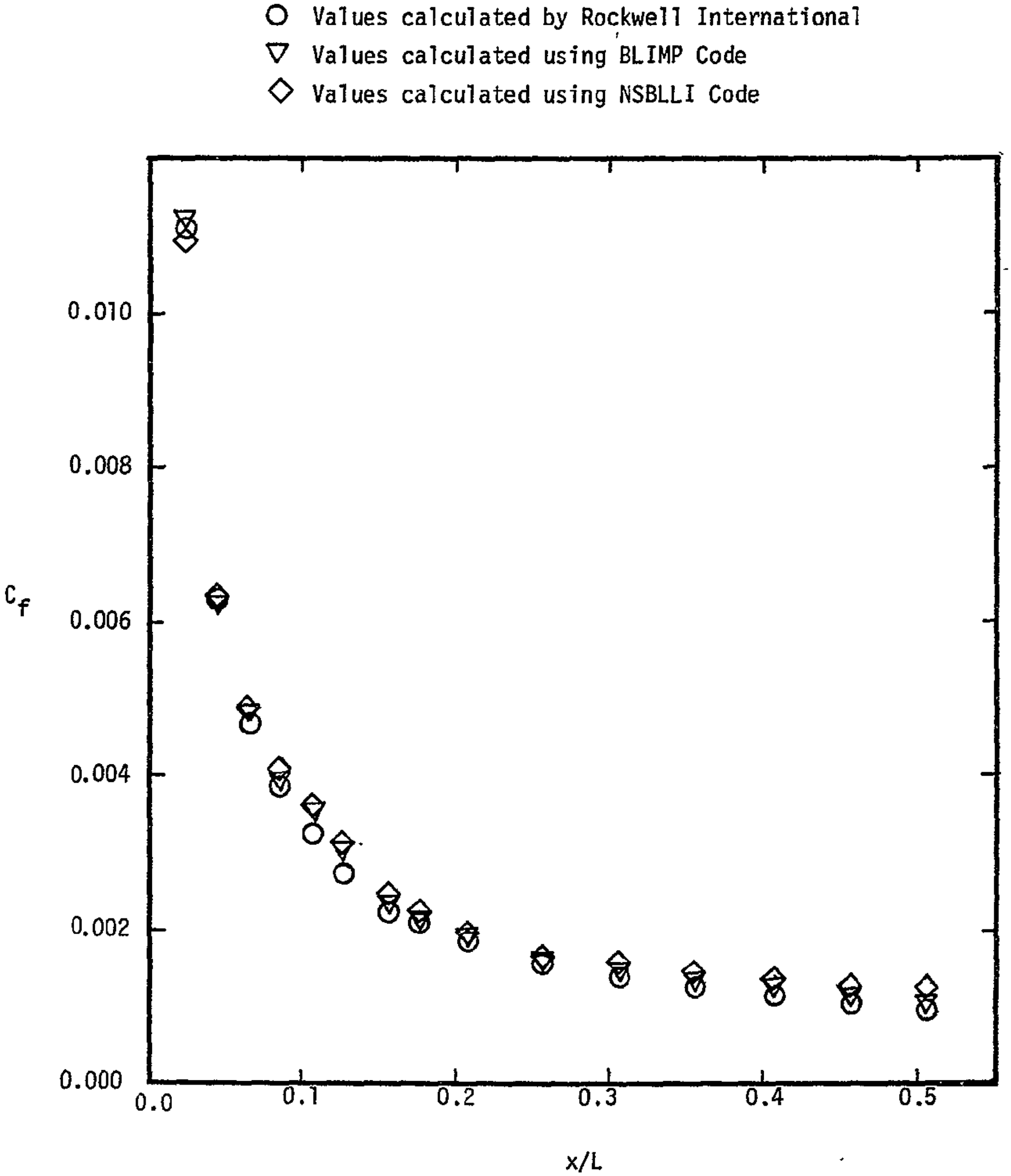

(c) The skin-friction coefficient

Figure 21. - Continued

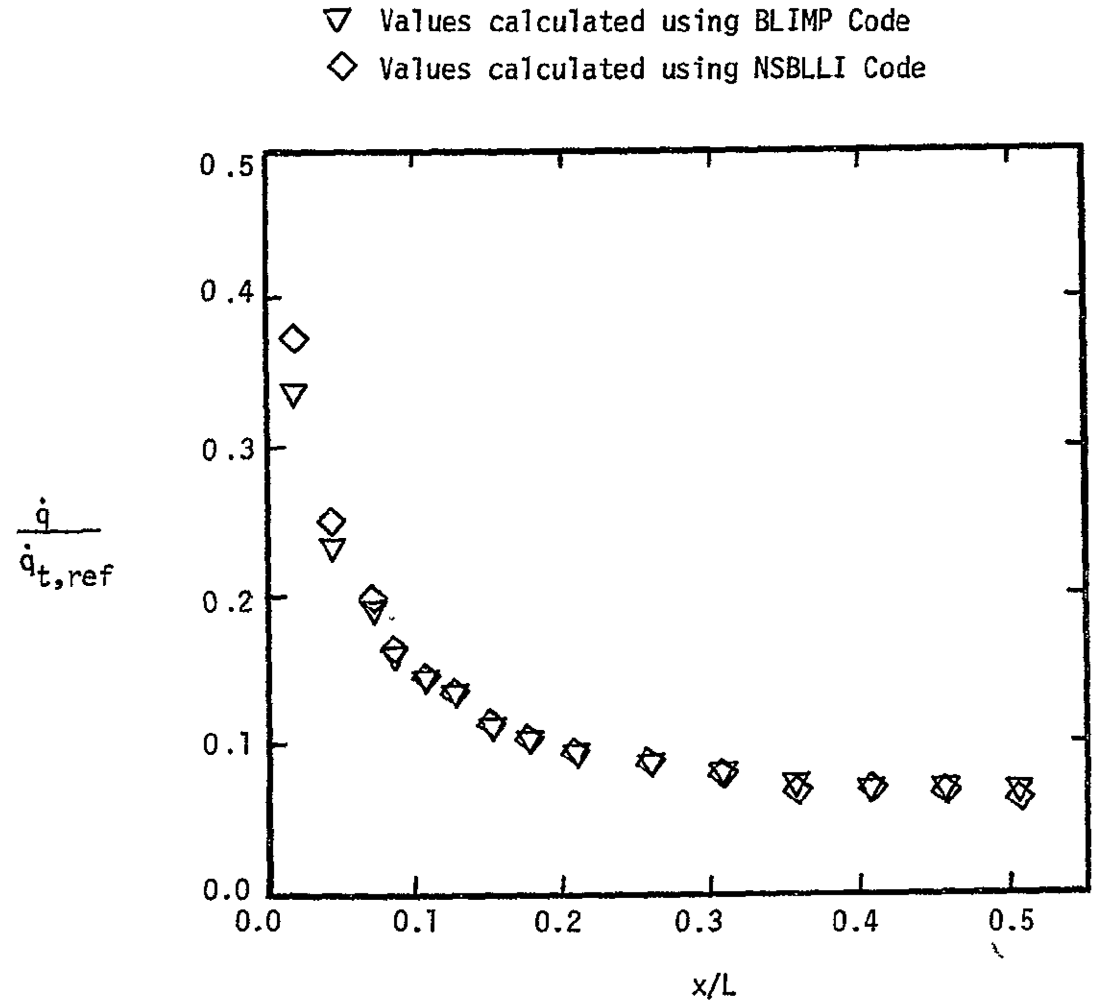

(d) The heat-transfer rates

Figure 21. - Continued

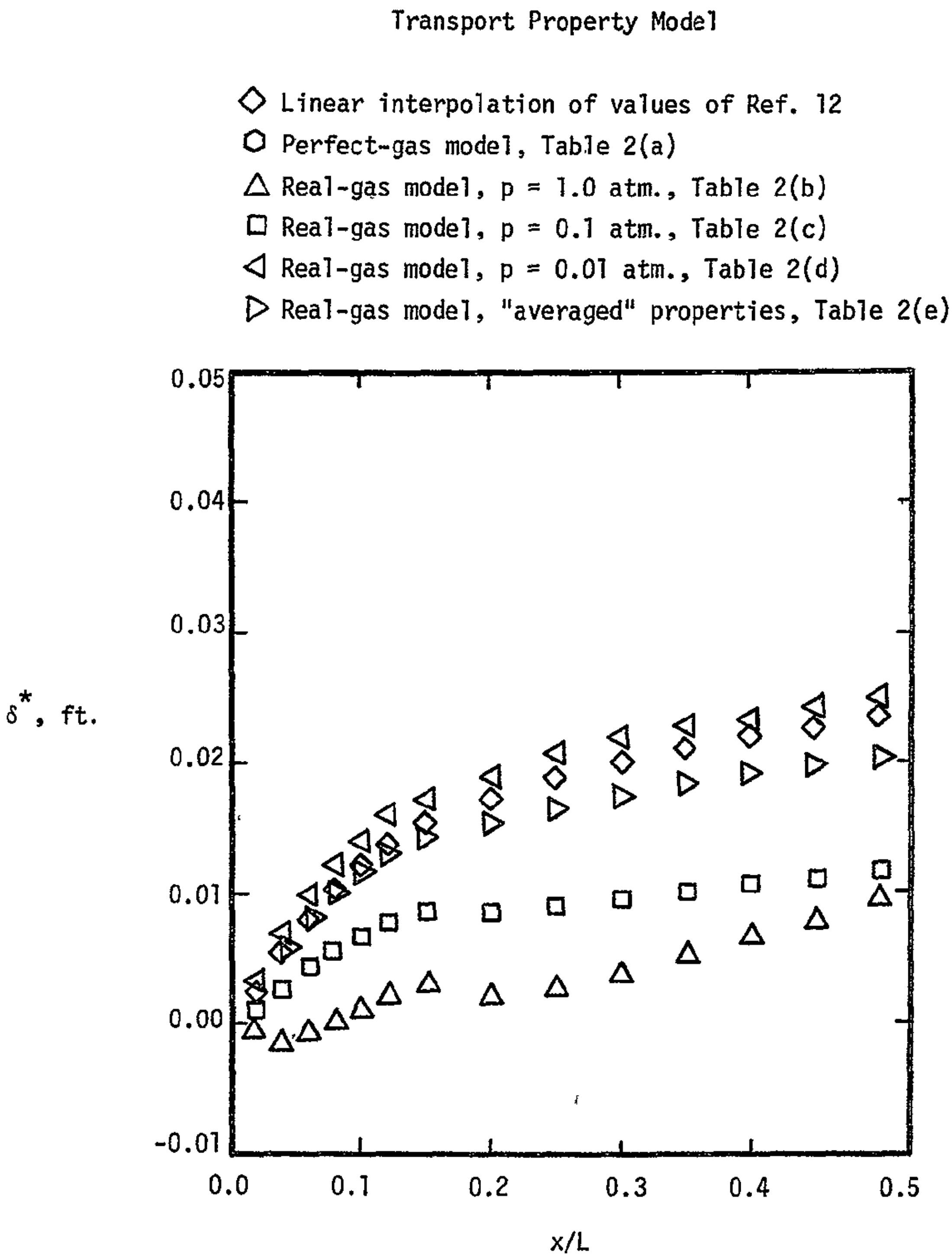

(a) The displacement thickness, δ^*

Figure 22. - The aerothermo distributions as calculated for the six transport property models for flow condition (c), M_∞ = 22.04.

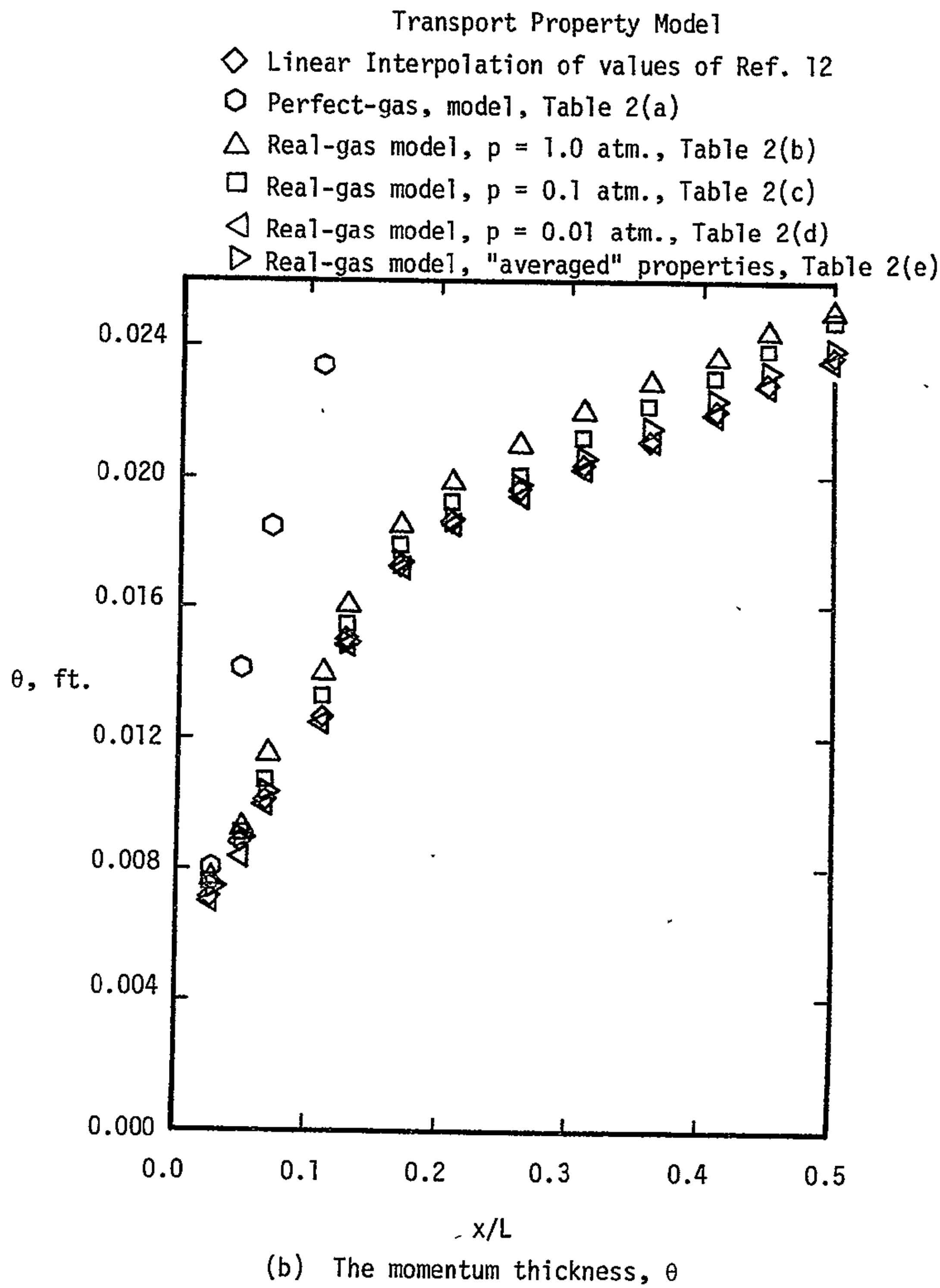

Figure 22. - Continued

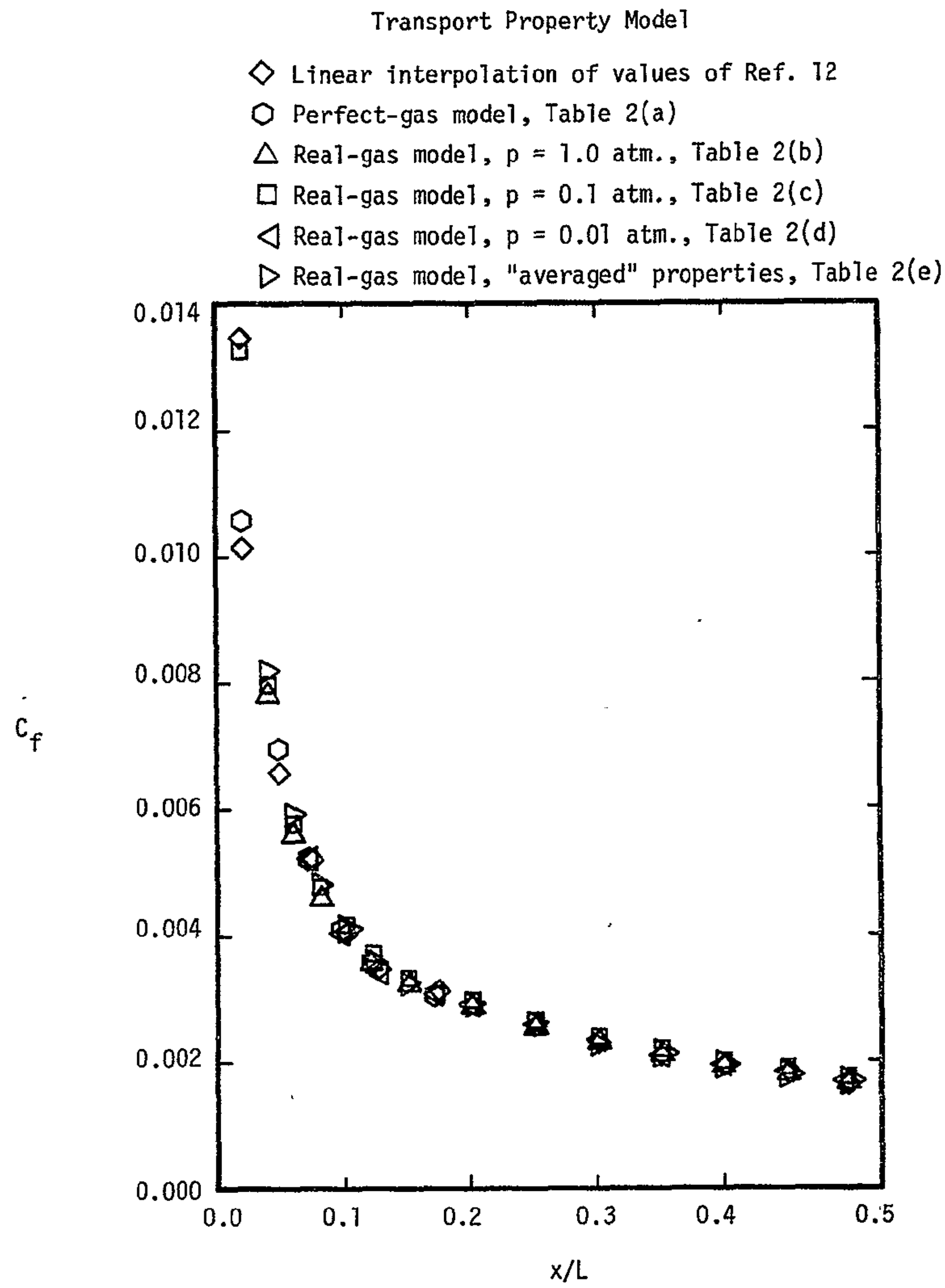

(c) The skin-friction coefficient, C_f

Figure 22. - Continued

C-2

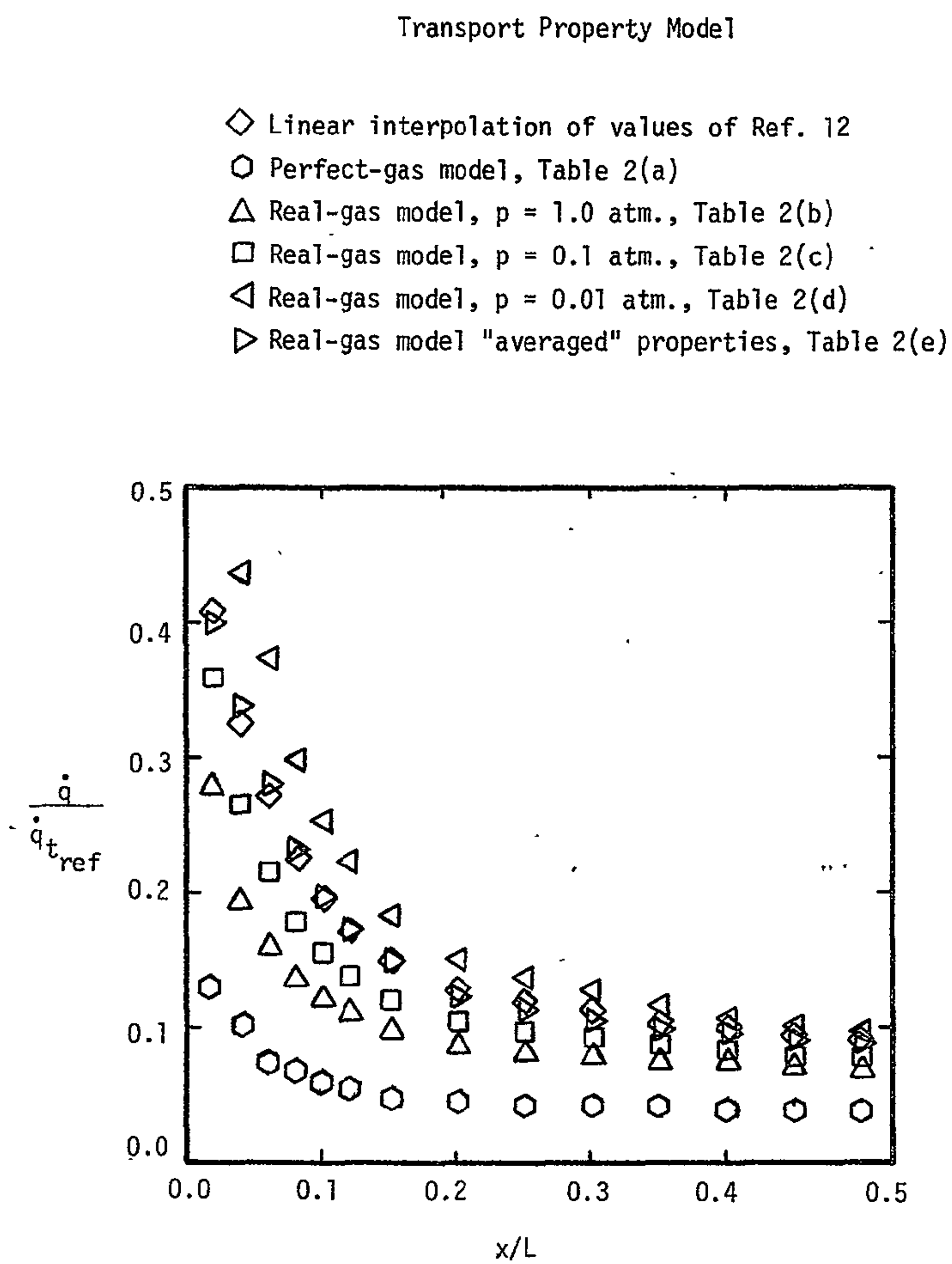

(d) The heat-transfer rates

Figure 22. - Concluded

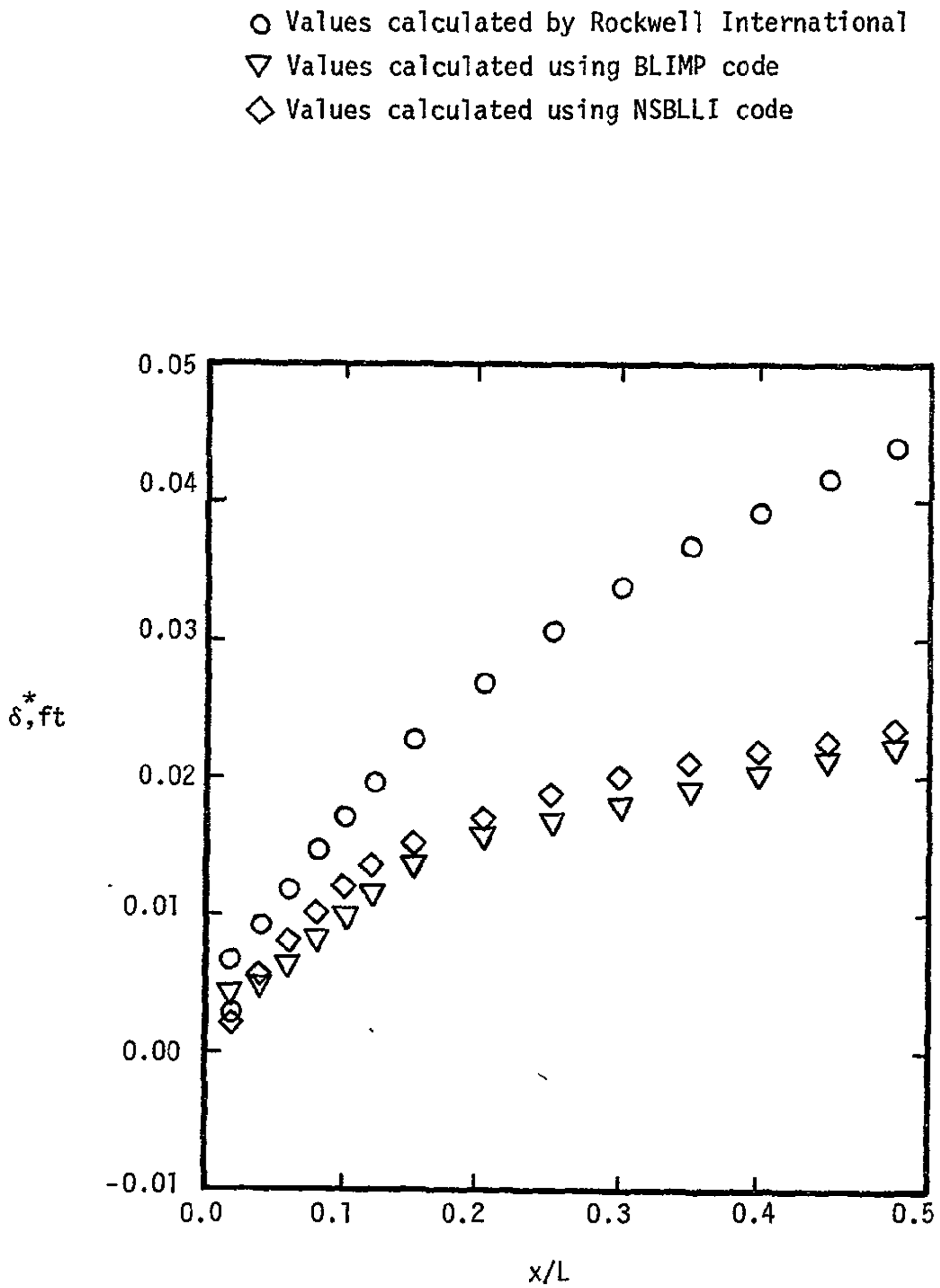

(a) The displacement thickness, δ^*

Figure 23. - The "real-gas" aerothermo distributions as calculated by three groups for flow condition (c), M_∞ = 22.04.

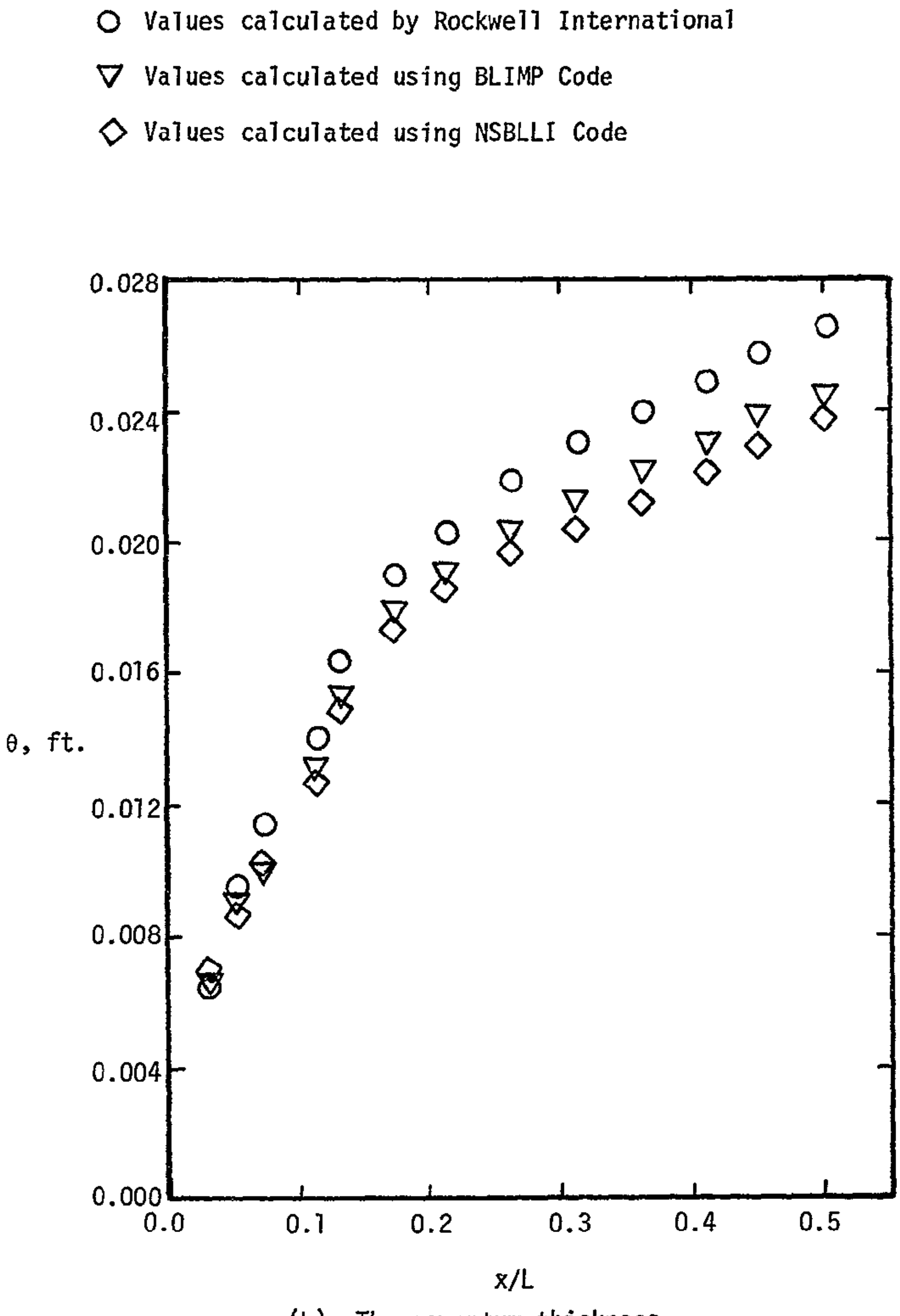

(b) The momentum thickness

Figure 23. - Continued

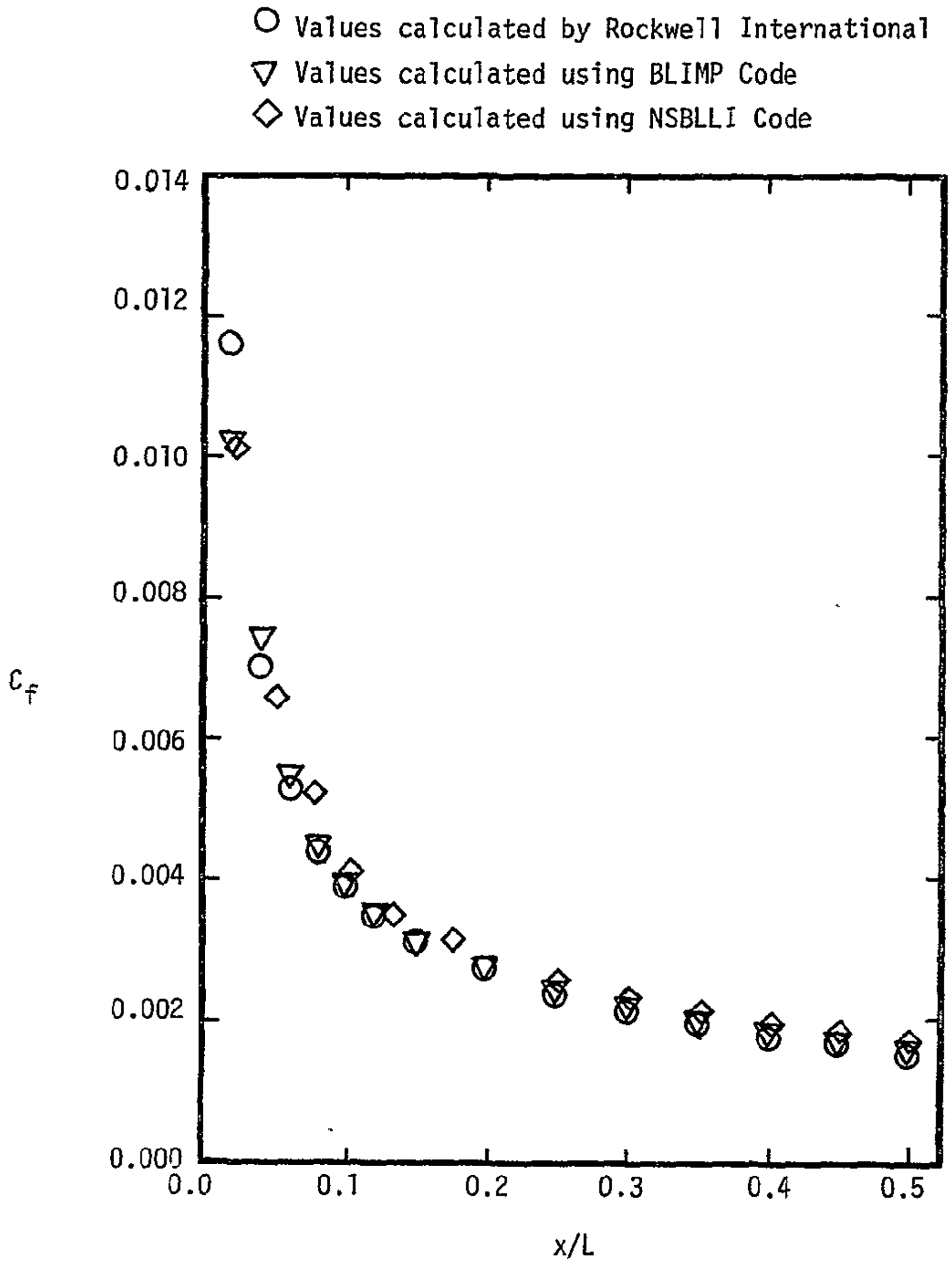

(c) The skin-friction coefficient, C_f

Figure 23. - Continued

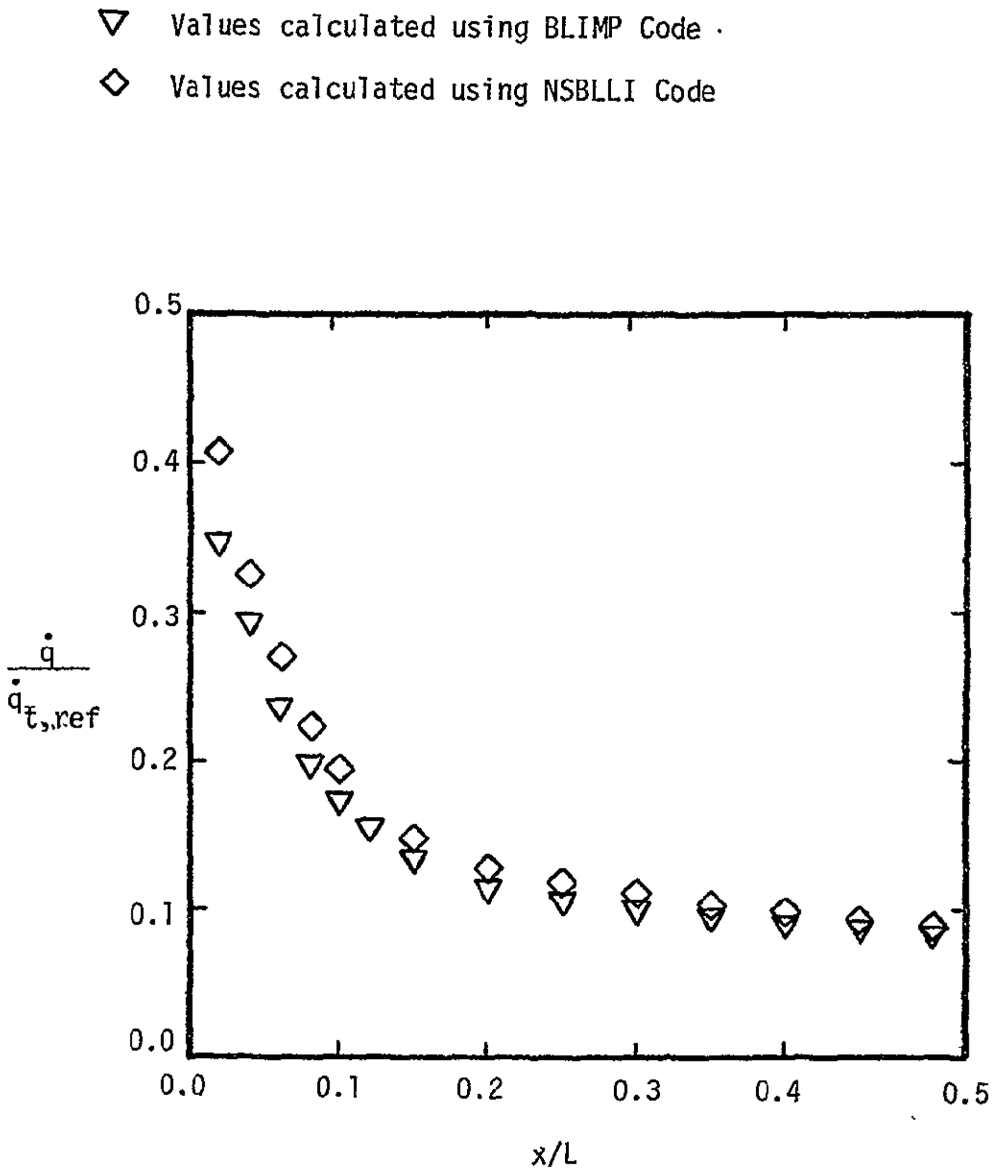

(d) The heat-transfer rates

Figure 23. - Continued

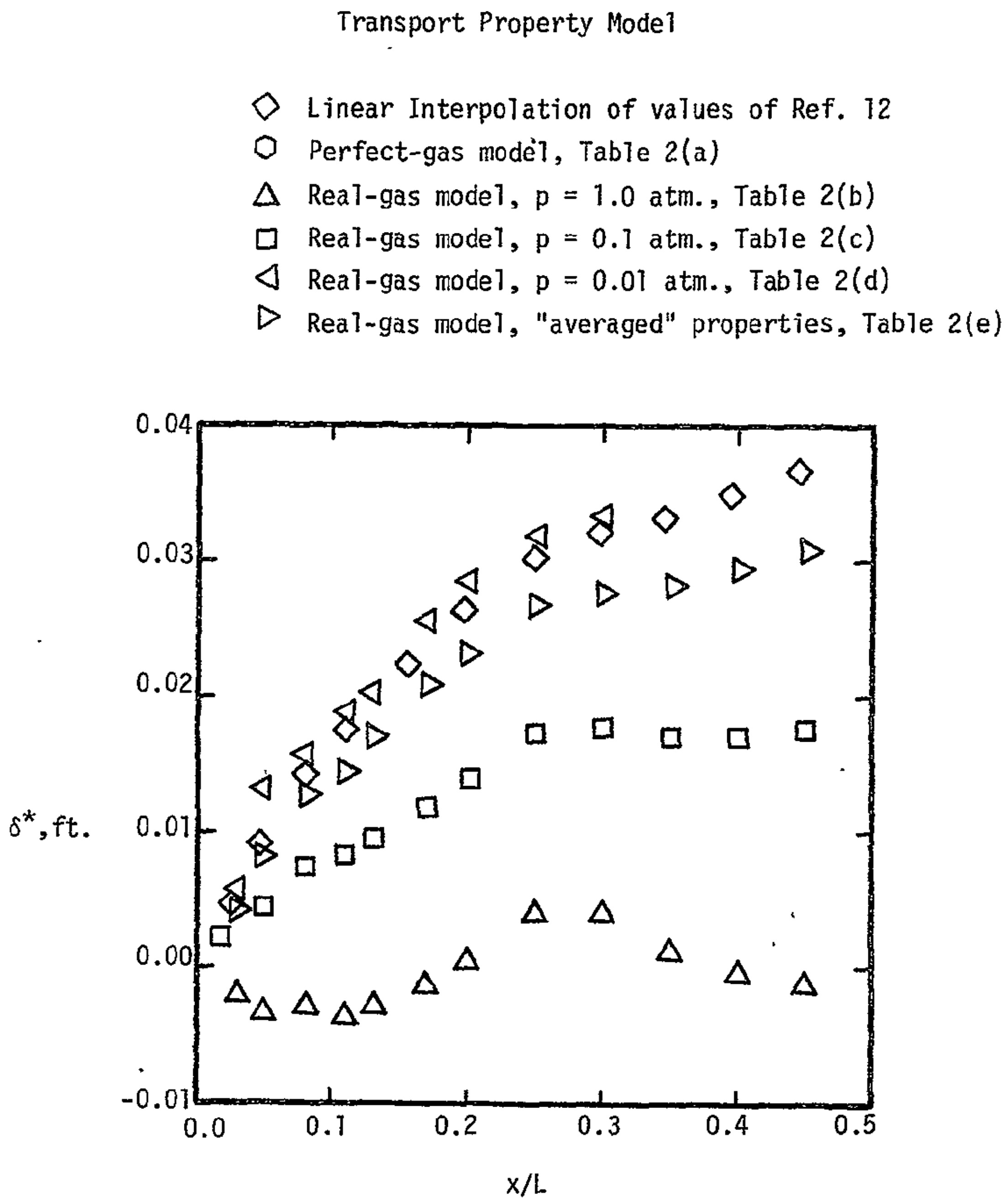

(a) The displacement thickness, δ^*

Figure 24. - The aerothermo distributions as calculated for the six transport property models for flow condition (d), $M_\infty = 29.86$

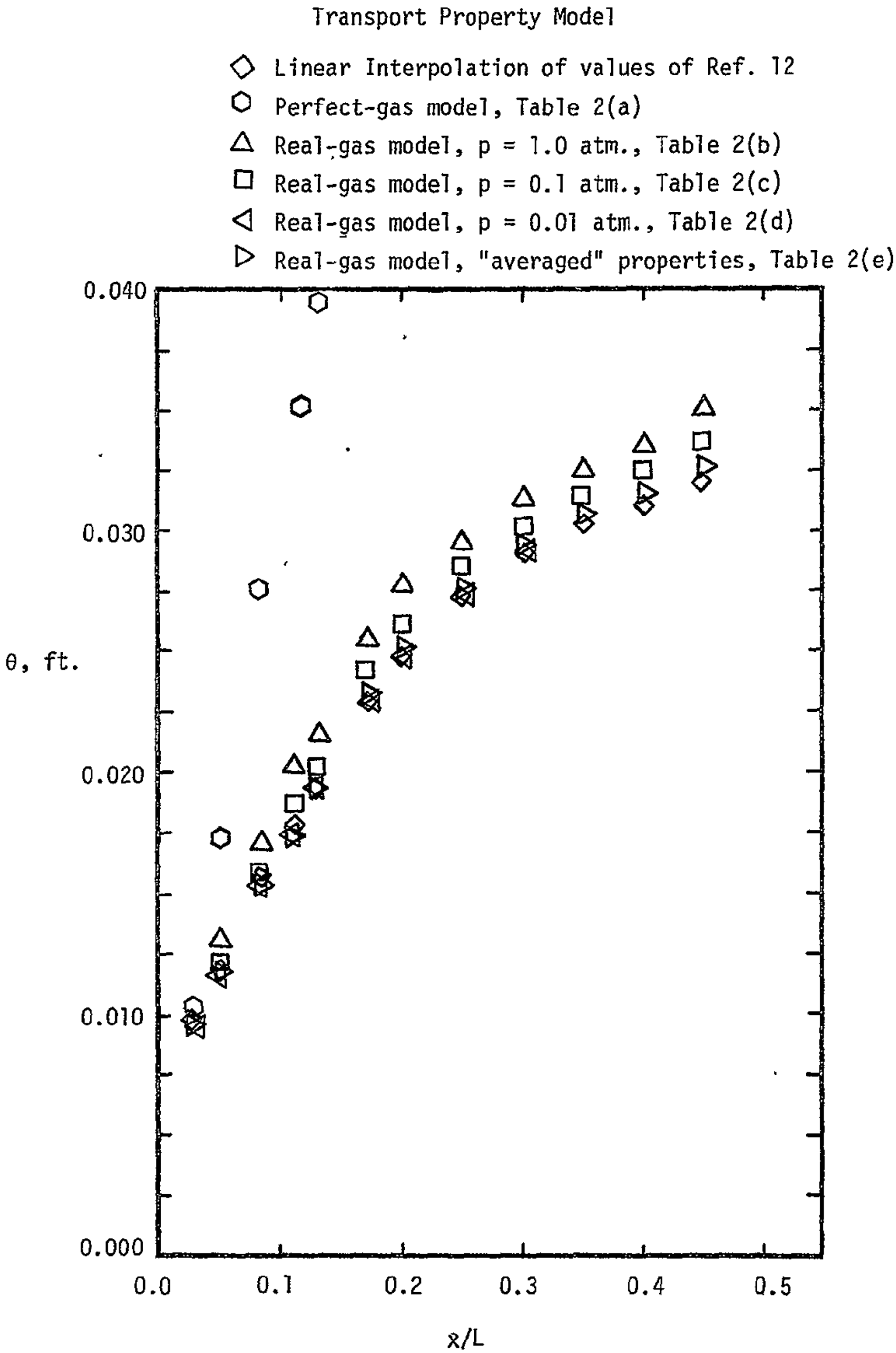

(b) The momentum thickness, θ

Figure 24. - Continued

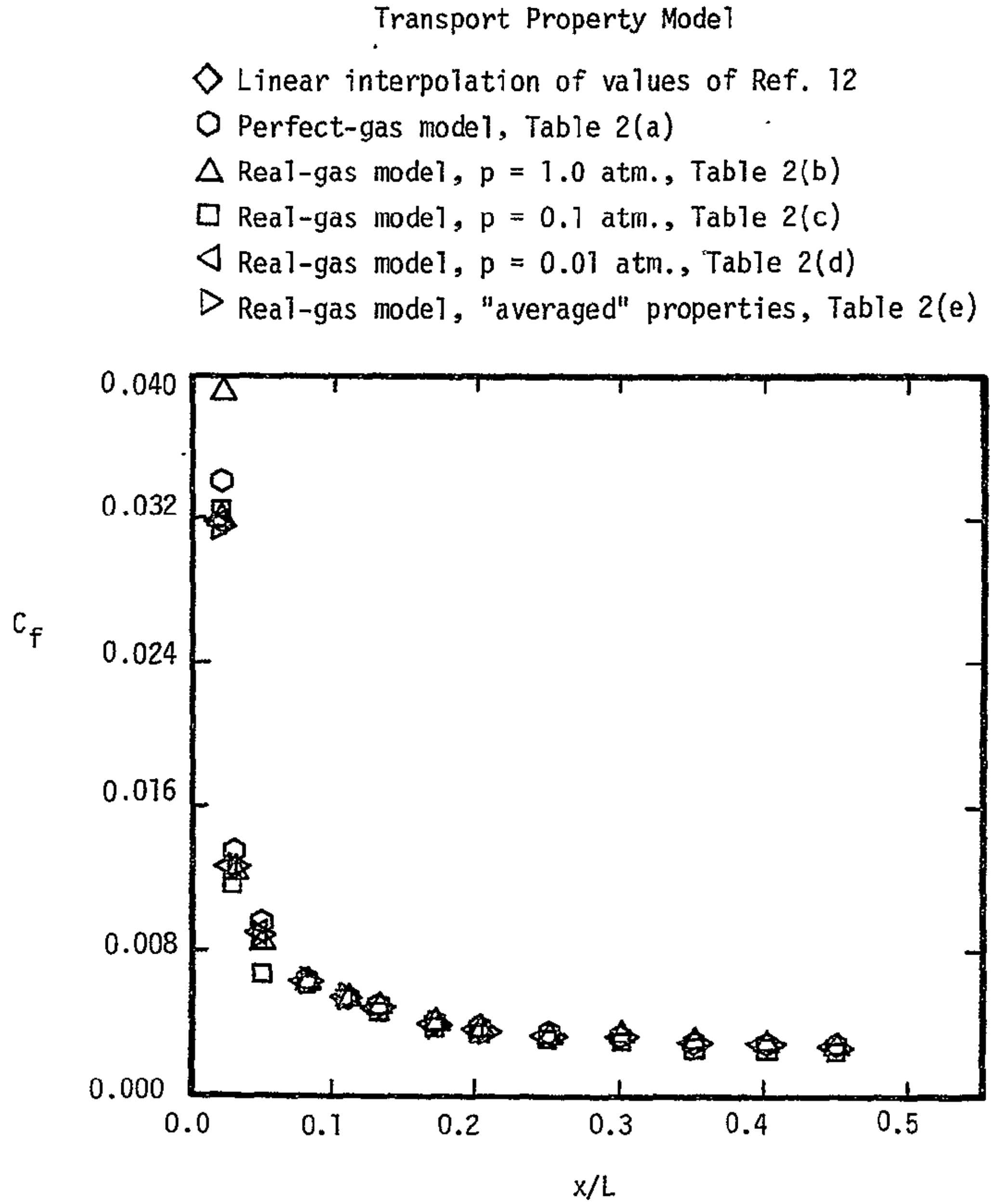

(c) The skin-friction coefficient

Figure 24. - Continued

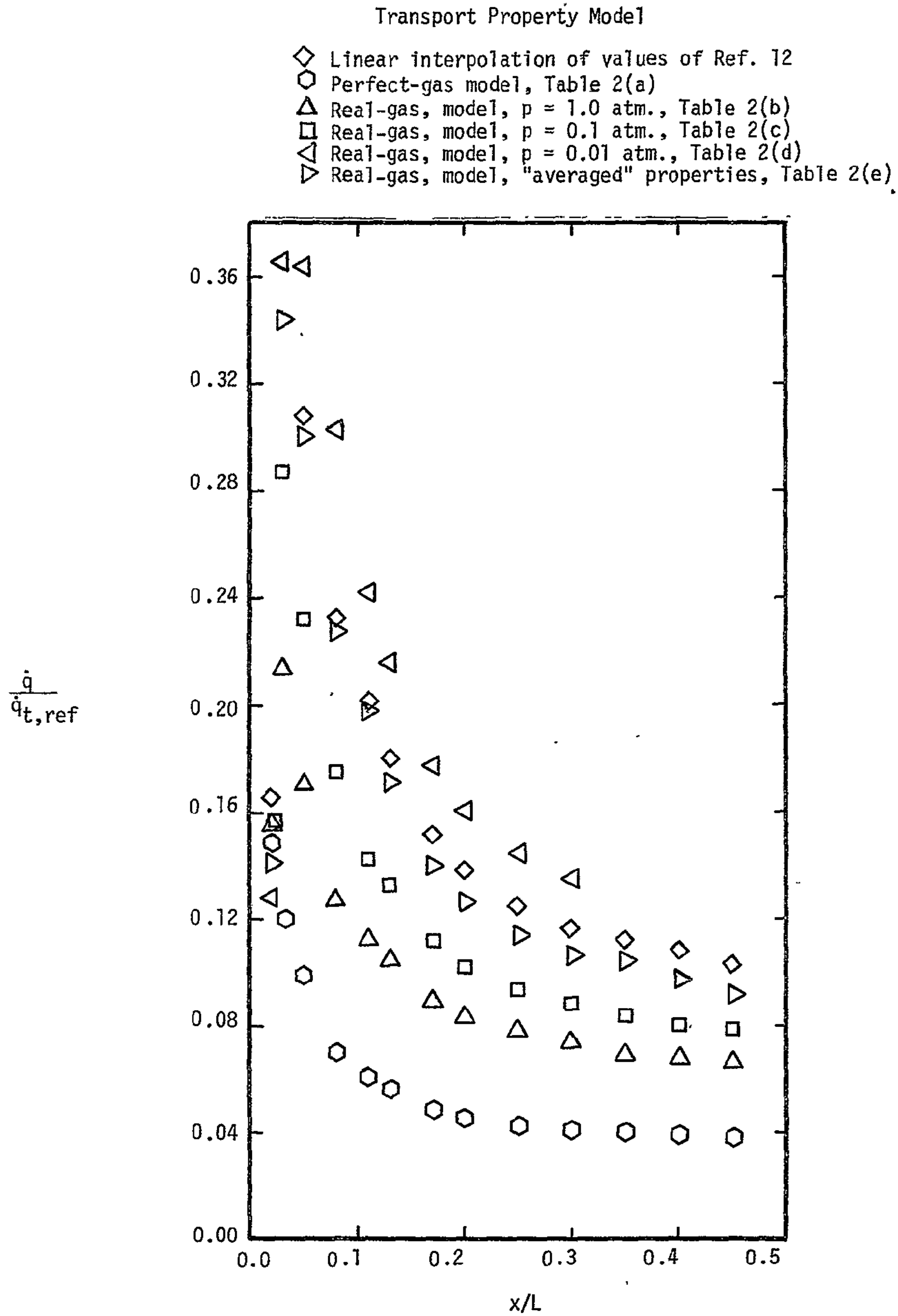

(d) The heat-transfer rates

Figure 24. - Concluded.

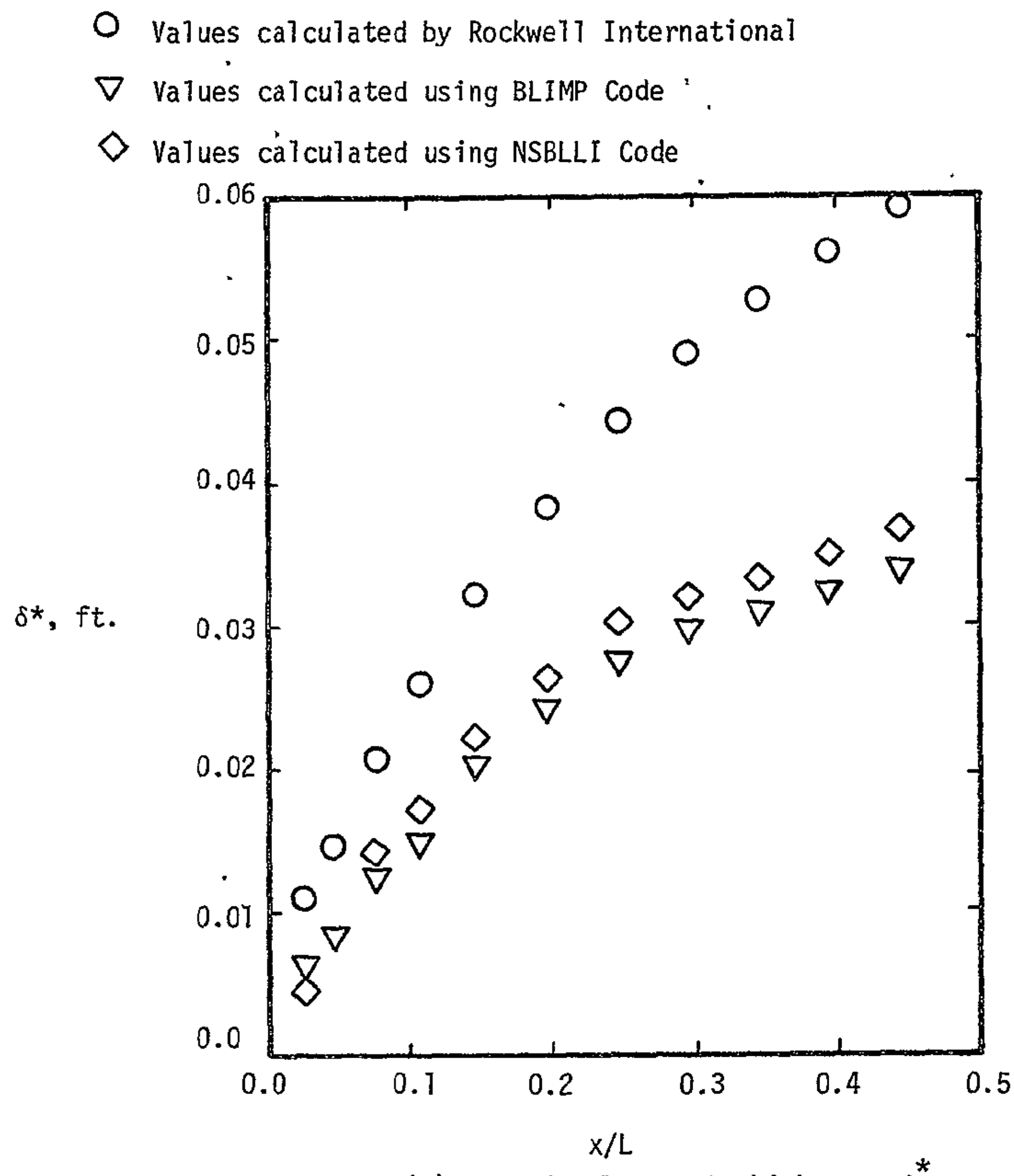

(a) The displacement thickness, δ^*

Figure 25. - The "real-gas" aerothermo distributions as calculated by three groups for flow condition (d), M_∞ = 29.86.

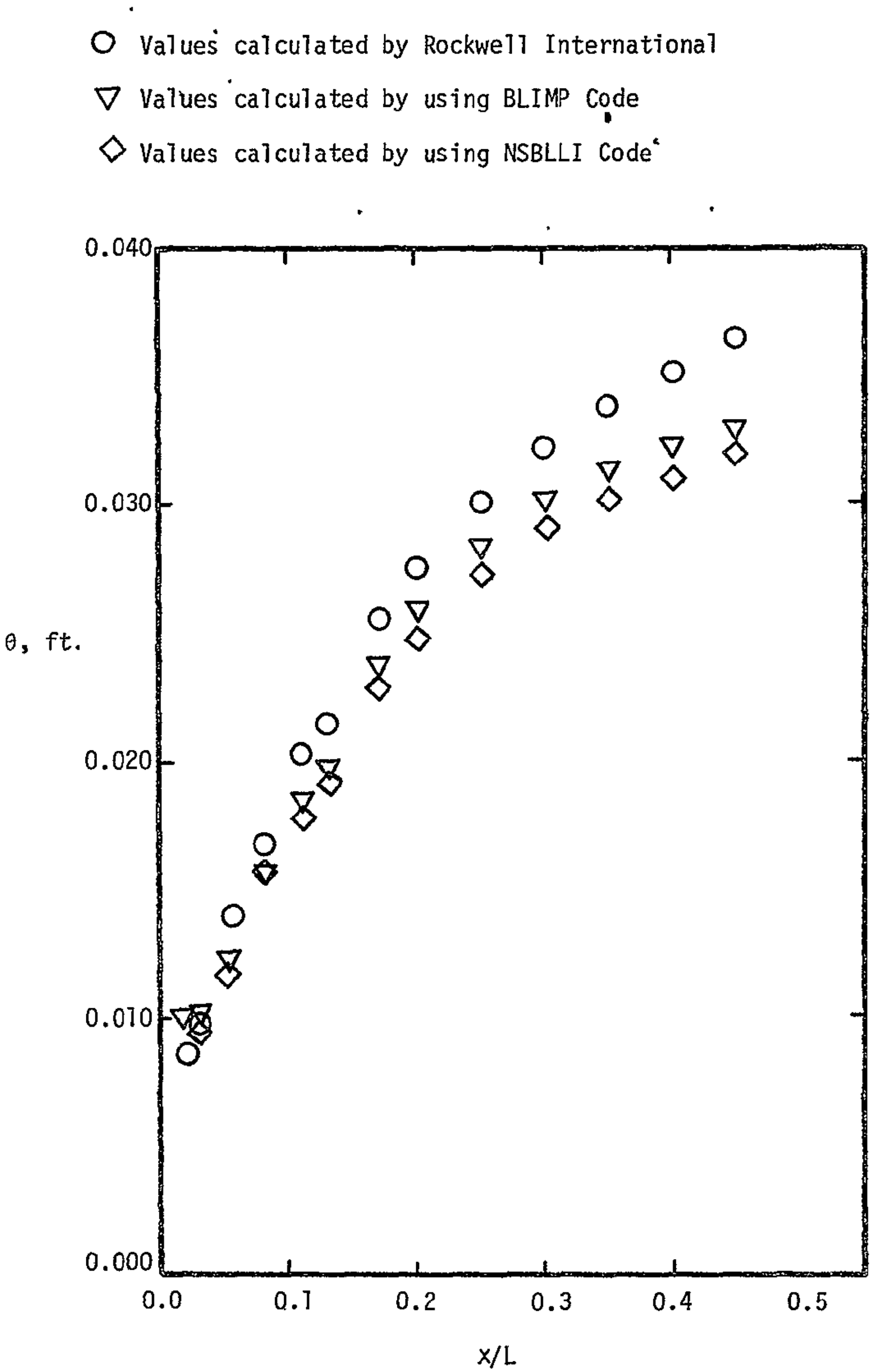

(b) The momentum thickness, θ

Figure 25. - Continued.

○ Values calculated by Rockwell International.

▽ Values calculated by using BLIMP Code

◇ Values calculated by using NSBLLI Code

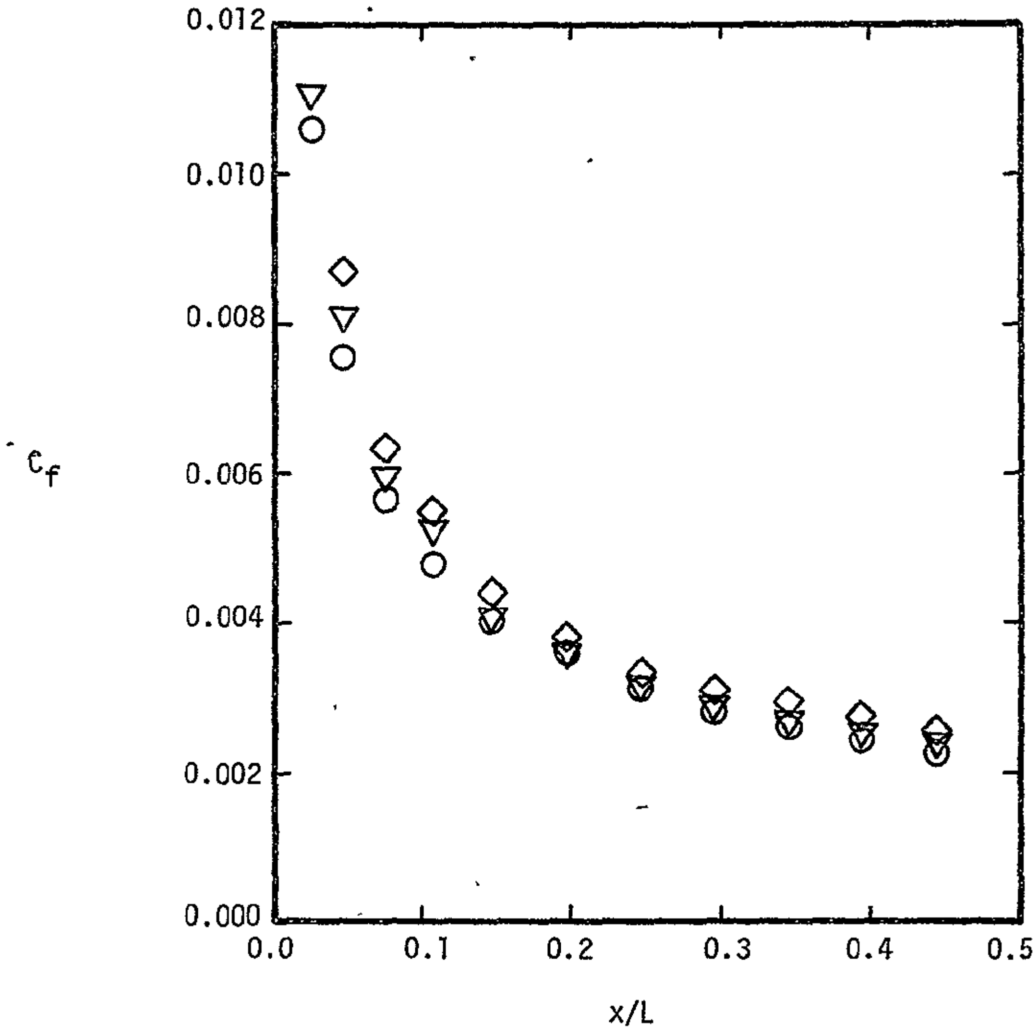

(c) The skin-friction coefficient

Figure 25. - Continued.

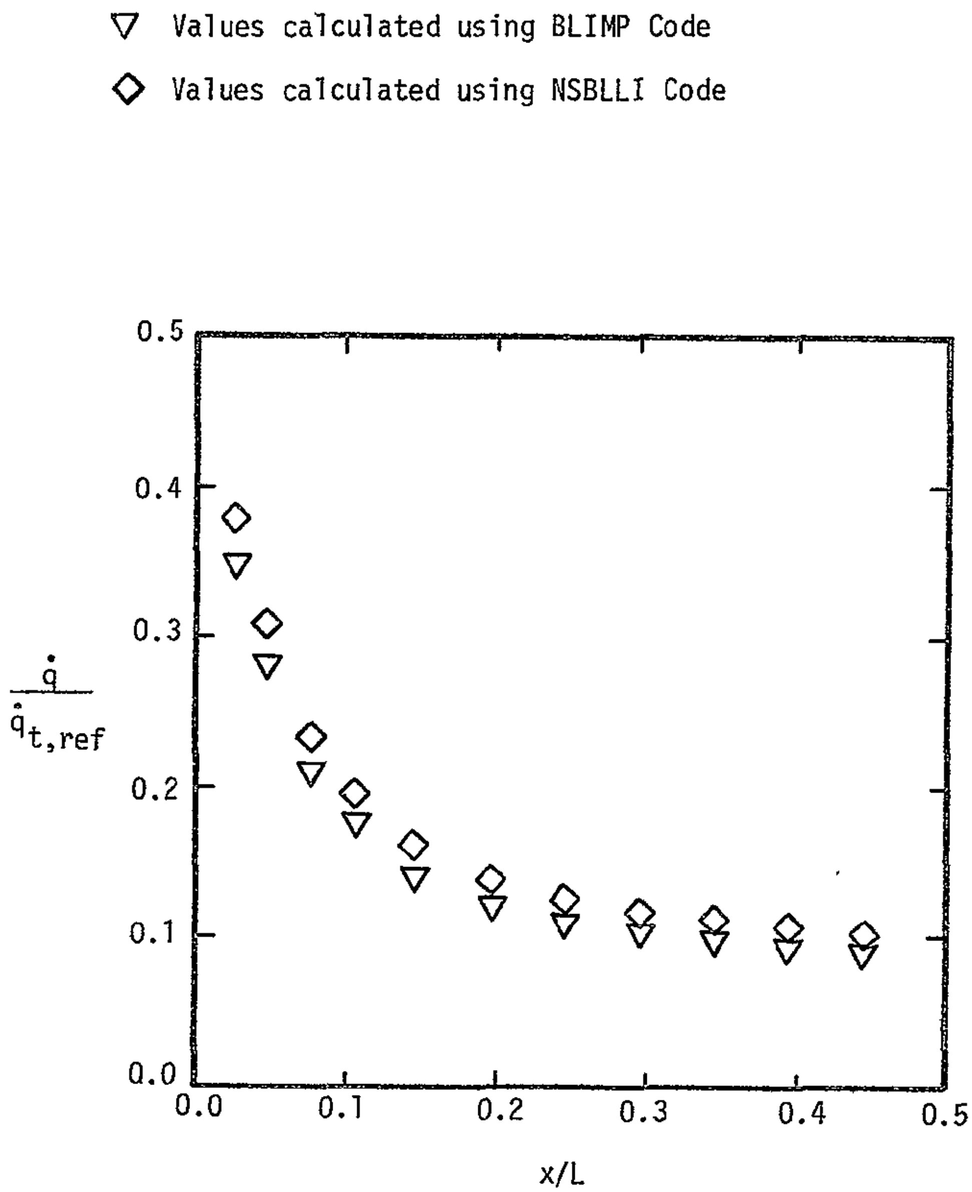

(d) The heat-transfer rates

Figure 25. - Concluded.